UNIVERSITY OF CALIFORNIA

Los Angeles

Miniature magnetic devices for compact accelerator applications

A dissertation submitted in partial satisfaction
of the requirements for the degree
Doctor of Philosophy in Electrical and Computer Engineering

by

Benjamin Arnell Pound

2022

ABSTRACT OF THE DISSERTATION

Miniature magnetic devices
for compact accelerator applications

by

Benjamin Arnell Pound
Doctor of Philosophy in Electrical and Computer Engineering
University of California, Los Angeles, 2022
Professor Robert N Candler, Chair

Electron accelerators play crucial roles in medical, scientific, and industrial uses. There are many technologies that are being developed to make the accelerator portion of these machines smaller, which would decrease the overall cost and size of the machine, but development of the magnetic elements to focus these electron beams, called "quadrupoles", have not been as fully explored. The main focus of the work is the miniature Panofsky quadrupole. This type of quadrupole is planar in nature and so lends itself to batch fabrication using microfabrication techniques. Additional benefits include an arbitrarily long magnetic length limited only by substrate size and the potential for high current densities due to the relatively high thermal conductivity of silicon. Device characterization was accomplished via direct magnetic field measurement, analysis of heating using a thermal camera, and an experimental demonstration of relativistic beam focusing at the PEGASUS laboratory at UCLA. I briefly describe several other quadrupole devices, including a current sheet device that could be used as a distributed focusing element inside an undulator, which would address concerns in future small gap, low energy accelerator-based light sources.

Accelerator-based light sources also benefit from the miniaturization of accelerators and their magnetic optics. These light sources could also benefit further from development of short period undulators. Two short period undulators that could be used in a low-energy (less than 1 GeV) electron accelerator to produce radiation are presented: a microfabricated 1.2 mm electromagnet undulator and a 2.7 mm hybrid permanent magnet undulator. Both undulators were characterized via magnetic field measurement. Importantly, in the case of the hybrid undulator, the ability to shim the strength of an individual pole tip was demonstrated. While the electromagnet undulator, as measured, is not as strong as the hybrid, pulsed power through thicker traces would increase the utility of this device substantially. Taken together, this work represents a step forward for use of short period undulators.

The dissertation of Benjamin Arnell Pound is approved.

Pietro Musumeci

Chandra J Joshi

Benjamin S Williams

Robert N Candler, Committee Chair

University of California, Los Angeles

2022

To my wife and kids.

TABLE OF CONTENTS

LIST OF FIGURES

LIST OF TABLES

ACKNOWLEDGMENTS

There's a saying that goes something like "it takes a village to get a PhD". Here are some people in my village that have helped me.

- Past group members - you know who you are.
- Emily Burnside, for keeping me sane. Thanks for lab-crashing.
- Cleanroom staff; for all your hard work keeping the tools running in spite of my best efforts to break them.
- the many admins that helped with my near-weekly purchase orders.
- Jere Harrison; we only talked once or twice, but your strong legacy in the lab lives on.
- Rob Candler, for pretty much everything.
- my family who put up with early mornings, late nights, and the cramped quarters of a west LA apartment, and still greet me with a smile and the hug at day's end.

VITA

2009–2010, 2012–2015	Accepted to Utah State University as an Undergraduate Research Fellow; performed research on various applications of carbon nanotube forests in the groups of Dr. Lisa M. Berreau (1 year), Dr. Charles Torre (0.5 years), and Dr. T.-C. Shen (2.5 years).
2014	Summer internship at the National Institute of Standards and Technology, Maryland, with Dr. Mark Stiles.
2015	B.S. in Physics from Utah State University; minors in Chemistry and Mathematics. Graduated *summa cum laude* as the College of Science Scholar of the Year.
2015	Summer internship at the National Institute of Standards and Technology, Boulder, with Dr. Gary Zabow.
2015–2017	Post-baccalaureate researcher at Los Alamos National Laboratory.
2017–2022	National Science Foundation Graduate Research Fellow
2019	M.S. (Electrical and Computer Engineering), UCLA, Los Angeles, California.

CHAPTER 1

Introduction

1.1 Motivation for using microelectromechanical systems in particle accelerators

Microelectromechanical systems (MEMS) are a class of micron-scale devices that comprise a wide variety of uses outside of integrated circuits. It is impossible to state every MEMS application, but microfabrication techniques (initially developed for the integrated circuit industry) are now used to manufacture gyroscopes [5], accelerometers [6], clock oscillators [7], gas sensors [8, 9], plasma sources [10], and many others [11, 12, 13, 14, 15, 16] with dimensions of nanometers up to a millimeter. The market share of MEMS devices is growing rapidly. As an example, over 4.4 billion MEMS microphones were sold in 2016 for around 1 billion USD. By 2022 the total market for MEMS microphones alone is projected to be around 20 billion USD [17].

There are many characteristics of microfabrication that are appealing from a device and cost perspective:

- The cost per device is low because many devices are fabricated in parallel ("batch processing") on a single wafer
- Many different materials can be used, and material properties can often be altered in substantial ways by changing process parameters.
- Device performance variation is low between wafers for a given process and well-

maintained tools.

- The high thermal conductivity and capacity of silicon allow high current density ($\sim 1 \times 10^{10}$ A/m^2) in thin copper traces [18]

- Feature size and alignment between individual devices (such as a quadrupole triplet) is automatically satisfied with single micron precision or better across the entire substrate [19]

Microfabrication has numerous difficulties as well. The processes are largely extrusions of two-dimensional designs, so fabricating truly three-dimensional devices is difficult. Process development can be slow due to the tight performance constraints for many devices. Owning and operating a cleanroom (where microfabrication is done), requires a very large initial investment and has high ongoing operating costs.

MEMS devices are used in almost every industry, but one industry where microfabrication has *not* made substantial inroads is accelerator physics. Most particle accelerator facilities are very large and use large beams with dimensions on the order of millimeters and centimeters, which largely precludes the use of microfabricated structures. New and upgraded facilities, however, are growing physically larger over time, which also leads to increased cost. It has become prudent to ask if facilities that span kilometers and cost billions of dollars can be built smaller and cheaper using less conventional technologies. One example of such a technology is the dielectric laser accelerator (DLAs), which are typically microfabricated [20]. DLAs and other MEMS-based devices require small beams (and thus small beam emittance) because they have small bores of $\sim$1 μm - 1 mm; it has only been somewhat recently that beam emittance has decreased enough, with sufficient charge, that using such devices can be seriously considered.

In this dissertation I will:

- motivate the desire to make accelerators (both industrial and research-grade) more

compact.

- briefly describe the current state of the art in actual accelerators and prospects for compact accelerators, and
- discuss my work in designing, fabricating, and testing microfabricated and micromachined quadrupole magnets (for beam focusing) and undulators (for radiation production) for use in compact accelerators.

1.2 Uses of electron accelerators

As it turns out, the most well-known class of particle accelerators such as the Large Hadron Collider is also the rarest type, comprising only approximately 1% of all accelerators worldwide [21]. The vast majority of accelerators are not used as particle colliders (or other research-focused machines) that operate with giga- or teraelectronvolt (GeV, TeV) beam energies but are rather dedicated to industrial uses with energies measured in megaelectronvolts (MeV). Some such applications are:

- Medical: electron beam therapy [22, 23], isotope production [24], radiography [25], sterilization [26]
- Polymer curing [27, 28, 29]
- Ion beam implantation [30]
- Microfabrication [31, 32, 33]
- Cargo inspection [34, 35]

While in no way a comprehensive list, it is apparent that electron beams play a role in a wide variety of industries. Furthermore, it is reasonable to expect that many industries would benefit from the development of smaller, cheaper compact accelerators. There are

many technologies that are being developed for this goal as will be briefly discussed in the next section.

1.3 Compact accelerators

There are effectively two strategies in the development of high-gradient accelerating devices. The first is to refine the design of the standard rf cavity and increase the frequency and operating power. The accelerating electric field gradient of a standard radio frequency cavity is limited to ~100 MV/m at room temperature [36] and ~65 MV/m for superconducting niobium cavities [37]. It is possible to achieve accelerating gradients higher than 200 MV/m using such technologies use higher frequencies [38], though many difficulties remain. One could also operate the normal-conducting accelerator at cryogenic temperatures to achieve gradients of 250 MV/m [39].

Alternately, one could turn to other technologies which are less well developed but have greater potential performance in the quest of a more compact accelerator. One example is the dielectric laser accelerator often come in the form of photonic or Bragg-like gratings [40, 41]. These devices generally produce beams that are wide and thin to increase overall electron beam current and suppress instabilities. In particular, groups investigating dielectric laser acceleration (DLA) in photonic structures have achieved impressive acceleration gradients, routinely achieving several hundred MV/m [42, 43]; the current record, to the author's knowledge, is 690 MV/m [44]. Despite many successes, DLA approaches have limitations. It is difficult, though not impossible to achieve 100 MeV/m or higher gradients with sub-relativistic particles [45], and the maximum gradient is limited to about 10 GeV/m because of dielectric breakdown [46]. Another limitation is that DLA is most efficient when accelerating femtocoulombs of charge [47], whereas RF cavities and plasma-based accelerators can accelerate pico- or even nanocoloumbs of charge. Another important limitation is fabrication; there are many dielectric structures which can be envisioned and simulated to

work very well, but few can actually be fabricated effectively. It is possible that miniature electron sources with ultra-small emittances could play a role in advancing this technology further [48, 49].

The other class of novel technologies is based on plasma wakefield acceleration, broadly classified as either laser-driven wakefield acceleration (LWFA) or particle-beam-driven plasma wakefield acceleration (PWFA). These approaches can produce extremely large accelerating gradients. Accelerations over 100 GV/m have been demonstrated several times [50, 51], and there seems to be no upper limit on achievable accelerating gradients [52]. These approaches, however, have myriad downsides that hinder usage in compact accelerators. The first is that the previously cited high gradients are only achieved by a small fraction of the injected electrons. The final energy of most of the injected electrons was below 10 MeV [50]. In studies reporting higher mean electron energy gain, the accelerating gradients were much lower, around 100 MV/m. As could be inferred already, the spread of electron energies after acceleration can be quite large; the smallest reported energy spreads are on the order of a few percent, which is unsatisfactory for some uses such as free electron lasers which require much less than 1% energy spread [53, 54]. Another limitation is the experimental setup. LWFA requires very high laser power (and therefore very large lasers) in the range of terawatts to petawatts [55]. PWFA itself requires a high-energy accelerator capable of precise bunch separation. As the technologies currently stand, LWFA may be able to accelerate electrons for compact light source applications with further developments that improve beam quality, and PWFA seems more applicable for particle collider applications.

1.3.1 Accelerator-based x-ray light sources

If one desires a monochromatic, coherent, short pulse of x-rays (photon energy above 1 keV), there are essentially only two options, synchrotrons and x-ray free electron lasers. These accelerator-based x-ray light sources require highly relativistic electron beams (usually greater than 1 GeV) to operate. Such high energies conventionally require large accelerators;

the accelerator portion of x-ray FELs (XFELs) is typically ~1 km to achieve the required energy.

Why are such machines needed to produce x-rays? There are two main reasons. The first is related to reflectivity and absorbance. All matter absorbs x-rays. There are many materials that reflect visible light with high efficiency, but no such material exists for x-ray wavelengths, so one cannot build mirrors and cavities for x-rays easily. There are some ways around this using Bragg reflectors, even for normal incidence x-rays [56], but these approaches have major issues yet to be resolved. Even if such a cavity could be built, population inversion (the mechanism by which conventional lasers operate), is not possible (at least in a practical sense) for x-ray frequencies as it requires a free-electron laser to drive the population inversion [57].

Additionally, the few options to generate coherent x-rays (special diode lasers [58] and high harmonic generation [59]) suffer from low photon flux compared to accelerator light sources. For hard x-rays the only alternative option is bremsstrahlung radiation, which has low flux and coherence.

Therefore, the remaining option is to build an accelerator-based light source such as an XFEL or synchrotrons. Both XFELs and synchrotrons are very large ($>$ 1 km), expensive ($>$ \$1B) facilities, both to build and run. Making these machines more compact would allow them to be built more cheaply, which would also increase access for a wider variety of researchers. These facilities are often oversubscribed, or in other words, the number of proposed experiments far exceeds the amount of time available. The result is that much good and useful research cannot be accomplished. The realization of more compact facilities would allow more research to be done, to the benefit of all.

The workhorses of these accelerator-based light sources are the "insertion devices" known as undulators or wigglers. The insertion devices can be inserted or removed arbitrarily because they do not perturb the overall beam trajectory. Inside the insertion device, however, the alternating dipole fields of undulators and wigglers cause the electrons to "wiggle" as

they traverse the alternating fields. Undulators and wigglers are characterized mainly by the period λ_u (the length over which the magnetic field changes), the number of periods N_u, and the peak magnetic field on-axis in the undulator. Undulators have relatively weak fields that only slightly perturb the electron trajectory, which results in narrowband radiation. A wiggler has strong magnetic fields that strongly perturb the electron motion, which produces broadband radiation.

1.4 Compact quadrupoles and undulators for compact accelerators and light sources

Although the electron accelerator obviously needs to be miniaturized for truly compact accelerators, the undulator also should be compact for electron beam based light sources. It has long been realized that shortening the undulator period could help accomplish both goals. A shortened undulator period would allow for a lower electron energy, which would also decrease the accelerator length and therefore the cost [60]. It is possible that the total undulator length could also decrease. Chapter 3 showcases our work simulation and experimental work on a microfabricated 1.2 mm electromagnetic undulator fabricated using both conventional and microfabrication techniques, and some preliminary work on a 2.7 mm hybrid undulator fabricated using waterjet cutting and 3D printing.

Chapter 4 shows two novel quadrupole devices, a quadrupole based on two current sheets that could be trivially included in future short period, small gap undulators, and a monolithic quadrupole fabricated from a single block of copper.

Chapter 5 presents a comprehensive study of the microfabricated Panofsky quadrupole (MPQ), including the derivation of an analytical model and experimental and simulation results for both magnetic fields and thermal behavior. The device was tested in a 3.2 MeV beamline, demonstrating focusing of a relativistic beam with a microfabricated device for the first time. This same type of device geometry was replicated using more conventional ma-

chining techniques adapted for small features, which work is presented in the same chapter. These devices would be used as focusing optics in a future compact accelerators.

Taken together, it is my hope that some of the ideas presented here will be useful in future considerations of compact accelerator design.

CHAPTER 2

General Background

This section contains background information that is common to later chapters related to both undulators (chapter 3) in Section 2.1 and quadrupoles (chapters 4 and 5) here in Section 2.2.

2.1 Undulators for radiation production

2.1.1 Theory

A basic diagram of an undulator is shown in Fig. 2.1. As the electrons traverse the alternating magnetic dipole fields, they are forced to accelerate. Accelerating charged particles radiate photons. The undulator periodicity causes constructive interference at specific resonant frequencies and destructive interference at all other frequencies. It can be shown that the electrons in a planar undulator emit photons of wavelength $\lambda_{r,n}$:

$$\lambda_{r,n} = \frac{\lambda_u}{2n\gamma^2}\left(1 + \frac{K^2}{2} + \gamma^2\theta^2\right) \tag{2.1}$$

where λ_u is the undulator period, n is the harmonic under consideration, γ is the relativistic Lorentz factor of the electron beam ($\gamma = (1 - \frac{v^2}{c^2})^{1/2}$, where v is the electron beam velocity and c is the speed of light), and θ is the angle of observation away from the beam axis. The undulator parameter K is defined as

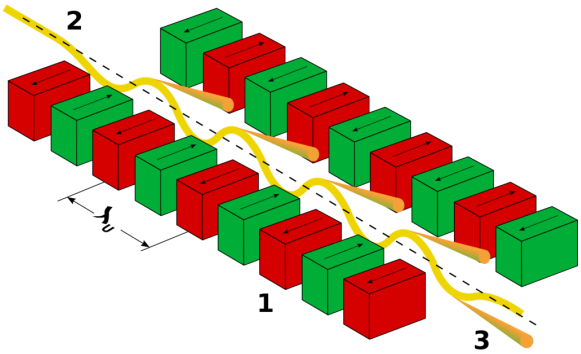

Figure 2.1: A basic diagram of an undulator. 1) the magnets that alternate field direction every period. 2) the electron beam entering the undulator. 3) the photons (of wavelength $\lambda_{r,n}$) produced in the undulator. From Ref. [1].

$$K = \frac{e}{2\pi m_e c} B_0 \lambda_u \approx 0.934 \lambda_u[\text{cm}] B_0[\text{T}] \tag{2.2}$$

where B_0 is the maximum mid-plane magnetic flux density, m_e is the electron rest mass, and c is the speed of light. If $K > 1$, the device is termed a "wiggler"; if $K < 1$, the insertion device is called an undulator. The main difference is that undulator radiation is largely limited to the fundamental harmonic, $n = 1$, and all even harmonics are suppressed [61]. Wiggler radiation possesses significant optical power in higher order ($n > 1$, including the even n) harmonics. For very strong wigglers the spectrum approaches that of a bending magnet [61] except with higher brilliance.

It can also be shown that the undulator radiation for an undulator with N_u periods possesses the linewidth

$$\frac{\Delta\lambda}{\lambda} = \frac{1}{N_u} \tag{2.3}$$

and that the radiation is mostly emitted into the central lobe which has a half angle of

$$\theta_{cen} = \frac{1 + K^2/2}{\gamma\sqrt{N_u}} \tag{2.4}$$

2.1.2 Motivations to develop short period undulators

There are a variety of applications for which short period undulators could be useful. We highlight some here.

2.1.2.1 Free electron lasers

The photon pulses from XFELs are very short (femtoseconds) with unmatched temporal and spatial coherence, that also have order-of-magnitude higher brilliance than other light sources such as synchrotrons. This is due to the high beam quality used in XFELs that allow for exponential optical power gain. However, to achieve this large amplification current XFELs require long undulators (around 100 m), which is expensive in both materials and equipment. Changing the undulator period from 3 cm (LCLS undulator period) to 3 mm, for example, would suggest a total undulator length of 10 m to keep the number of periods constant. Additionally, Eq. 2.1 shows that the undulator radiation wavelength λ_r is proportional to λ_u and $1/\gamma^2$. For a fixed radiation wavelength, therefore, shortening the undulator period would also lower the required electron beam energy, which would decrease the length of the electron accelerator portion and reduce cost further.

2.1.2.2 Spontaneous undulator radiation from low energy accelerators

Another application is simply use spontaneous undulator radiation without the exponential gain of FEL amplification. The radiation typically does not have the high coherence, peak photon flux, or ultrashort pulses that FELs provide, but is still very useful; the hundreds of beamlines housed at synchrotrons around the world use spontaneous undulator radiation for many different types of experiments.

2.1.2.3 Undulator diagnostics

Short period undulators could be useful as undulator diagnostics. Beam diagnostics are extremely important in the design and operation of any accelerator or light source [62]. Undulator-based diagnostics have been used to measure the absolute energy [63], energy spread [63, 64, 65], and transverse emittance [64, 66] of the electron beam by monitoring changes in the radiation spectra from the undulator. The potential advantages of using short period undulators over undulators with longer periods is that the physical area of the diagnostic could be made physically smaller and the energy of the radiation would be higher, relative to a longer-period diagnostic undulator. This could be helpful in low energy accelerators to shift the diagnostic radiation to a regime that is more easily measured. One example is a 10 MeV accelerator. Using a 3.3 cm period undulator yields photons at 1.6 THz, which relative frequency range is traditionally difficult to measure. Using a 1 mm period undulator at that same electron beam energy, however, yields photons in the near-IR regime at 1180 nm, which boasts a plethora of highly sensitive detectors.

2.1.2.4 Inverse FEL accelerator

Finally, a short period undulator could be useful in an inverse free electron laser (IFEL) accelerator. An FEL uses energy from electrons to create photons inside an undulator. One could reverse this process; impinge photons of the resonance wavelength on an electron bunch in an undulator to increase the kinetic energy of the electron bunch. Usually, however, the undulators have cm-scale periods and require that the electron beam energy already be ~100 MeV to achieve resonance with the undulator and IFEL laser driver [67]. With a millimeter scale undulator period, the initial electron bunch energy could be lowered by roughly an order of magnitude. IFELs are also sometimes used not for acceleration but the ability to microbunch the beam [68], which is required in some contexts [69, 70]. Again, with a shorter period undulator, lower energy electron beams could be microbunched.

2.1.3 Prior work

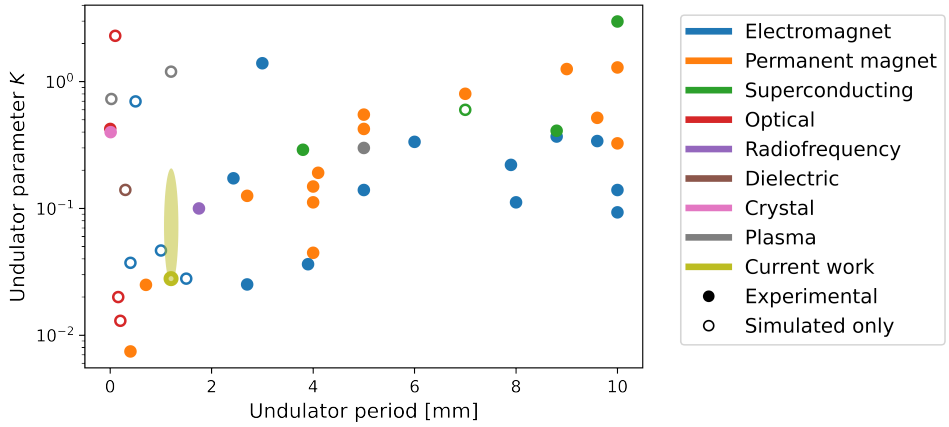

Figure 2.2: Prior work in sub-cm period undulators, categorized by type. The references for the devices in this plot are included as Supplementary Material.

A fairly comprehensive overview of prior work in sub-cm undulators is found in Fig. 2.2. There are some things the reader should know to put this comparison in proper context.

- The data point corresponding to the mesoundulator from this work represents the most conservative implementation of our design, which is a single coil or trace with dc current. A two-coil design, consisting of a coil on both sides of the wafer, can double the mid-gap magnetic flux density while not saturating the pole tips. Using pulsed current can further increase the maximum magnetic field. This range of operation parameters is roughly represented by the oval, where the upper limit is achieved through pulsed current.

- The majority of undulators are electromagnets (normal and superconducting) or based on permanent magnets. One can observe in this chart that the performance of permanent magnets dominates over similar-period electromagnets for the "large" periods considered here; this is the reason that most undulators with cm-scale periods are based on permanent magnets [71]. The popularity of superconducting undulators has increased as in-vacuum undulator technology has progressed and has the potential to

meet or surpass the performance of permanent magnet undulators. However, the technical demands of superconducting devices are higher than permanent magnet devices due to cooling, special power supplies, quench protection, and other considerations.

- At periods less than about 4 mm electromagnet and permanent magnet undulator performance is roughly equal. Electromagnets seem to have the advantage at very short periods because of pulsed power, despite the relatively lower fraction of magnetic material used in those designs.

- It is interesting to note that many of these undulators were fabricated in the 1980s and 1990s for the purpose of long wavelength free electron lasers, particularly around 300 GHz. Interest in FELs of such long wavelengths has diminished, but there is still much interest in using short period undulators for XFELs.

2.2 Quadrupoles for beam focusing

2.2.1 General theory

Two important devices for electron beam manipulation are dipole and quadrupole magnets. The fields, and their effect on an electron beam traveling into the page, are shown in Fig. 2.3. In short, dipoles steer electron beams and quadrupoles focus electron beams. The work for this dissertation has focused more on designing quadrupole magnets than dipole magnets.

Quadrupoles are characterized by both their transverse gradient B' and effective magnetic length L_m, which is the transverse magnetic gradient integrated along the beam axis through the quadrupole magnet, divided by the peak gradient. A quadrupole can be considered a "lens" for charged particles with a focal length (in the thin lens approximation), to be

$$f = \frac{p}{q}\frac{1}{B'L_m} \tag{2.5}$$

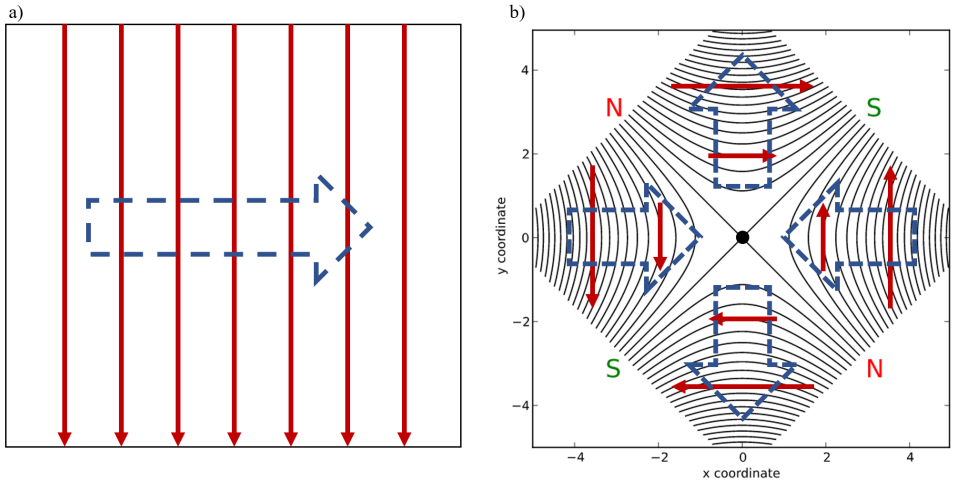

Figure 2.3: The forces on an electron beam traveling into the page due to the a) dipole and b) quadrupole fields. The red lines show the magnetic field direction, and the blue dashed arrows show the deflection direction of the electron beam.

where q is the electron charge and p is the particle momentum. However, we see from Fig. 2.3b that a quadrupole focuses a beam in one dimension and defocuses the beam in the other dimension. The beam can be focused in both dimensions by using multiple quadrupole magnets separated in space with fields rotated by 90 degrees.

As in standard ray optics, the trajectory of an electron beam can be calculated using a series of matrix multiplications [72]. For example, a single dimension of a quadrupole can be represented in the thin lens approximation by the matrix

$$M_{(f,d)} = \begin{bmatrix} 1 & 0 \\ -1/f & 1 \end{bmatrix} = \begin{bmatrix} M_{11} & M_{12} \\ M_{21} & M_{22} \end{bmatrix} \tag{2.6}$$

where f is the focal length from Eq. 2.5, taking f to be positive for a focusing quadrupole and negative for a defocusing quadrupole. The construction of these matrices can vary based on convention and types of analysis; for example, the matrix formulism can be extended to incorporate various other effects (see for example Ref. [73]). Nonetheless, in this simplest case, M_{11}, M_{22} are the spatial and angular magnifications respectively. M_{21} is related to

the beam focusing. Finally, if $M_{12} = 0$, then the system images from point-to-point (not parallel-to-point or point-to-parallel) with the magnification given by M_{11}.

A drift space (i.e., the space between quadrupoles) of length L_d can be represented by the matrix

$$M_O = \begin{bmatrix} 1 & L_d \\ 0 & 1 \end{bmatrix} \tag{2.7}$$

To find the focal length of a system of quadrupoles, assume there are two quadrupoles of the same strength where the first focuses the electron beam in one dimension and the second quadrupole defocuses the electron beam in the same dimension (and vice versa for the other dimension). Let the quadrupoles be separated by a length L_d. The total system, called a doublet, can be represented in matrix form:

$$\vec{x}_f = M_T \vec{x}_i = M_O M_d M_O M_f \vec{x}_i = \begin{bmatrix} 1 - \frac{L_d}{f} - (L_d/f)^2 & 2L_d + \frac{L_d^2}{f} \\ -\frac{L_d}{f^2} & \frac{L_d}{f} + 1 \end{bmatrix} \vec{x} \tag{2.8}$$

where $\vec{x}_i = [x_i, x_i']^T$, which describes the initial position x_i and angle x_i' with respect to the beam axis of a single particle. We see that, comparing the bottom left element of this matrix with the original focusing matrix of Eq. 2.6 that this doublet has an effective focal length of $f_{eff} = f^2/L_d$, which always positive. Therefore, the beam is focused in both dimensions. This does not mean, however, that the focal point is the same in both dimensions - the quadrupole gradient, length and/or spacing between magnets needs to be chosen to exhibit the desired behavior.

In general, a total-focusing system of quadrupole magnets can be composed of any number of magnets greater than one. There are distinct advantages to using triplets (composed of three magnets) or quadruplets (four quadrupole magnets) as compared to doublets, though these systems obviously occupy more valuable beamline space and represent additional cost

and complexity. We show total focusing in Fig. 2.4 using the matrix formalism for a a) doublet and b) triplet. In both cases the magnetic lengths of all quadrupoles were set to 10 mm, as was the drift distance. The electron beam energy was set to 10 MeV ($p = 5.6 \times 10^{-21}$ kg m/s), though this has no fundamental impact on the result other than scaling the focal length. To achieve total focusing for the doublet configuration, the gradients of the first and second quadrupole were set to 19.74 T/m and -20 T/m respectively. Note that any scaled version of these gradients will also result in a total-focusing configuration, with a similarly scaled focal length. There are many different configurations of the triplet that result in total focusing [74]; the configuration chosen here were +20 T/m for the first and third magnet and -39.5 T/m for the middle magnet. We immediately see one benefit of this triplet configuration: the x and y angles of the beam at the focal point are nearly the same, whereas the angles for the doublet configuration are very different.

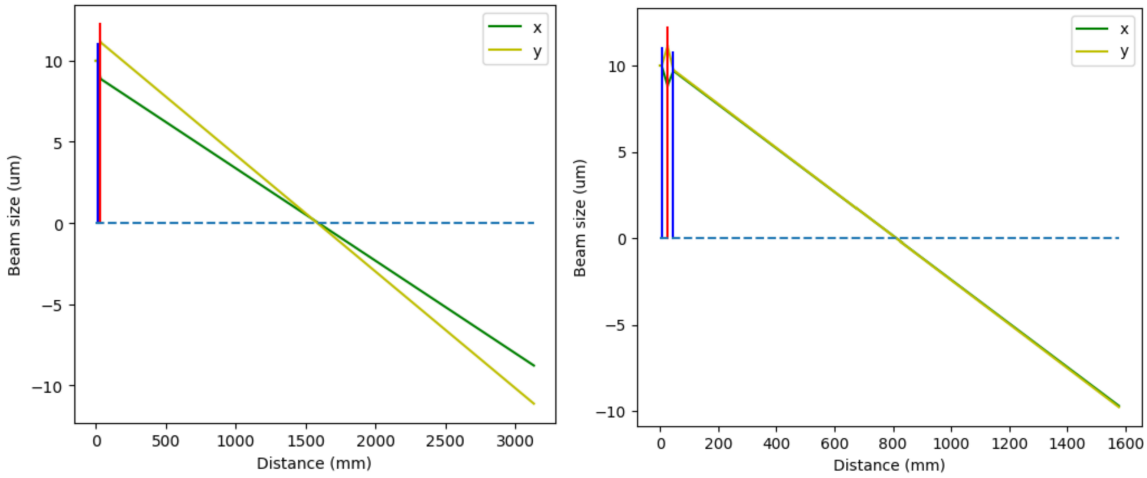

Figure 2.4: a) Total focusing with a doublet configuration. b) Total focusing with a triplet configuration.

The thin lens approximation, under which all these derivations have been performed, requires that the quadrupole is short compared to its focal length. If this is not true, then the quadrupole "lens" would be considered "thick" and the corresponding (more complicated) thick-lens matrix equations should be used [72].

These matrices can be used to track the beam through and after a focusing quadrupole.

The two-dimensional transverse beam matrix, composed of the second-order moments of the beam distribution, is expressed as

$$\sigma = \begin{bmatrix} \sigma_x^2 = \langle x^2 \rangle & \sigma_{xx'} = \langle xx' \rangle \\ \sigma_{xx'} = \langle xx' \rangle & \sigma_{x'}^2 = \langle x'^2 \rangle \end{bmatrix} \tag{2.9}$$

where x is the position of the particle and x' is the slope of the particle's trajectory in the x direction with respect to the longitudinal coordinate.

The determinant of this matrix is related to the rms beam emittance:

$$\det(\sigma) = \epsilon_{x,rms}^2 = \sqrt{\sigma_x^2 \sigma_{x'}^2 - \sigma_{xx'}^2} \tag{2.10}$$

Assuming that the quadrupole is a thin lens, the transport matrix M of the beam through the quadrupole (with a focal length l) to the screen placed a distance L away is

$$M = \begin{bmatrix} 1 & L \\ 0 & 1 \end{bmatrix} \begin{bmatrix} 1 & 0 \\ -1/f & 1 \end{bmatrix} = \begin{bmatrix} 1 - \frac{L}{f} & L \\ -1/f & 1 \end{bmatrix} \tag{2.11}$$

The beam parameters transform via a given transfer matrix M as

$$\sigma = M \cdot \sigma_0 \cdot M^T \tag{2.12}$$

and so the transformed beam size is given by σ_{11} and is given by

$$\sigma_x^2 = M_{11}^2 \sigma_{x_0}^2 + 2 M_{11} M_{12} \sigma_{x_0 x_0'} + M_{12}^2 \sigma_{x_0'}^2 \tag{2.13}$$

With this result in hand, one can measure the beam size after a given transport system and fit the beam parameters at that point in the beamline. For example, in a later section this expression will be used to fit the beam parameters after a single quadrupole. In that

experiment the beam size was measured as a function of quadrupole current (which is directly related to the quadrupole gradient and focal length), and therefore were able to fit the beam parameters $\sigma_{x_0}, \sigma_{x_0 x_0'}$, and $\sigma_{x_0'}$.

2.2.2 Prior work in microfabricated quadrupoles

There are several quadrupole devices in the literature that leverage microfabrication techniques. Microfabricated devices based on static electric fields have been used in miniature mass spectrometers [75]. Electromagnetic waves have been employed to control the transverse size in dielectric laser accelerators [76]. In that work, a photonic crystal based lens driven by a 2 μm laser was shown to be equivalent to quadrupole gradients in the MT/m range, but these structure have an extremely small gap (on the order of the optical wavelength) and are severely limited in the amount of transmitted current. They also showed that their photonic lens becomes less effective than a 500 T/m magnetic lens when the electron beam energy is above 35 MeV. This beam energy is sufficiently large for many industrial applications but not for all envisaged applications such as electron colliders or electron-beam based light sources [77]. There has been work in miniature mass spectrometry devices which require microfabricated electrostatic quadrupoles [75]. Quadrupoles fabricated directly as a printed circuit board (PCB) [78] leverage processing techniques similar to microfabrication but suffer from inferior PCB thermal characteristics and less precise intra-substrate alignment. Finally, our group previously reported a microfabricated conventional quadrupole [79] with potential for gradients of $\sim$100-1000 T/m but the magnetic length of that device is restricted to less than 1 mm due to the limits of thick film, high aspect ratio electroplating. The relatively short length means that the integrated gradient of the device is comparable to macroscale magnets. Therefore, the microquadrupole is not inherently better or stronger than large-scale devices (despite the very large gradient), but the device is noteworthy because it is designed specifically for small beams and as a result is millions of times smaller and consumes thousands of times less power than conventional quadrupoles.

2.2.3 Current sheet derivations

A derivation that will prove useful in this dissertation is the magnetic field of a finite volume of current. If the current sheet of dimensions W, H, L in the x, y, z directions respectively, is centered at the origin and has a current directed in the $+z$ direction, the magnetic field is found by directly integrating the Biot-Savart law to be:

$$B_x(x,y,z) = \frac{\mu_0 J_0}{4\pi} \sum_{p,q,r=1}^{2} (-1)^{p+q+r} \Bigg[\tilde{z}_r \log\Big(\tilde{x}_p + \tilde{l}_{pqr}\Big) + \tilde{x}_p \log\Big(\tilde{z}_r + \tilde{l}_{pqr}\Big) - \tilde{y}_q \arctan\left(\frac{\tilde{x}_p \tilde{z}_r}{\tilde{y}_q \tilde{l}_{pqr}}\right) \Bigg] \tag{2.14}$$

$$B_y(x,y,z) = -\frac{\mu_0 J_0}{4\pi} \sum_{p,q,r=1}^{2} (-1)^{p+q+r} \Bigg[\tilde{z}_r \log\Big(\tilde{y}_q + \tilde{l}_{pqr}\Big) + \tilde{y}_q \log\Big(\tilde{z}_r + \tilde{l}_{pqr}\Big) - \tilde{x}_p \arctan\left(\frac{\tilde{y}_q \tilde{z}_r}{\tilde{x}_p \tilde{l}_{pqr}}\right) \Bigg] \tag{2.15}$$

$$B_z(x,y,z) = 0 \tag{2.16}$$

where $\tilde{x}_p = x + W/2(-1)^p$, $\tilde{y}_q = y + H/2(-1)^q$, $\tilde{z}_r = z + L/2(-1)^r$, and $\tilde{l}_{pqr} = \sqrt{\tilde{x}_p^2 + \tilde{y}_q^2 + \tilde{z}_r^2}$.

Previewing the work in future sections, we will want to know the gradient between two current volumes separated by a gap distance g. Finding the transverse gradient $(\frac{dB_y}{dx}, \frac{dB_x}{dy})$ of one plate to begin will suffice as magnetic field gradients superimpose linearly. This derivative for one current sheet is computed to be

$$\frac{dB_x(x,y,z)}{dy} = \frac{\mu_0 J_0}{4\pi}\sum_{p,q,r=1}^{2}(-1)^{p+q+r}\left[\frac{\tilde{y}_q\tilde{z}_r}{\tilde{l}_{pqr}\left(\tilde{l}_{pqr}+\tilde{x}_p\right)}+\frac{\tilde{x}_p\tilde{y}_q}{\tilde{l}_{pqr}\left(\tilde{l}_{pqr}+\tilde{z}_r\right)}\right. \tag{2.17a}$$
$$\left. -\arctan\left(\frac{\tilde{x}_p\tilde{z}_r}{\tilde{y}_q\tilde{l}_{pqr}}\right)+\frac{\tilde{x}_p\tilde{y}_q\tilde{z}_r(\tilde{y}_q^2+\tilde{l}_{pqr}^2)}{(\tilde{x}_p^2+\tilde{y}_q^2)(\tilde{y}_q^2+\tilde{z}_r^2)\tilde{l}_{pqr}}\right]$$
$$\frac{dB_y(x,y,z)}{dx} = -\frac{\mu_0 J_0}{4\pi}\sum_{p,q,r=1}^{2}(-1)^{p+q+r}\left[\frac{\tilde{x}_p\tilde{z}_r}{\tilde{l}_{pqr}\left(\tilde{l}_{pqr}+\tilde{y}_q\right)}+\frac{\tilde{x}_p\tilde{y}_r}{\tilde{l}_{pqr}\left(\tilde{l}_{pqr}+\tilde{z}_r\right)}\right. \tag{2.17b}$$
$$\left. -\arctan\left(\frac{\tilde{y}_q\tilde{z}_r}{\tilde{x}_p\tilde{l}_{pqr}}\right)+\frac{\tilde{x}_p\tilde{y}_q\tilde{z}_r(\tilde{x}_p^2+\tilde{l}_{pqr}^2)}{(\tilde{x}_p^2+\tilde{y}_q^2)(\tilde{x}_p^2+\tilde{z}_r^2)\tilde{l}_{pqr}}\right]$$

To shift the current sheet center from the origin to $y \neq 0$, one simply replaces the previously given definition $\tilde{y}_q = y + H/2(-1)^q$ with $\tilde{y}_q = (y - y_c) + H/2(-1)^q$. If one desires a gap g between the plates then the proper choice of y_c is $y_c = \pm(g/2 + H/2)$, which centers the current sheet at $(0, g/2 + H/2, 0)$ and $(0, -(g/2 + H/2), 0)$. The full expression for the two-plate device, which I will call the "two current sheet quadrupole" in chapter 4, is very complicated and so is not reproduced here.

If we restrict the analysis to only the very center point between the current sheets ($x = x_c = y = z = z_c = 0$, with $y_c = \pm(g/2 + H/2)$), we obtain the following result:

$$\frac{dB_y}{dx}_{center} = B' = \frac{2\mu_0 J_0}{\pi}\left[\arctan\left(\frac{L}{W}\frac{g+2H}{\sqrt{W^2+(H+g)^2+L^2}}\right)\right. \tag{2.18}$$
$$\left. -\arctan\left(\frac{L}{W}\frac{g}{\sqrt{W^2+(H-g)^2+L^2}}\right)\right]$$

For a long device, where $L^2 \gg W^2 + (H+g)^2$, the gradient in the center of the device is given by

$$\frac{dB_y}{dx}_{center,max} = \frac{2\mu_0 J_0}{\pi}\left[\arctan\left(\frac{2H+g}{W}\right) - \arctan\left(\frac{g}{W}\right)\right] \tag{2.19}$$

CHAPTER 3

Short period undulators

I present in this chapter my work on a 1.2 mm period electromagnet undulator, termed a "mesoundulator" because the device period is between the micro-scale of microundulators [60, 80] and centimeter-scale of conventional undulators.

A concept drawing of the mesoundulator is shown in Fig. 3.1:

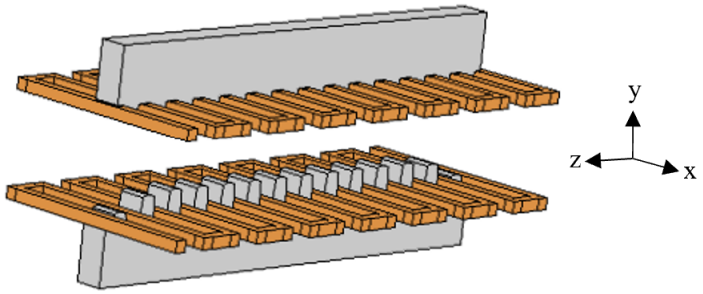

Figure 3.1: The serpentine coil mesoundulator. Copper traces are orange and yoke is grey. The copper traces are recessed into the silicon (not shown for clarity). The electron beam would enter from the left, produce undulator radiation as it traverses the undulating magnetic field, and exit to the right side. The pole tips are spaced 0.6 mm apart, giving an undulator period of 1.2 mm. The gap is nominally 300 μm, though the gap shown here is much larger for better visualization. The indicated axis is used throughout this section.

3.1 Introduction to designs

The concept of our electromagnetic mesoundulator is to microfabricate copper coil windings in silicon and interface the completed silicon die with a laser machined yoke in a fixture that holds them in the proper positions. The period was determined to be $\lambda_u = 1.2$ mm by a

J	1×10^8	A/m^2
λ_u	1.2	mm
yoke thickness	0.5	mm
copper trace height	50	μm
copper trace width	100/200	μm
g	300	μm
N_u	18	

Table 3.1: Mesoundulator device parameters. The coil (serpentine) design has a trace width of 100 (200) μm

previous project aiming to produce 1.5 Å radiation using a 1 GeV beam. In simulations the gap was set to a "standard" $g = \lambda_u/4 = 0.3$ mm; the gap must be small to minimize leakage flux to adjacent poles [81]. The yoke pole tips were shaped longitudinally (which is straightforward with our laser machining approach) to maximize the fundamental harmonic contribution to the radiation. The derivation of the exact pole tip shape is shown in Appendix A.2. The yoke is made of MuMetal, which has a relative permeability of $\mu_r \approx 8 \times 10^4$ and a saturation magnetization of 0.8 T. Due to laser machining constraints the yoke thickness was set at 0.5 mm. The yoke and undulator coils are fabricated separately, then joined Fig. 3.1 and placed together on a custom mount.

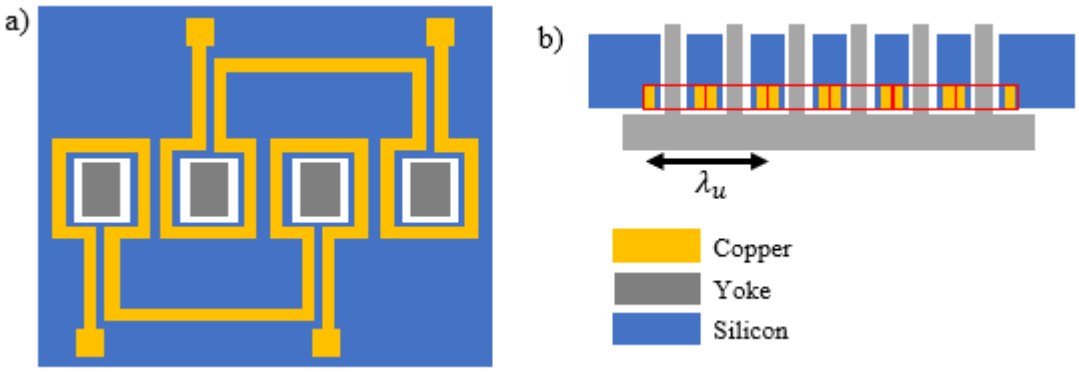

Figure 3.2: a) Top view of two-period coil design device. b) cross-sectional view of coil device. Notice how all the currents are "paired".

There are two designs, the "coil" and "serpentine" designs. The nominal geometry parameters of the fabricated mesoundulator device are as shown in Table 3.1. The coil design,

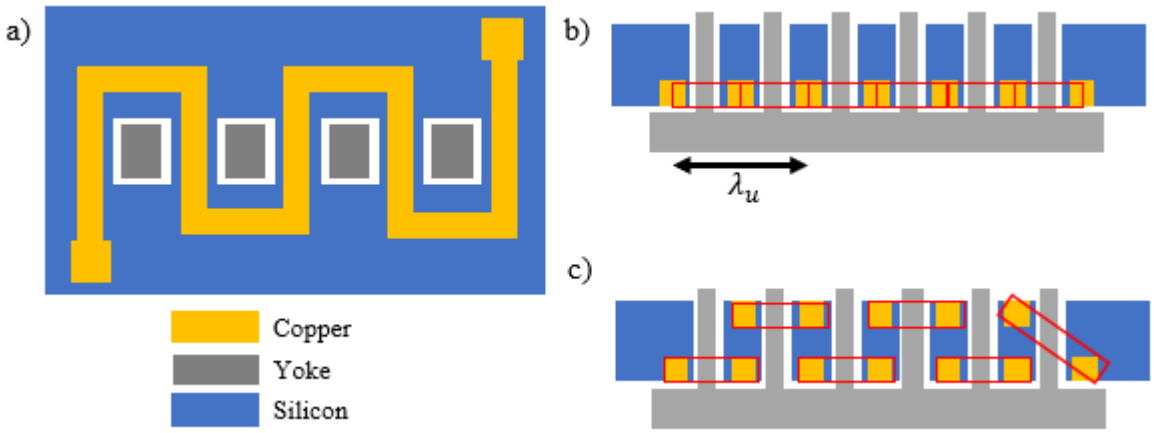

Figure 3.3: a) Top view of two-period serpentine device. b) Cross-sectional view of serpentine device. Notice that there are half currents on either side of the device that are "unpaired". c) if coils are also fabricated on the wafer backside, the currents can be "paired" again.

with the top view shown in Fig. 3.2a, is similar to typical macroscale electromagnetic undulator designs where individual coils wrap each pole. Electrically speaking, there are two strings of coils that are connected in series, meaning that there are four electrical connections as seen in the diagram by the squares that terminate each trace. The microfabricated version only has a single current loop around each yoke pole as the cross-section view in Fig. 3.2b shows. Each red rectangle contains shows the pairs of currents that excite a pole tip, and we see for this design that all currents are paired across a pole tip.

While there are many similarities between the serpentine (similar to Ref. [82]) and coil designs, there are also some notable differences. First, the serpentine design is slightly easier to address, electrically speaking, because there are only two total connections instead of four as shown in Fig. 3.3a. The more consequential difference is that the first and last traces have twice as much current as the coil design. We see in Fig. 3.3b that this extra current is not paired across a pole tip. If one were to put traces on both sides of the wafer as shown in Fig. 3.3c, then the currents can be paired properly.

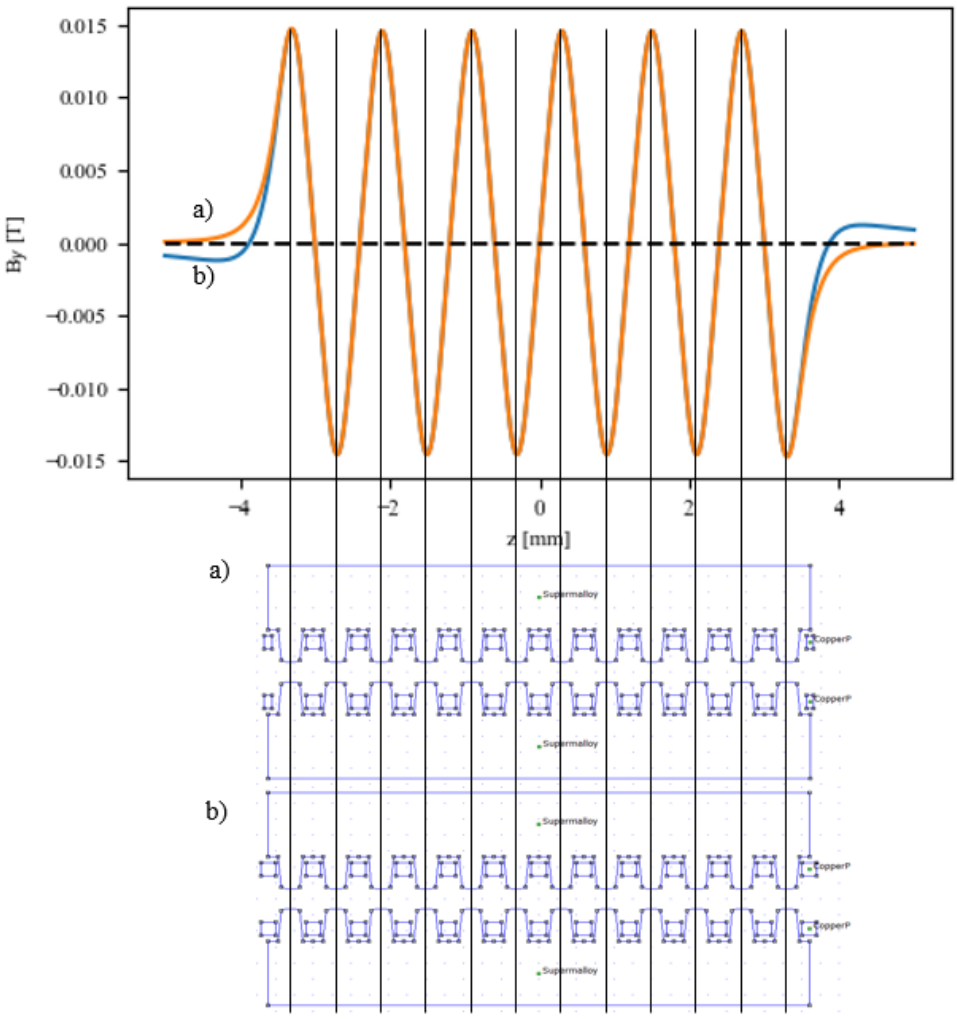

Figure 3.4: Magnetic field profile for the a) coil and b) serpentine design undulators.

magnetic field simulations in Fig. 3.4 of the two devices show why this concept of "paired" currents is consequential. The longitudinal magnetic field profiles are shown for the coil (a) and serpentine (b) undulators as calculated with a finite element solver code called Finite Element Method Magnetics [83], or FEMM, using a current density of $J = 1 \times 10^8\,\mathrm{A/m^2}$. The peaks of the undulator field are correlated with the actual pole tip peaks with the vertical black lines, and we see that the coil and serpentine designs have identical magnetic field profiles in the interior region of the undulator. However, the behavior is not the same at undulator ends. For the serpentine case, with a geometry shown in part (b), the field

has a reversal at both ends of the longitudinal magnetic field that is not associated with an actual pole tip; this "virtual" pole tip is created by the unpaired currents of the serpentine undulator, which has implications for beam steering and trajectory correction.

3.1.1 Undulator field integrals

The effect of the undulator on the electron beam trajectory is one of the most important design considerations. A first order analysis simply uses the relativistic equations of motion of an electron in a magnetic field; higher order analyses are also possible [84]. For an electron moving in the z direction in the undulator (with x, y being the horizontal and vertical directions, respectively) the equations of motion are [85]

$$x'' = -\frac{q}{\gamma m_e v_z} B_y \tag{3.1a}$$

$$y'' = \frac{q}{\gamma m_e v_z} B_x \tag{3.1b}$$

where q is the electron charge, m_e the rest mass of an electron, γ is the relativistic Lorentz factor, v_z is the electron velocity in the z direction, and B is the magnetic field in the direction indicated by the subscript. The prime indicates a derivative with respect to z. Assuming that the initial slope in both directions is zero at a point $z = z_0$ we can integrate these equations to obtain

$$x'(z) = -\frac{q}{\gamma m_e v_z} \int_{z_0}^{z} B_y(\tilde{z}) d\tilde{z} = -\frac{q}{\gamma m_e v_z} I_{1y} \tag{3.2a}$$

$$y'(z) = \frac{q}{\gamma m_e v_z} \int_{z_0}^{z} B_x(\tilde{z}) d\tilde{z} = \frac{q}{\gamma m_e v_z} I_{1x} \tag{3.2b}$$

where I_{1x}, I_{1y} are the "first" undulator field integrals. It is desirable that $I_1 = 0$, so that

electrons do not have a net trajectory slope as they exit the undulator; fortunately, this condition is automatically satisfied for the anti-symmetric undulators (which have an even number of poles) considered in this section.

By assuming that $x(z_0) = y(z_0) = 0$, we can also find the position of the electron at any point in or out of the undulator by integrating again to obtain

$$x(z) = \int_{z_0}^{z} x'(\tilde{z})d\tilde{z} = -\frac{q}{\gamma m_e v_z}\int_{z_0}^{z}\int {z_0}^{z_1} B_y(\tilde{z})d\tilde{z}dz_1 = -\frac{q}{\gamma m_e v_z} I_{2y} \tag{3.3a}$$

$$y(z) = \int_{z_0}^{z} y'(\tilde{z})d\tilde{z} = \frac{q}{\gamma m_e v_z}\int_{z_0}^{z}\int {z_0}^{z_1} B_x(\tilde{z})d\tilde{z}dz_1 = \frac{q}{\gamma m_e v_z} I_{2y} \tag{3.3b}$$

A zero-position offset after the undulator is not automatically guaranteed for anti-symmetric undulators. The offset can be adjusted by changing the magnetic field profile at the undulator ends [2]. This "end correction" for conventional electromagnet undulators is accomplished by using uniform pole heights with different current excitation for the first and last pairs of poles. This is difficult to do for the mesoundulator. Therefore, we chose to keep the pole current excitation uniform across the undulator and change the pole height. The trajectory slope inside the undulator and the beam offset at the undulator exit were optimized using FEMM by changing the pole tip height. The first and second pole tip heights (and the last pole tip and second-to-last pole tips heights) are described by $p1 * h_{pt}$ and $p2 * h_{pt}$, where $p1, p2$ are between 0 and 1 and the pole tip height from the yoke base up to the where the yoke rounding occurs (i.e., excluding the height of the rounded yoke tip) is $h_{pt} = 0.48$ mm. In the simulations the rounded tip, with a height of 0.032 mm, was always simulated, even when $p1, p2 = 0$. Therefore, the full range of full pole tip heights is 0.032 to 0.512 mm. A brute force optimization was performed by calculating the second integral for twenty values of $p1, p2$, for a total of 400 simulations. We show the results in Fig. 3.5. In Fig. 3.5a we see from a representative subset of simulations results that small changes in pole tip height can cause substantial displacements compared to the wiggle amplitude. The dashed curve from

part (a) is shown by itself in part (b). As the position is directly proportional to I_2, we see that the position is well centered in the undulator and also has very small displacement at the end. The magnetic field that produces this second integral result is shown in Fig. 3.5c, which shows the standard 1/4, -3/4, 1 structure [3, 2]. For a 1 GeV beam, the maximum displacement inside the undulator is approximately 0.15 nm for $J = 1 \times 10^8\,\mathrm{A/m^2}$.

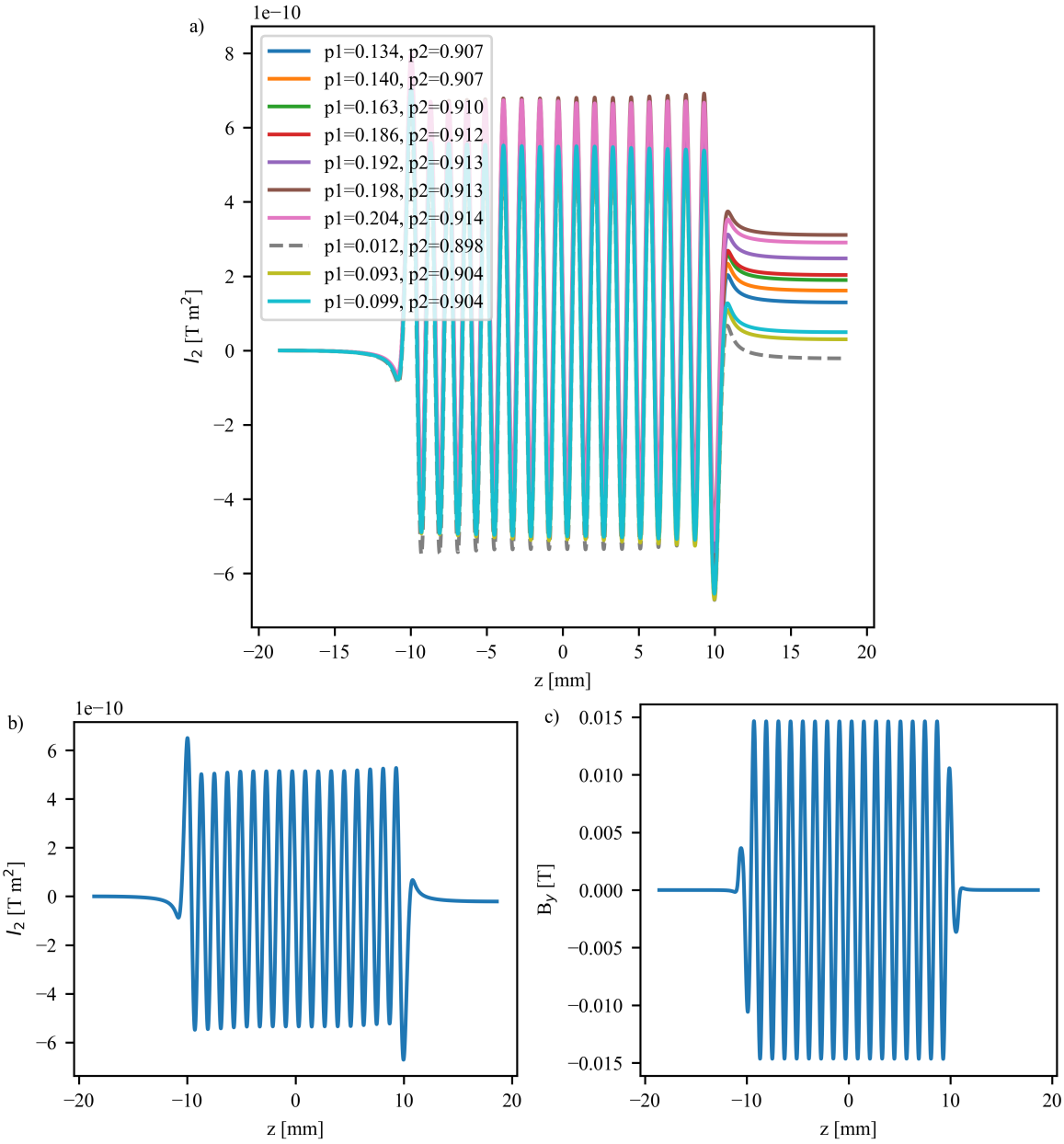

Figure 3.5: a) the second integral along the undulator length for a select set of pole tip heights of the coil design, showing that the displacement is quite sensitive to small pole height changes. b) the second integral from the dashed line in (a), showing good centering and zero displacement and angle at the undulator end. c) the longitudinal magnetic field profile that gives the second integral shown in (b), which, unsurprisingly, is the standard +1/4,-3/4,+1 pattern [2, 3].

The same type of brute force optimization was not as successful for the serpentine design.

As can be seen in Fig. 3.6a there is no solution that simultaneously has zero displacement and centered movement in the undulator. Fig. 3.6b shows the best no-displacement solution, and the corresponding magnetic field profile is shown in Fig. 3.6c. The trajectory suffers from non-centered movement in the undulator. We see that the effect of non-paired currents is significant. Despite using the same current as the coil design, the second integral, and therefore the maximum displacement, inside the undulator is more than an order of magnitude larger at the entrance and exit, which would be very difficult to correct if centered beam trajectory was required. However, for such a low-K undulator such a drastic correction may not be required; even with a beam energy of 2.5 MeV the maximum beam excursion for the serpentine undulator in Fig. 3.5 is only about 1 micron, which is likely much smaller than the beam size. For larger beam energies the maximum displacement would decrease even more. Therefore, as long as the displacement is small, it may be acceptable to have a non-centered trajectory inside the undulator.

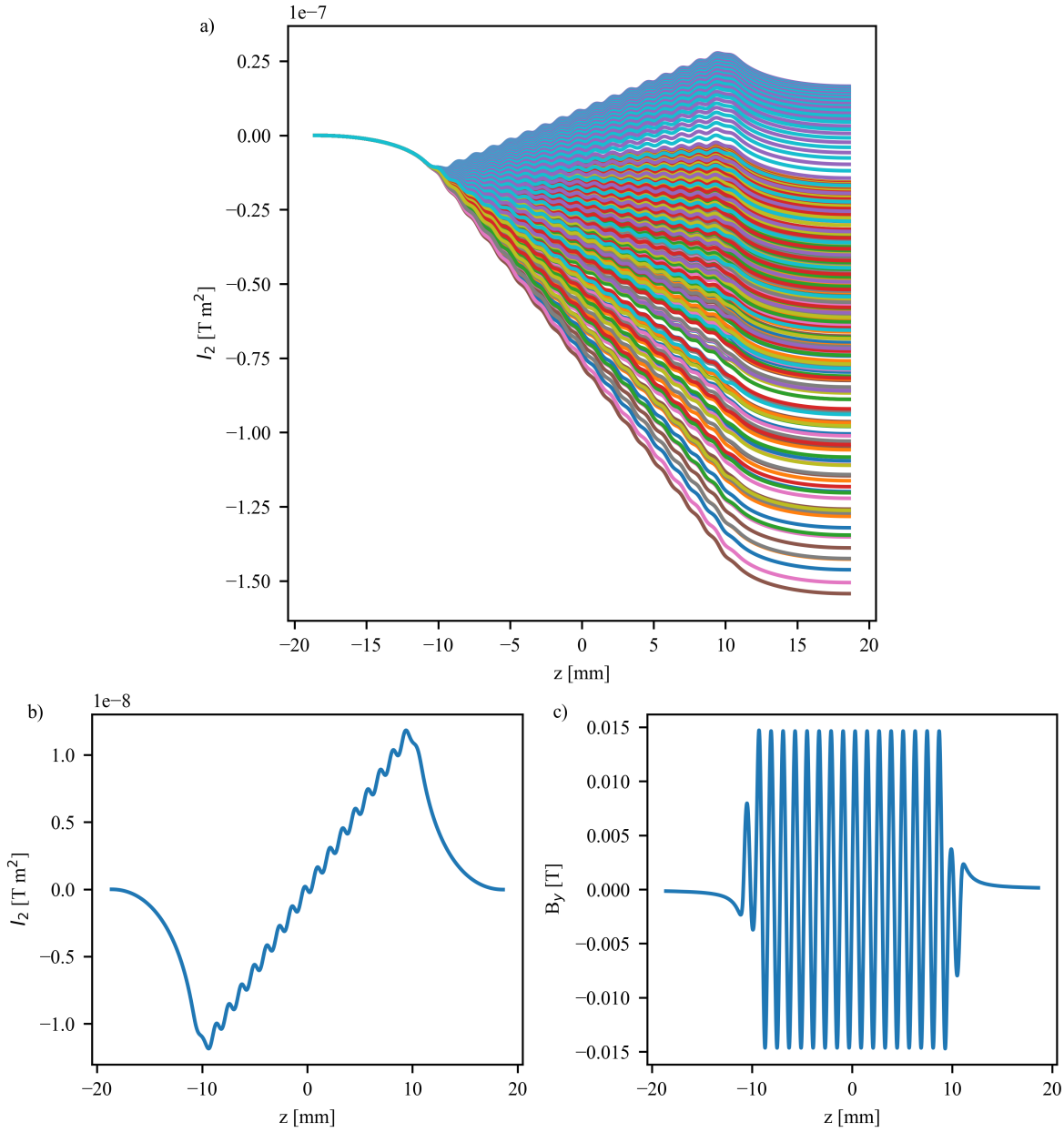

Figure 3.6: Field integrals for the serpentine design. a) the second integral along the undulator length for some $p1, p2$, where the ranges of $p1, p2 = [0, 1]$. b) the lowest overall displacement I_2 curve from part (a). c) the longitudinal magnetic field profile that gives the second integral shown in (b). Note that the first and last peaks in the magnetic field correspond to a "virtual", not physical, pole tip as explained in the body text.

3.2 Mesoundulator radiation output

The power in the central cone at the fundamental harmonic (and within the spectral bandwidth) is found to be [86]:

$$P_{n=1,central\ cone} = \frac{\pi e \gamma^2 I}{\epsilon_0 \lambda_u} \frac{K^2}{\left(1+\frac{K^2}{2}\right)^2} f(K) \tag{3.4}$$

where $f(K) = J_0(x) - J_1(x)$ and $x = K^2/\left(4+2K^2\right)$. Over all angles, the power of the fundamental harmonic within the spectral bandwidth is:

$$P_{n=1,all\ angles} = \frac{\pi e \gamma^2 I N_u}{3\epsilon_0 \lambda_u} \frac{K^2}{\left(1+\frac{K^2}{2}\right)^2} \tag{3.5}$$

The total power, over all angles, wavelengths, and modes of an undulator is given by [87]:

$$P_t = \frac{\pi e \gamma^2 I N_u K^2}{3\epsilon_0 \lambda_u} \tag{3.6}$$

Table 3.2 presents a comparison of a typical undulator at the Advanced Photon Source (APS) and a short period (1 mm period) undulator of the same total length in a lower energy accelerator with similar operating conditions. We see that the power in the central cone of the mesoundulator is very low, but that nearly all the power of the beam is concentrated in the fundamental harmonic, whereas the conventional undulator has significant power in higher harmonics, which is often filtered out and is wasted. From the equations above it seems that a low energy electron beam (low γ) coupled with a short period undulator (low K) would produce orders of magnitude less useful power than conventional wigglers in use today. However, the large increase in the number of periods and concentration of power in the first harmonic work together such that the mesoundulator produces only one order of magnitude less photons, not several orders of magnitude.

	APS Undulator	Mesoundulator
Energy [GeV]	7.0	0.98
γ	13700	1920
Average current [mA]	100	100
Beam size (x,y) [μm]	320, 50	320, 50
Beam divergence (x,y) [μrad]	23,7	23,7
Undulator period [mm]	33	1.0
Undulator length [m]	2.4	2.4
K	1.0[a]	0.037
Radiation wavelength [nm]	0.13	0.13
Frequency bandwidth [%]	1.4	0.04
Central cone angle [microradian]	12.8	10.6
Total power, central cone, n=1 [W][b]	12	0.03
Total power, all angles, n=1 [W][c]	345	23.33
Total power, all angles, all harmonics [W][d]	780	23.36
Brilliance [(photons/s)/mm^2 mrad^2 (0.1% BW)]:	4.4×10^{18}	4.7×10^{17}

Table 3.2: Comparison of undulator comparison for synchrotron radiation production.
Note *a*: this is the undulator parameter that corresponds to the total power in the central cone in the table; the K value for this undulator can increase up to 2.76, resulting in a total power of 5914 W as calculated by Eq. 3.6.
Note *b*: computed with Eq. 3.4.
Note *c*: computed with Eq. 3.5.
Note *d*: computed with Eq. 3.6 and verified with the software SPECTRA [4].

3.3 Simulations

3.3.1 Thermal

Since the mesoundulator is inherently a low-K device, the magnetic field, and therefore the current density, needs to be optimized considering the thermal constraints of the device. Thermal simulations performed in COMSOL Multiphysics are presented in Fig. 3.7, showing the steady-state temperature rise of the mesoundulator as a function of current density assuming that the back plane of the silicon die is held at room temperature. We see that at $J = 1 \times 10^9\,\mathrm{A/m^2}$ the temperature rose only about 6 K, but thermal runaway occurs at only marginally higher current densities. Consequently, a current density of $J = 1 \times 10^9\,\mathrm{A/m^2}$ was used for the magnetic field simulations. The thermal response of the coil design was very similar and so is not shown here.

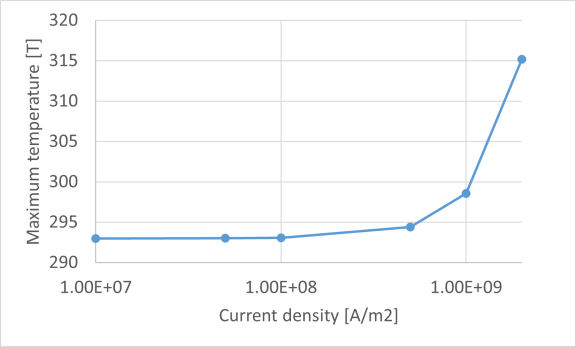

Figure 3.7: Plot showing the maximum temperature within the die for the serpentine design at each current density.

3.3.2 Magnetic field simulations

Various magnetic field simulations were carried out to characterize the expected mesoundulator performance. All simulations were performed with a gap of 0.3 mm between the pole tips, a current density of $J = 1 \times 10^9\,\mathrm{A/m^2}$, and with standoff distances of 50 μm and 1500 μm for the coil and serpentine designs respectively. Unfortunately, all attempts at 3D

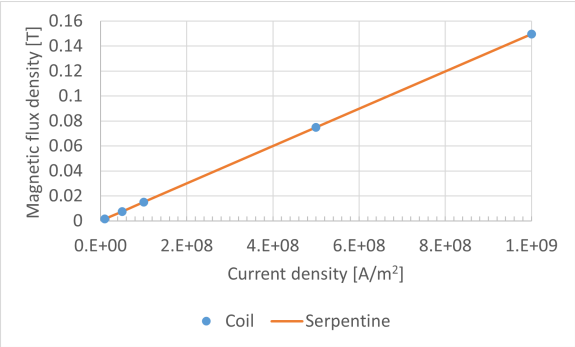

Figure 3.8: 3D COMSOL simulation showing the magnetic field in the center of the gap between two pole tips as a function of current density for the coil and serpentine designs.

modeling with the actual magnetization curve of MuMetal were unsuccessful due to solver convergence issues, so a constant relative permeability of $\mu_r = 80000$ was assumed. The magnetic field in the yoke was monitored to make sure that it did not reach the saturation magnetization. The maximum field in the middle of the gap is shown in Fig. 3.8, which is about 0.15 T for $J = 1 \times 10^9\,\mathrm{A/m^2}$. As the magnetic material did not saturate for this range of current densities the linear dependence of field on current is expected.

The longitudinal variation, i.e., along the beam axis, is important to undulator design and is shown for both designs in Fig. 3.9. This 3D result matches well with the 2D result shown in Fig. 3.4. We see that, as before, the fields of the coil and serpentine designs match well except for the outer two periods on both ends. This is due to the unpaired currents concept described in a previous section.

The transverse profile of the magnetic field in the gap above one of the central pole tips is plotted in Fig. 3.10 across the pole tip width, 0.5 mm. We see that the transverse magnetic field profile of the coil design is symmetric, but due to the 3-sided excitation of the serpentine coils the magnetic field profile is not symmetric. The next section discusses this phenomenon further.

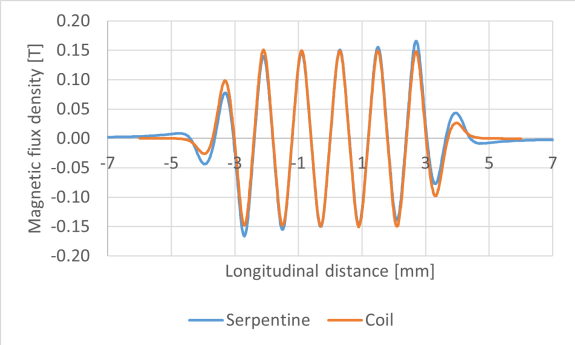

Figure 3.9: 3D COMSOL simulation showing the longitudinal variation of magnetic flux density for coil and serpentine designs in the gap center.

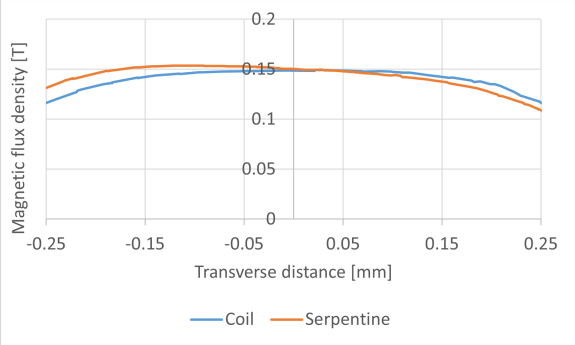

Figure 3.10: Transverse variation of magnetic flux density for the coil and serpentine designs in the gap center between two pole tips.

3.3.3 Strong focusing configuration

A potential drawback of the serpentine is that the traces are asymmetric with respect to a single pole, in the sense that the pole has currents on only three of the four sides. This results in a magnetic field gradient across the gap region, superimposed over the dipole field, whose magnitude is inversely proportional to the distance between the yoke and side trace. To reduce this effect, one could lengthen the meandering path so that the side currents are far away from the yoke, and thus minimize their influence, or one could put traces on both sides of the wafer as discussed in Fig. 3.3c. Alternately, one could *use* this transverse gradient as built-in strong focusing of the electron beam.

Electron beam focusing is needed to maintain the optimal small electron beam size inside the undulator. In most cases, this focusing is accomplished by quadrupoles placed between undulator sections in a "lumped" focusing scheme. While this works for many applications, there are some applications that require strong focusing along the entire length of the undulator, not just between segments. One example is the VISA FEL [88], where the design called for additional magnets in the undulator bore to superimpose a quadrupolar field with a gradient of 33 T/m upon the oscillating undulator dipole fields [89]. This built-in focusing field fulfills a similar distributed focusing function. In practice this could be visualized as a series of short undulator sections that have alternating gradient polarities that forms a pseudo-FODO lattice, focusing the beam inside the undulator itself and reducing the need for external quadrupoles to focus the beam. Pole tip saturation could negatively impact the effect of such a focusing mechanism.

Varying the distance between the side traces of the serpentine undulator and the undulator yoke should change the gradient of the quadrupole field. This distance is shown by the arrow in Fig. 3.11a. The results of varying this standoff distance from 0 to 3 mm are shown in Fig. 3.11b, including a table that shows the dipole and quadrupole components of the transverse magnetic field. We see when the side trace is close to the yoke that the slope

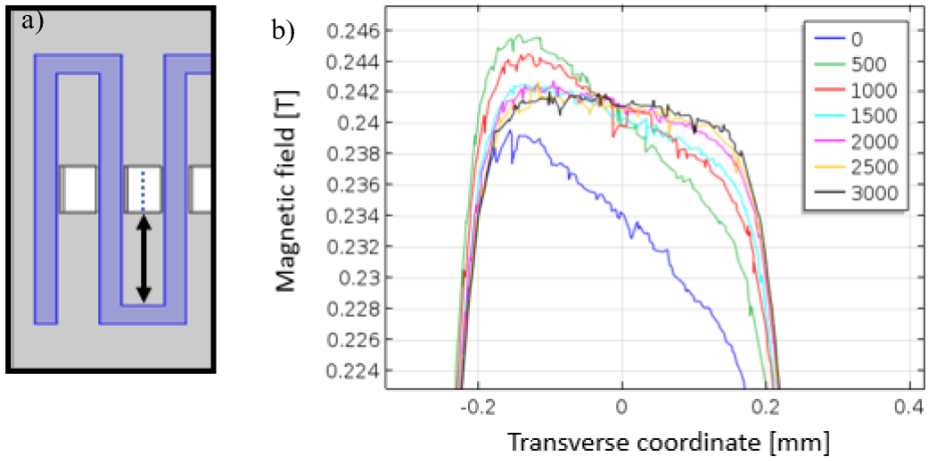

Standoff distance	Magnetic field gradient [T/m]	Dipole field [T]
0 μm (red)	46	0.233
500 μm (green)	42	0.239
3000 μm (black)	6	0.241

Figure 3.11: a) schematic of serpentine standoff distance. b) Plot showing the magnetic field along the dashed line from part (a), in the mid-plane of the full mesoundulator. Each curve is for a different side current trace standoff distance; the legend has units of microns. The table gives the dipole and quadrupole field strengths of selected standoff distances.

of the magnetic field is large, resulting in a gradient of 46 T/m within the central 0.2 mm area, but the gradient decreases to 6 T/m at a standoff distance of 3 mm. We can also see that the dipole field suffers somewhat at small standoff distance but that the value recovers quickly. The data are somewhat noisy because of meshing difficulties in the high-aspect ratio 3D mesoundulator structure.

3.4 Fabrication

The mesoundulator fabrication process is shown in Fig 3.12. The fabrication process of the single-coil and serpentine coils is the same; indeed, the two devices were fabricated on the same wafer. The trace width is determined by the photolithography mask design and the trace thickness is determined by the deep reactive ion etching (DRIE) step. It is desirable to have the thickest traces possible since they allow more current through the device, but the

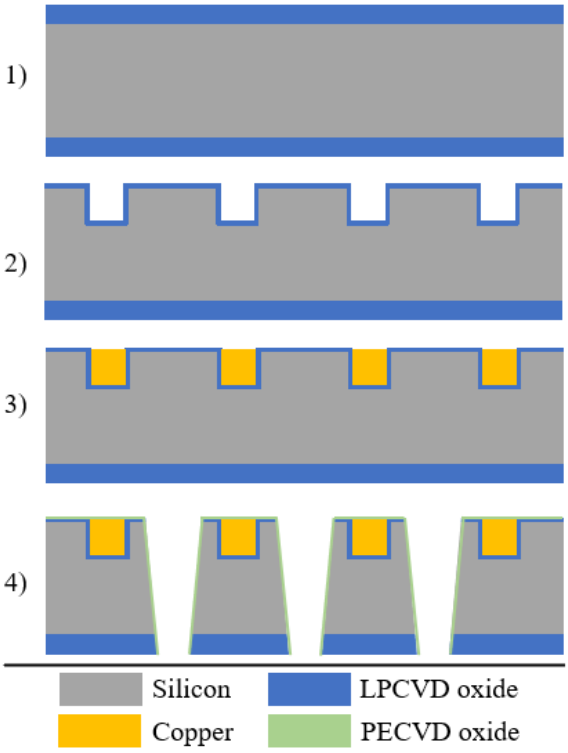

Figure 3.12: Mesoundulator fabrication process. 1) Deposit silicon oxide via LPCVD to act as a hard mask, 2) Etch hard mask and silicon to the desired depth, then deposit LPCVD silicon oxide again for electrical insulation. 3) Deposit electroplating seed layer and electroplate copper. Polish copper to be flush with silicon. 4) Fabricate holes for pole tips, either using laser machining (which introduces a taper as shown) or DRIE, then electrically isolate the sidewalls with PECVD silicon oxide.

electroplating step become increasingly more difficult and defect prone as the aspect ratio increases. Therefore, a 1:4 height/width ratio (50 μm depth, 200 μm width) was deemed appropriate for the proof-of-concept serpentine device.

The yokes were laser cut (Oxford Lasers) from 0.5 mm thick sheets of Mu-Metal purchased from Magnetic Shield Corporation. Laser cutting damages the magnetic properties of the nearby material [90], which can be "healed" via annealing (performed by Magnetic Shield Corporation). The magnetic properties of a single square coupon (3 mm x 3 mm x 0.5 mm) of laser-processed yoke material were characterized along one of the long axes before and after annealing by measuring the MH curve using a vibrating sample magnetometer

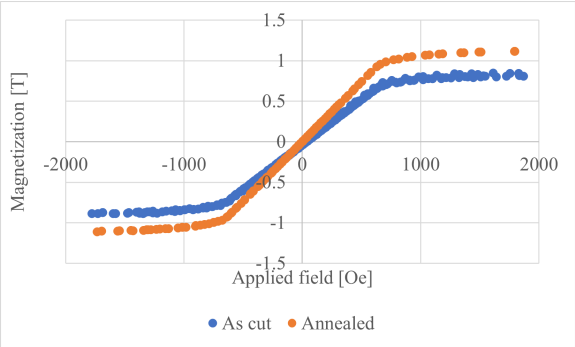

Figure 3.13: The magnetication curve for a single square piece of yoke material, before annealing and after annealing. This was measured using a VSM.

(Lakeshore VSM model 7304), as shown in Fig. 3.13. We see that the maximum magnetization increased from 0.89 T to 1.1 T, and the relative permeability also increased from $\mu_r = 900$ to 1100). It is curious that the maximum magnetization increased, and it is likely this is due to changes in the VSM experimental setup. However, the clear improvement in permeability validates the usefulness of the annealing step in restoring magnetic properties. The peak magnetization and relative permeability are not in line with the magnetization and permeability values provided by the manufacturer of 0.8 T and 10^6, respectively, but these discrepancies could be in part due to limitations of the VSM [91]. These curves have not been adjusted for demagnetization, which is inherent in all VSM measurements; such a correction can be problematic [92] but always results in a higher permeability. There may also be small imperfections in size measurement, composition, and VSM calibration that could cause errors.

The copper traces are made using typical microfabrication techniques in a silicon wafer. A 2 μm thick wet thermal oxide was grown at 1100 ^{o}C (Tystar Titan II) for a hard mask and patterned using photolithography. All lithography was done using the following process:

1. spin AZ 1529 positive photoresist at 4000 RPM for 30 seconds,
2. 50 second soft bake at 90 C,
3. 112 J/cm^2 exposure,

4. development in AZ Developer (typically $\sim$ 60 s),

5. descum using Matrix Asher for 60 second at 50 C at 100 watts.

After etching the hard mask (STS Advanced Oxide Etcher), the photoresist was removed with acetone and the deep silicon etch was performed (Plasmatherm DSE III FDRIE). This is the step that defines the thickness of the embedded copper trace, which was 50 μm for the device shown here but could be made deeper to fabricate taller traces to handle more current. A 1 μm wet thermal oxide was then grown to serve as electrical isolation. A seed layer consisting of 30 nm titanium for adhesion, 300 nm copper, and 30 nm titanium to protect the copper from oxidation was then sputtered (CVC 601). Before electroplating the capping layer of titanium was removed by dipping in 1% hydrofluoric acid for approximately 30 seconds until the copper was exposed, then immediately prepared the wafer for electroplating. We used the Technic Elevate Cu 6320 commercial bath at a current density of 50 A/m^2. This is a relatively low current density that results in slow plating ($\sim$ 7μm/hr), but also lower stress deposits and better step coverage (also called "high throw"). As the electroplating coats the entire wafer in copper, chemical mechanical polishing (Logitech CDP, AlumTX 100 slurry) was used to grind and polish the copper down to silicon level. This process of etching trenches, depositing seed layers, electroplating, then polishing is known as the Damascene process. At this point the copper traces are finished. A wafer processed to this point, with traces only on one side, is shown in Fig. 3.14 alongside the laser-machined yoke. If desired, one could repeat this process on the backside of the wafer to roughly double the magnetic field in the undulator gap. I will note, however, that I have had problems with the backside etch step in other, similar processes because the copper traces on the front side of the wafer change the cooling distribution across the wafer. This causes incomplete etching of the passivation layer, causing micromasking that leads to unacceptable roughness at the trench bottom. It may be possible to avoid this issue by etching both trenches before any seed layer deposition or electroplating step, but this process flow has not been tested.

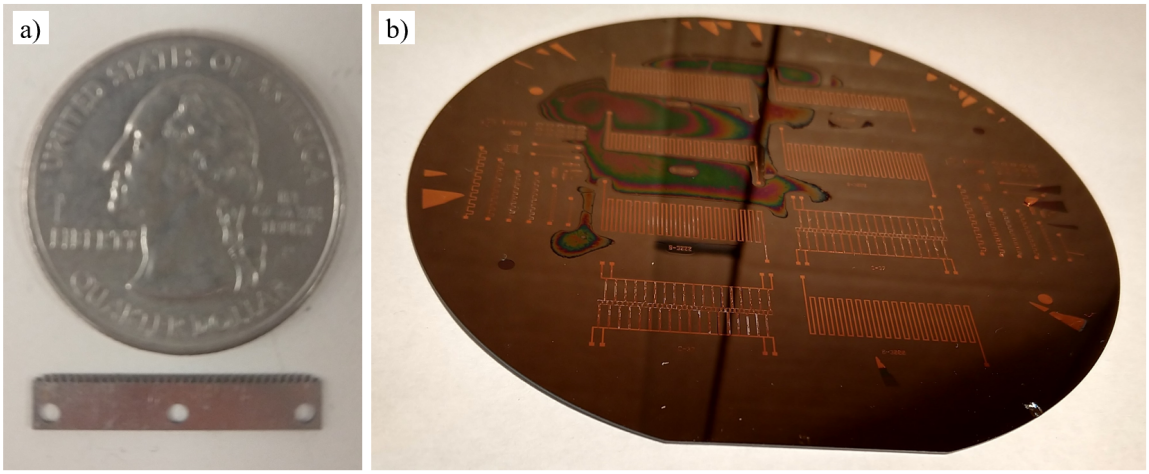

Figure 3.14: a) fabricated yoke next to a quarter. b) fabricated wafer ready for final yoke hole drilling step.

The yoke holes were fabricated using laser machining (LPKF Protolaser U4). This tool scans the laser beam over a scan field with a high precision mirror, with positioning accuracy of 20 μm. However, if the entire sample is larger than a single scan field, then the table itself will move the sample to a new scan field. The table positioning accuracy is much worse than the laser positioning accuracy. This is important to take into consideration because the spacing of the laser drilled holes may not be uniform across the device if the device is larger than a single scan field.

The desired hole had dimensions of 350 μm x 550 μm, which is just large enough for the 330 μm x 500 μm yoke pole pieces. This only leaves about 50 μm between the copper traces to position the laser beam, but good alignment was achieved as shown in Fig. 3.15a. Fig. 3.15b is a closer view of a laser drilled hole, showing smooth sidewalls. However, only 17 periods fit inside a single scan region. Consequently, the last two holes were drilled from the adjacent scan field which involved a coarse stage movement. We see the resulting misalignment in Fig. 3.15c. The left hole was in the scan from which the majority of the holes were drilled. The right hole was drilled from the adjacent scan field. We can see that the left hole is centered between the copper traces, but the right hole is adjacent to the right trace. This misalignment means that the yoke cannot be optimally inserted as can be seen

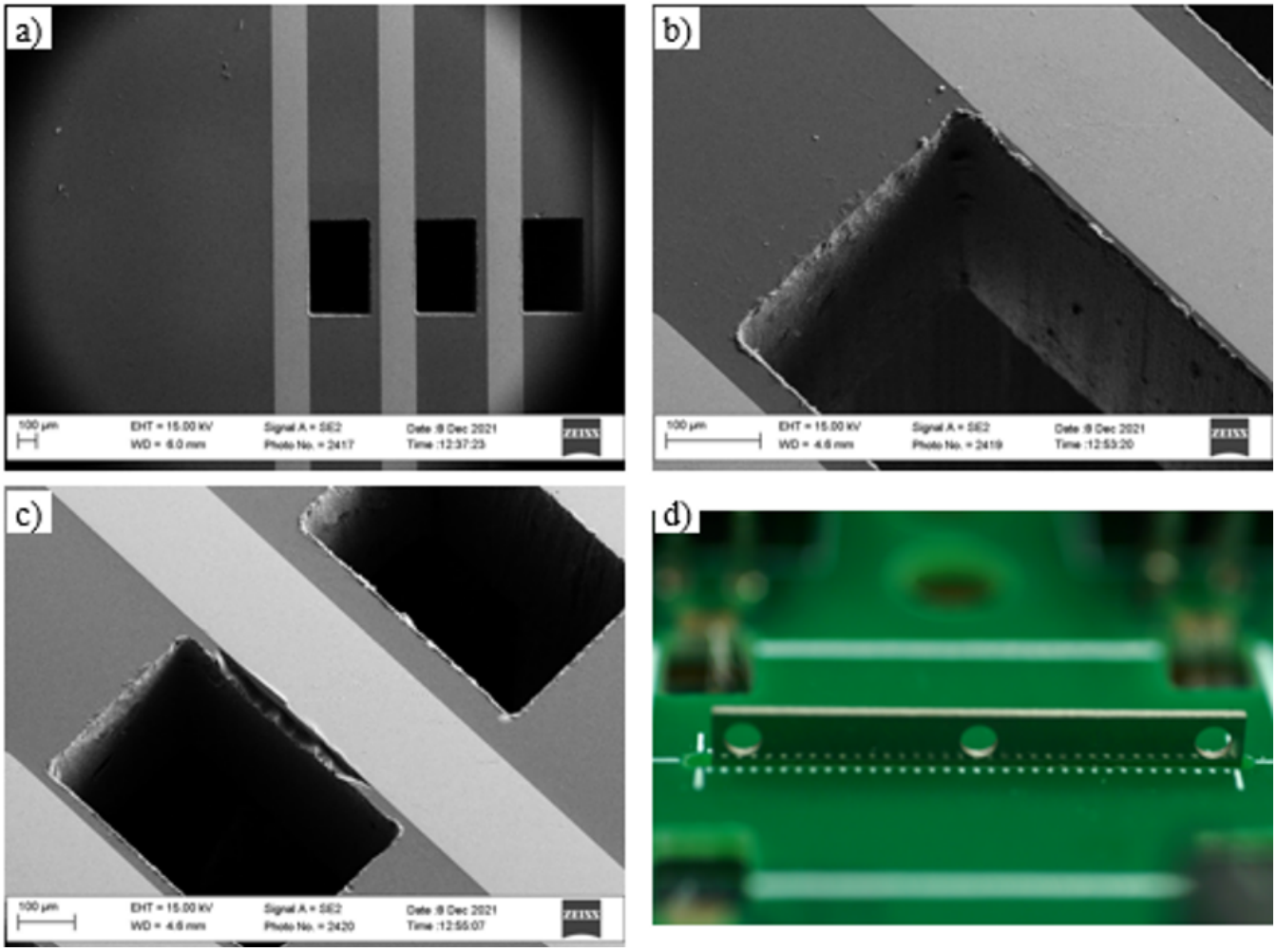

Figure 3.15: a) scanning electron microscope image of wide area of mesoundulator. b) close-up on sidewalls of another laser-drilled hole. c) two laser drilled holes from adjacent scan fields, showing the resulting fabrication errors. d) since the last period (on the left) was laser-drilled from an adjacent scan field the yoke cannot be fully inserted on that side.

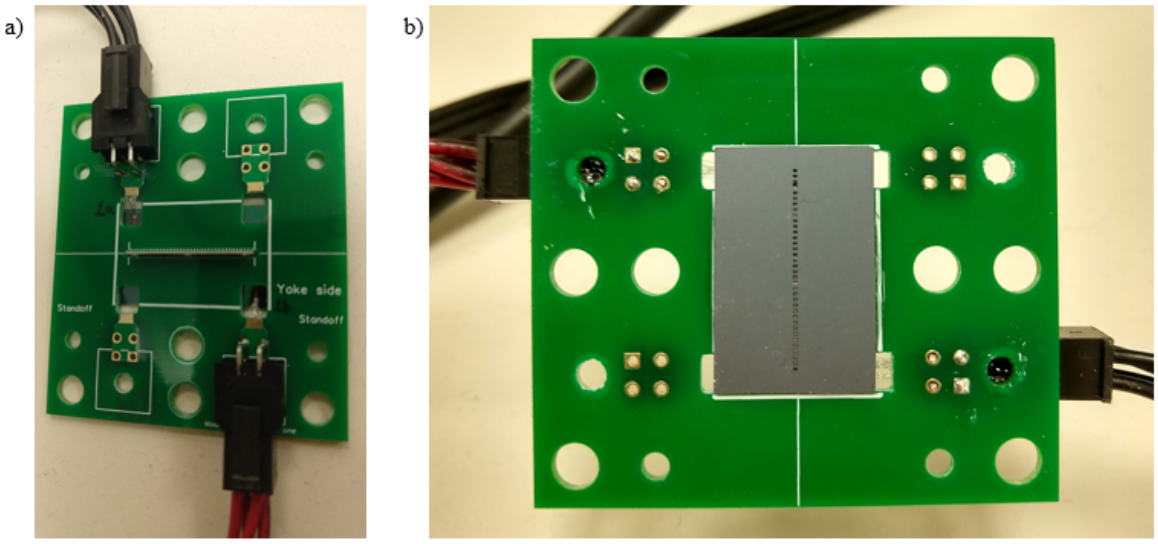

Figure 3.16: a) backside of PCB, with the yoke and electrical wirebonded connections visible. b) the frontside of the PCB. This is the part that is "inside" the undulator gap.

in Fig. 3.15d, where the right side is slightly more inserted than the left.

After laser machining, 800 nm of PECVD oxide was deposited on the wafer frontside to electrically insulate the drilled yoke holes and the copper traces. The copper pads are also insulated after this step; the oxide must be etched off the pads using a lithography and buffered oxide etch prior to wire bonding. The silicon die is mounted with the copper traces facing the yoke to 1) more easily facilitate electrical connections via wirebonding and 2) seat the copper coils near the base of the pole tips. The mounted devices are shown in Fig. 3.16.

Wirebonding facilitated electrical connection from the PCB to the mesoundulator. Each wirebond can only handle about 250 mA of steady current, so a large number of wirebonds is needed to use high currents. As shown in Fig. 3.17, only few wirebonds adhered to some pads (seen in (a)), while other pads permitted many more connections (seen in (b)). These devices were fabricated simultaneously on the same wafer, so the most probable cause is the unoptimized oxide etch step to remove the pad oxide.

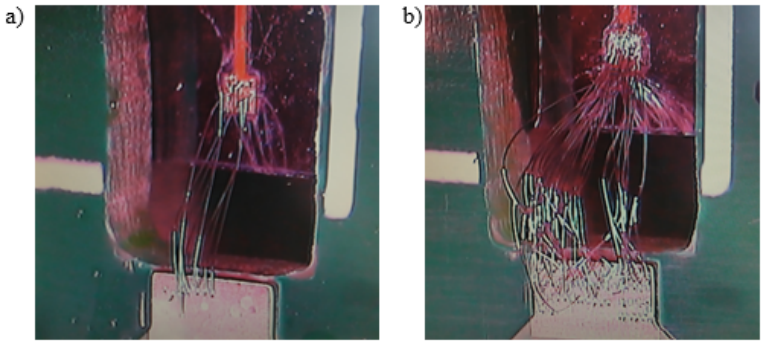

Figure 3.17: a) on this pad, most wirebonds popped off as they were applied, leaving only a few viable wirebonds. b) On other pads, many wirebonds adhered without issue.

3.5 Experimental measurements

There are multiple methods to characterize an undulator:

1. Pulsed wire: the low K value makes this measurement difficult.

2. Electron beam test: the low K value ensures that any beam modulation would be very small. The total optical power is given by $P_t = \frac{\pi e \gamma^2 I N_u K^2}{3\epsilon_0 \lambda_u}$, which assuming PEGASUS-like parameters [93] and a single mesoundulator segment of 18 periods results in a power output of $\approx 100\mu$W, which may not exceed background noise such as bremsstrahlung [94].

3. Hall Probe: the narrow 0.3 mm gap precludes scanning the fully assembled mesoundulator but scanning one half of the device is feasible.

Therefore, half of a serpentine undulator was scanned with a Hall probe to characterize the magnetic field. Because the device was mounted on a thermally resistive PCB, the maximum current that could be applied to one undulator half was 1 A ($J = 1 \times 10^8$ A/m^2). The magnetic field sensor was positioned so that it was nearly touching the silicon die, which means that the distance from the sensor to the pole tips was about 1.15 mm. The results

are shown in Fig. 3.18. The left column (a,c,e) are the experimentally measured values for B_x, B_y, and B_z, while the right column (b,d,f) are the simulated data from COMSOL for the same geometry. Referring back to the coordinate system in Fig. 3.1, the B_x field is horizontal in the gap, B_y is the sinusoidal dipole wiggler field, and B_z is the longitudinal field (to pass flux between adjacent pole tips, for example). Qualitatively, the plots show many of the same features, such as modulation in both B_y and B_z (the B_z component will be canceled on axis when both undulator halves are present), and that the magnetic field is roughly the correct order of magnitude. We can also see the yoke tips clearly in the B_y and B_z data as brighter spots along $y = 0$.

Fig. 3.19 shows data taken along the black dotted lines from Fig. 3.18. We again see that the experimental and simulated devices share many of the same features: A bulge in B_x, oscillations of approximately the same magnitude in B_x and B_z, and large changes in magnetic field near the ends of the undulator, near 0 mm and 26.2 mm. Disagreements between experiment and simulation can be attributed to misalignments in the magnetic measurement system and fabrication imperfections, including the yoke misalignment discussed earlier.

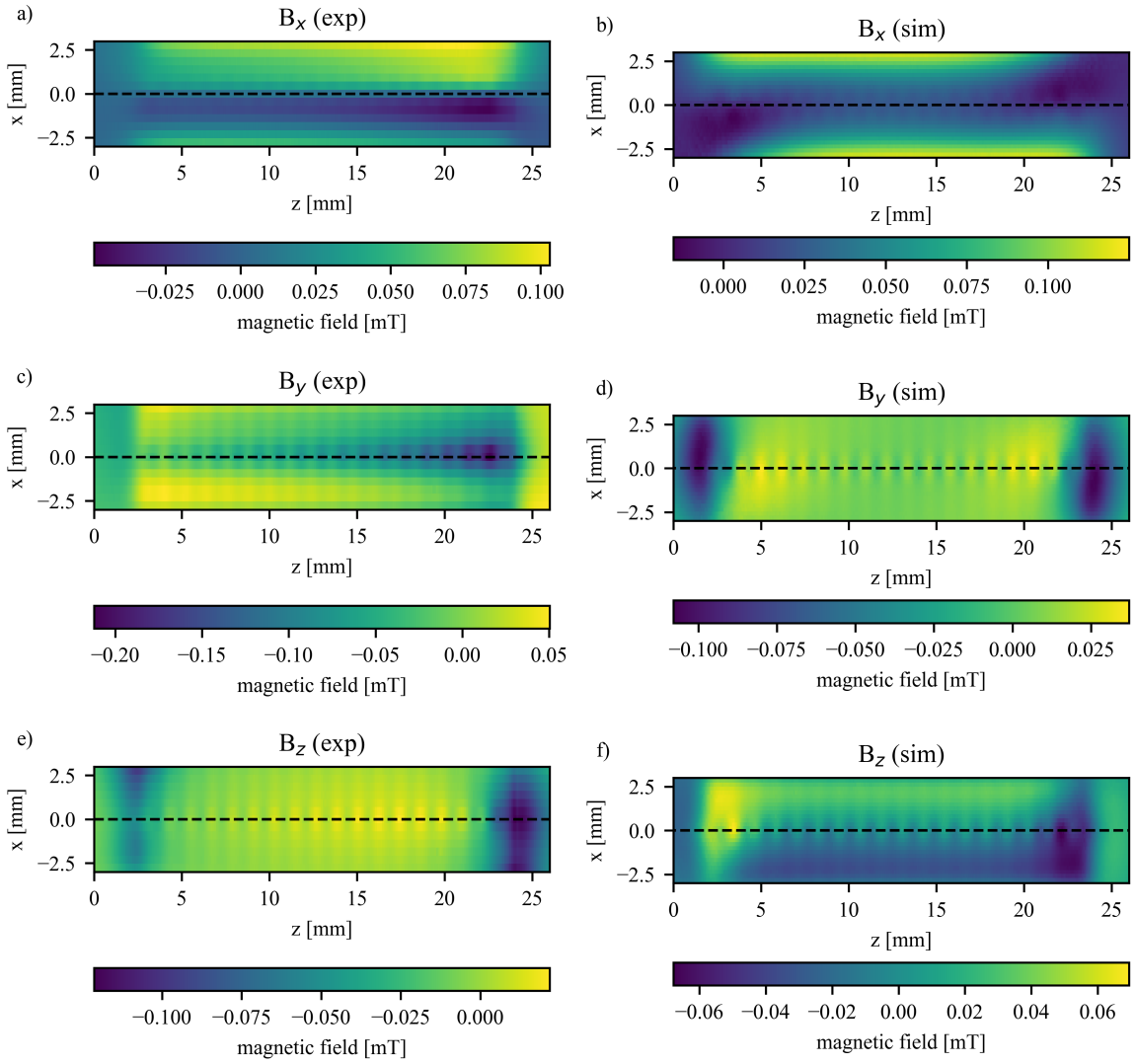

Figure 3.18: Magnetic field measurements (left column, parts a,c,e) and simulations (right column, parts b,d,f) of one-half of a serpentine mesoundulator with a yoke. The current was 1 A and the distance from pole tips to sensor was approximately 1.15 mm. The dashed lines correspond to data shown in Fig. 3.19.

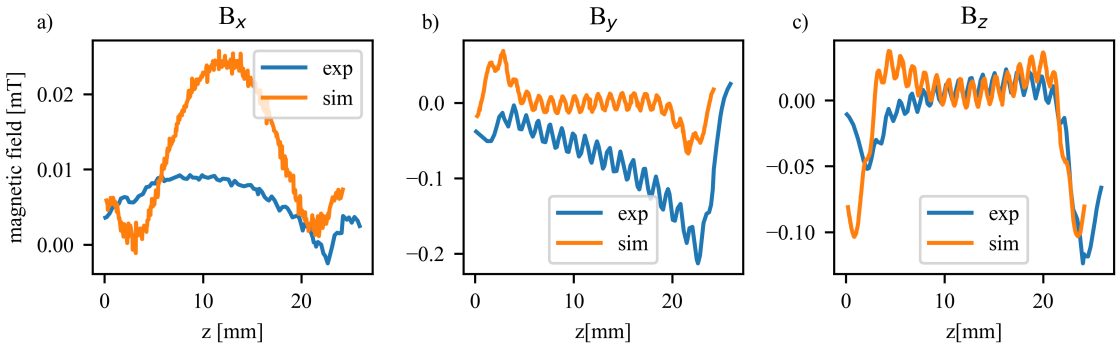

Figure 3.19: Lineouts of the magnetic field from Fig. 3.18

The same scans were performed without the yoke, shown in Figs. 3.20 and 3.21. We immediately note that while the data still do not match simulation perfectly in the yokeless case either, the agreement is much better. As before we compare experimental data and simulation lineouts in Fig. 3.21, which shows improved agreement as compared to the yoked case. This is intuitive - the yoke is known to be misaligned, and by design the yoke dominates the magnetic field contributions. We can also see the effect of the yoke in the wiggle amplitude of the B_y field. In the experimental data of the yoked and unyoked case the average peak to trough variation is approximately 0.03 and 0.005 mT, respectively, and the simulation data also show approximately a factor of 10 difference between the yoked and unyoked cases.

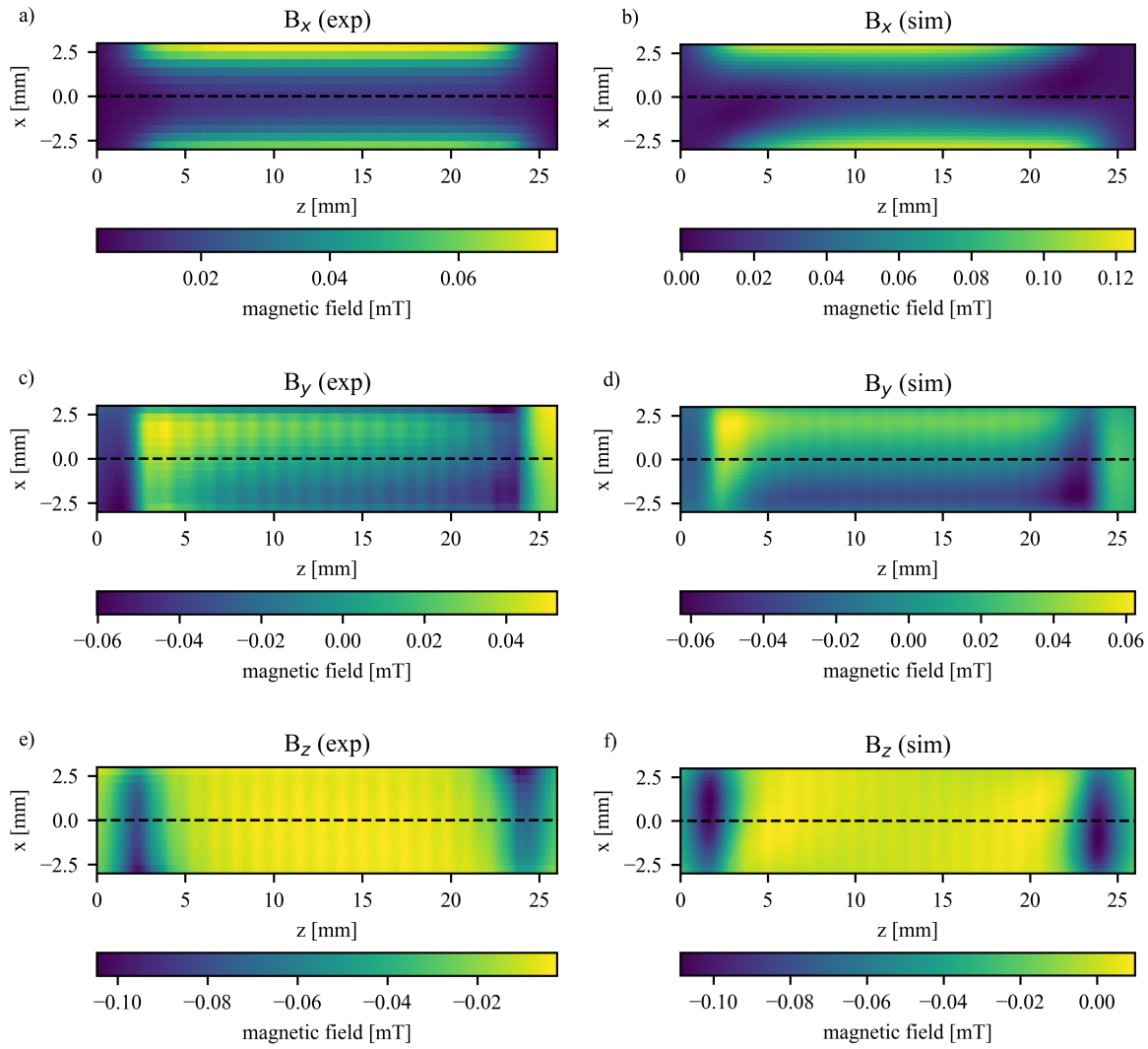

Figure 3.20: Magnetic field measurements (left column, parts a,c,e) and simulations (right column, parts b,d,f) of one-half of a serpentine mesoundulator without a yoke. The current was 1 A and the distance from pole tips to sensor was approximately 1.15 mm. The dashed lines correspond to data shown in Fig. 3.20.

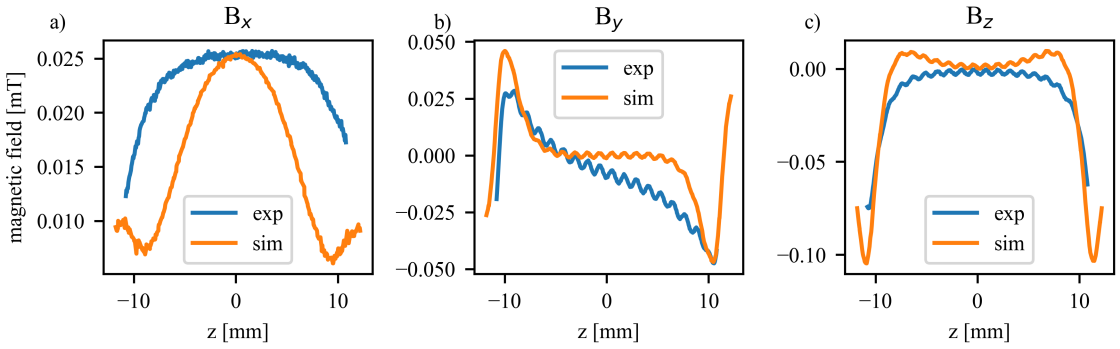

Figure 3.21: Lineouts of the magnetic field from Fig. 3.20

3.6 2.7 mm short period hybrid undulator

Hybrid undulators are a very common undulator type, and so it is useful to investigate the ramifications significantly shortening the period. In this work a 2.7 mm undulator was conceptualized and tested. In the interest of cost, commercially available permanent magnets (PMs) from K&J Magnetics were used, of dimensions 1/2" x 1/4" x 1/32". A 0.5 mm as-rolled (i.e., unannealed) permendur sheet from Goodfellow Corporation was cut using a waterjet form 5.3 mm x 7 mm rectangular pole tips. These dimensions were optimized using RADIA simulations. The waterjet cutting technique does not produce as much heat as other cutting methods, especially for hard alloys such as vanadium permendur, and so preserves the magnetic properties of the material better without annealing. In this case, however, because of the amount of hard work that occurs during the rolling process, the magnetic properties are quite poor - we measured the permeability to be approximately 6 using the VSM (the maximum permeability for vanadium permendur is typically cited as $\mu_r \approx 1E4$). The PMs and permendur pole tips were assembled in a 3D printed mold, shown in Fig. 3.22a. Spacers of various thicknesses were used to change the gap, and field measurements were performed with a FW Bell 5180 Hall probe mounted on an automated scanning stage, shown in Fig. 3.22b.

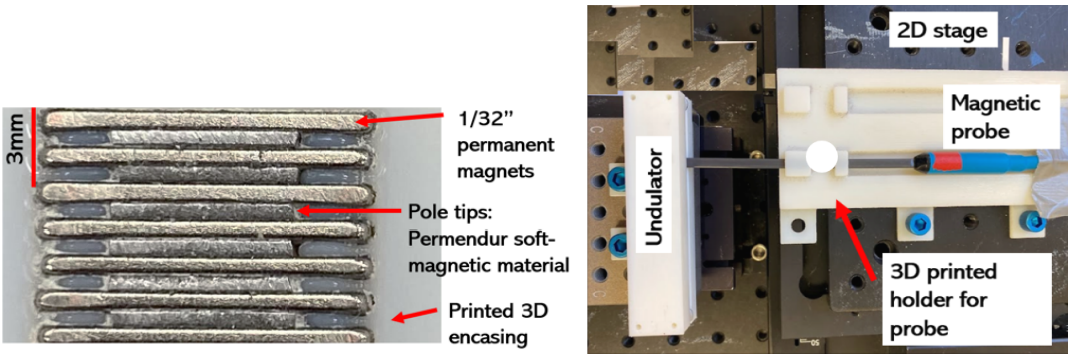

Figure 3.22: Experimental setup of 2.7 mm hybrid undulator

The longitudinal scans are shown in Fig. 3.23. The Hall probe is approximately 1.5 mm thick, which limited the minimum gap size. We see, however, that the scans performed at gap sizes above the probe thickness agree well with RADIA simulations. This gives confidence that if the gap were to be reduced $\lambda_u/4 \approx 0.7$ mm, the magnetic field in the gap would reach around 1.2 T, for which the K value is 0.3.

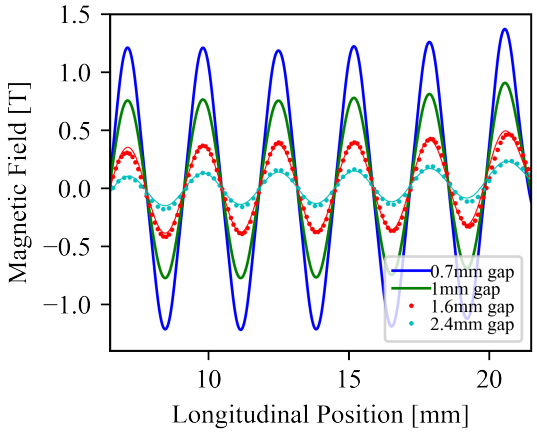

Figure 3.23: Left: picture of several periods of a hybrid undulator, labelled with the various features. Right: experimental setup of 2.7 mm hybrid undulator with a 1.6 mm gap.

Correcting field errors is commonplace and necessary for undulators with cm-scale periods. The ability to correct field errors may be even more crucial with short period undulators because a) the effects manufacturing errors and material inhomogeneities become more pronounced and b) it is simply more difficult to make adjustments on millimeter scales versus

centimeter scales [90, 95]. Indeed, Papadichev and Rybalchenko [96] demonstrated a 2.7 mm hybrid undulator similar to that shown here (except our undulator is stronger due to permendur plates - our undulator would produce 0.75 T at 1 mm gap, whereas the undulator of Papadichev and Rybalchenko only produces 0.5 T at the same gap). In the referenced work they demonstrated a form of shimming, which is simply to shunt flux from adjacent poles. This technique is not very flexible, however. They also suggested moving individual pole tips as a solution to correct trajectory errors, but such a technique would also be very difficult to implement.

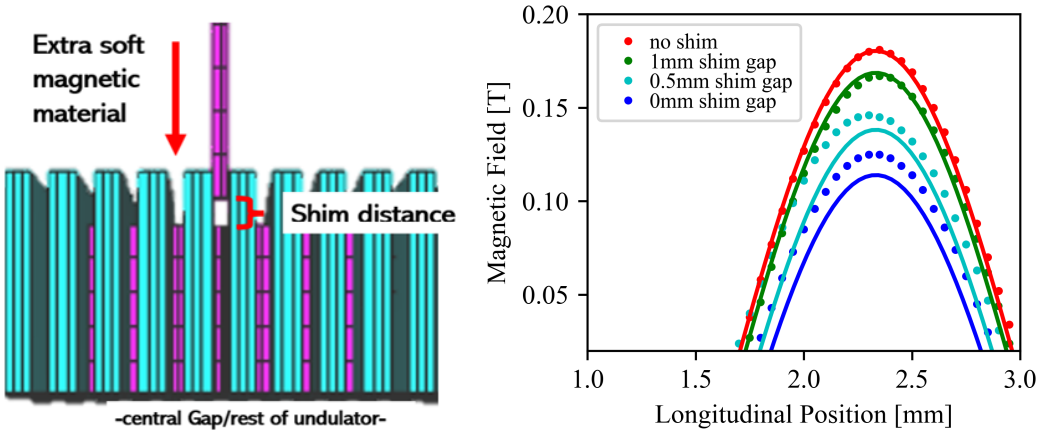

Figure 3.24: Left: schematic of top undulator half with a single shimmed pole piece. Right: The experimentally measured shimming effect, compared with RADIA simulations.

The shimming method presented here is different. The pole tips of most hybrid undulators are smaller in size than the permanent magnets around them. We show that inserting a soft magnet in the space behind the pole tip, between the PMs as shown in Fig. 3.24a is a tunable shimming method. The shimming gap, or the distance between the shimming piece and the pole tip itself, can be adjusted to proportionally change the field in the undulator gap. The results of this experiment are shown in Fig. 3.24b. With no shim the field underneath the corresponding pole tip is at the maximum, and the field decreases as the as the shimming gap decreases. The magnetic field was reduced from 0% to 31%. For large shimming gaps the shimming effect matched the RADIA simulations well; the deviation of small shimming

gap behavior from simulation is likely due to imprecise measurement of the actual shimming gap. Normally, such shimming would also affect neighboring poles, but our data was too noisy to see a clear trend. If shims were used on neighboring pole tips one would expect coupling between the spacers themselves; this would certainly modify the shimming effect across the undulator, but not the overall efficacy of the technique.

3.7 Conclusion

This section showed modeling and experimental results for an electromagnet undulator with a 1.2 mm period. Due to fabrication and manufacturing errors the point-for-point agreement was poor, but the overall behavior, including wiggle amplitude, was close to expected. Future work would be to improve the fabrication, especially the laser-drilling of the yoke slots, using coils on both sides of the wafer, and mounting on a thermally conductive substrate to use higher currents. It would also be profitable to explore the use of pulsed power. Without pulsed power the maximum possible undulator parameter value is around 0.02; with pulsed power, it may be possible to extend this by a factor of ten.

It was also shown that permanent magnet undulators can, even at the single-mm period level, achieve significant undulator parameter values. The demonstrated 2.7 mm period undulator with fields projected to exceed 1 T at the optimum 0.7 mm gap, possesses a K value around 0.3. Additionally, tunable field tuning that is suitable for large-scale undulator integration was demonstrated experimentally. Future work could include designing the end periods for trajectory correction, fabrication with a metal mount (probably using precision wire electrical discharge machining), and more precise magnetic measurements.

CHAPTER 4

Brief exploration of alternate quadrupole configurations

In this section two different current-dominated quadrupole devices based on microengineering processes (related more to conventional fabrication than microfabrication) are presented. Both devices are treated theoretically, simulated, fabricated, and experimentally characterized.

4.1 Intraundulator focusing via current sheets

4.1.1 Background

X-ray free electron lasers (XFELs) require a well-focused electron beam throughout the undulator section. This is typically accomplished through "lumped" focusing that uses quadrupole magnets placed between undulator segments. There are times, however, when lumped focusing is not adequate and "distributed" focusing, where the beam is continually focused inside of the undulator without dependence on quadrupoles between undulator segments, must be used. Examples of situations that may require a distributed focusing scheme include long-wavelength FELs [97] and small gap undulators. Maintaining a small beam size inside a small gap with a high energy electron beam can be challenging - if the undulator has a small period, and therefore using lower energy electrons, the space charge induced divergence making beam size maintenance even more difficult, especially for a lumped element focusing system. In this case, distributed focusing can be useful solution to keep the beam

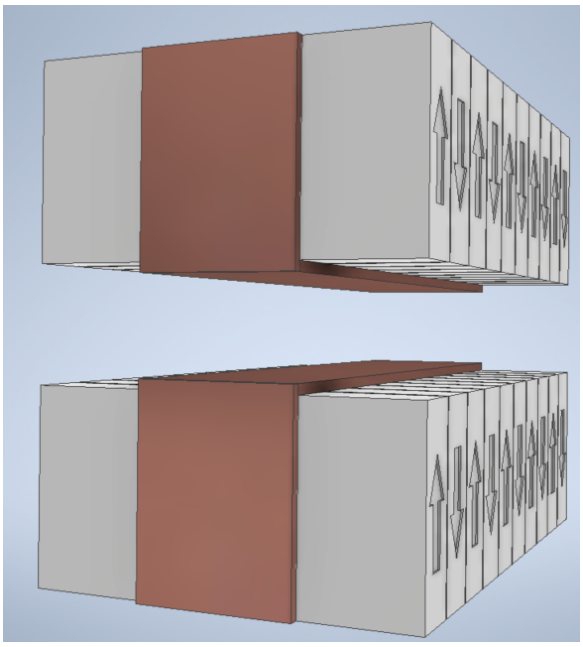

Figure 4.1: Concept of two current sheet quadrupole lining the inside of an undulator (magnetic field direction shown with arrows), including the current feed down the front face of the undulator. The two copper current sheets would have the same magnitude and direction of current for a quadrupole field configuration.

focused at all points in an undulator. Passing current through flat current sheets lining the inside of the undulator can provide such integrated, distributed focusing in a tunable fashion. I have termed this device the two current sheet quadrupole (TCSQ), as shown in Fig. 4.2. Lining in-vacuum short period undulators with conductive sheets is already standard practice to reduce beam impedance in the small gap [98, 99, 100], and so this work proposes to pass current through these pre-existing conducting sheets to produce a quadrupolar focusing field. For small gap devices (approximately 1 mm) we see a path towards gradients of around 50 T/m. Though this is a smaller gradient than other distributed focusing approaches, this new approach is very simple to fabricate and install in very small gap devices where other distributed focusing approaches would be very difficult to implement.

Many different distributed focusing designs have been proposed in the past. Undulators have built-in "natural" or "weak" focusing [101] (in both dimensions for helical undulators, but only the vertical direction for planar undulators), but this is usually not sufficient to

focus the beam to the required extent. One can enhance the sextupole focusing effect by shaping the undulator pole tips [102, 103, 104]. Quadrupole focusing has been demonstrated (often with gradients ≥ 50 T/m) by using:

- permanent magnet blocks placed in or near the undulator gap [88, 103, 105],
- longitudinally wedge-shaped permanent magnet blocks [106, 107],
- trapezoidal blocks [108],
- moveable undulator magnets [109],
- canted gap [110], or
- novel very high gradient (800 T/m) designs such as the twisted undulator [111].

Previous research suggested that sextupole focusing was superior to quadrupole focusing [101, 102], but other numerical results suggest that quadrupole focusing is more effective [112]. However, numerous experiments have successfully used both quadrupole and sextupole focusing elements.

4.1.2 The two current sheet quadrupole (TCSQ)

The proposed two current sheet quadrupole (TCSQ) can be simply modeled as two current sheets as seen in Fig. 4.2. This is identical to the yokeless MPQ discussed in Chapter 5. This device was briefly mentioned in Chapter 2 where we calculated:

- the gradient of a single current volume in Eq. 2.17
- the gradient at the very center of the two-plate device, which is the same as the TCSQ in Eq. 2.18
- the gradient at the center of a very long two-plate device (i.e., $L^2 \gg W^2 + (H+g)^2$, which is likely true for any envisaged usage) in Eq. 2.19

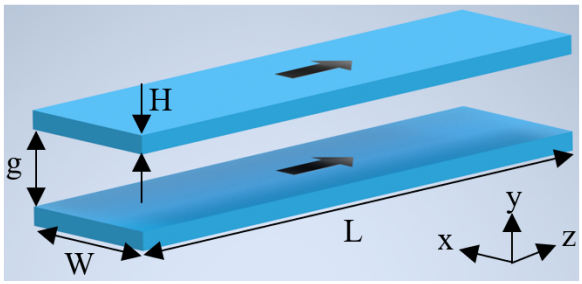

Figure 4.2: Diagram of the two current sheet quadrupole (TCSQ), with the geometry parameters labeled.

We will use the gradient at the center of the long TCSQ (Eq. 2.19), so we restate it here for convenience:

$$\frac{dB_y}{dx}_{center,max} = \frac{2\mu_0 J_0}{\pi}\left[\arctan\left(\frac{2H+g}{W}\right) - \arctan\left(\frac{g}{W}\right)\right] \tag{4.1}$$

We will see that it is useful to minimize Eq. 4.1 with respect to W to find a critical width at which the gradient is maximum, which is calculated to be

$$W_c = \sqrt{g(g+2H)} \tag{4.2}$$

We see that if the gap is much greater than the thickness of the conducting sheet the critical width is approximately equal to the gap. Calculating the critical width without the assumption of long length must be done numerically by minimizing Eq. 2.18 with respect to W.

4.1.3 Investigation of gradient

We can re-parameterize the TCSQ gradient (Eq. 4.1) in terms of two scaled variables, H/W and g/W; a contour plot of the resulting equation is found in Fig. 4.3. The current density for this plot was chosen to be $J = 1 \times 10^7\ \mathrm{A/m^2}$; the maximum gradient obtained at this current density is $B' = 4\pi = 12.57\ \mathrm{T/m}$. As the TCSQ gradient depends linearly on current

density this plot can be scaled for any current density. To use the plot to predict device performance, one would compute the scaled variables $H/W, g/W$, find the relevant contour on the plot, and multiply the contour value by the appropriate factor to scale the reference current density (1×10^7 A/m^2) to find the gradient of a "long" TCSQ.

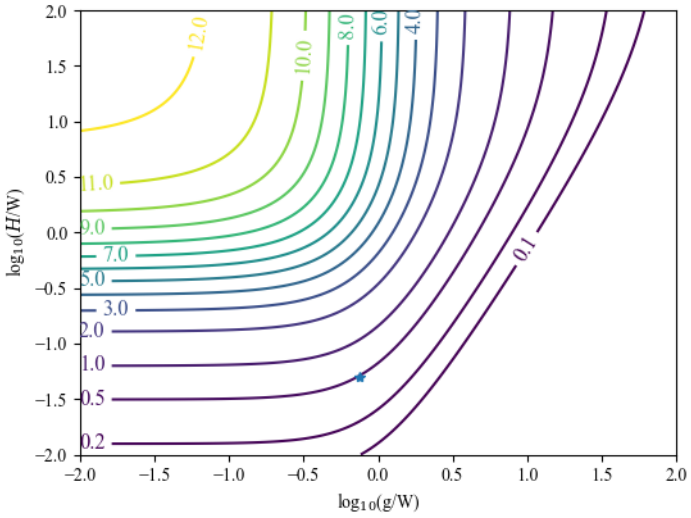

Figure 4.3: Normalized log-log plot of maximum center point gradient in two plate quadrupole with $J = 1 \times 10^7$ A/m^2. The star corresponds to a device with $g = 0.75$ mm, $W = 1$ mm, and $H = 50$ μm.

We can take the example of a 3 mm period undulator with a typical 0.25 λ_u (0.75 mm) gap. Copper sheets of 10s microns can easily be manufactured, so let us use $H = 50$ μm as the thickness and W=1 mm as the width. Naturally this narrows the usable gap by 100 μm to 0.65 mm, which is substantial in light of the already narrow gap, but this example is simply illustrative of the concept. This set of parameters is marked on Fig. 4.3 as a star and will achieve $\tilde{0}.5$ T/m field gradient. While this is a relatively low gradient, the current density was also relatively low. It may be possible to increase the current by a factor of 10 for room temperature copper without leading to much heating, and a factor of 100 for cryogenically cooled copper. Thus there exists a path for gradients exceeding 50 T/m using two current sheets in this type of configuration. This plot does not address homogeneity

of the magnetic field gradient, however, so this will be addressed further in the following section.

4.1.4 Gradient homogeneity

Gradient uniformity is important for beam focusing elements. The field quality of the TCSQ, like other quadrupole magnets, is highly dependent on geometry. As the TCSQ is described by only a few parameters (gap, current sheet height, width, and length), it is relatively straightforward to explore the parameter space. For this analysis the device has a gap of 3 mm, conductor thickness of 0.1 mm, and $J = 1 \times 10^7\,\mathrm{A/m^2}$ current density. As previously stated, this is a conservative current density.

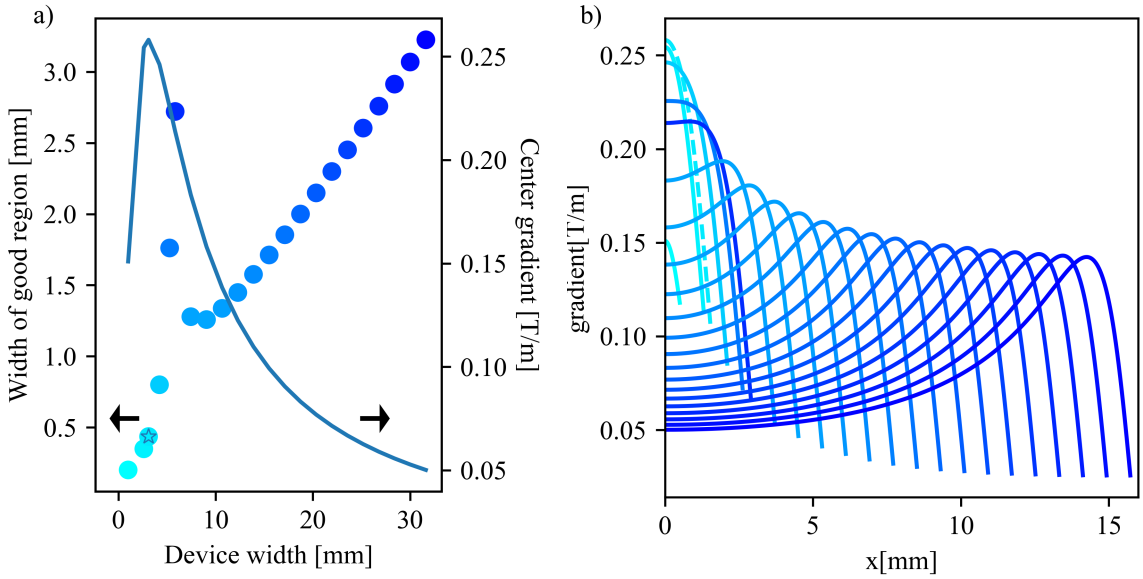

Figure 4.4: Dependence of the TCSQ gradient on width with $H = 0.1$ mm, gap = 3 mm, and $J = 1 \times 10^7\,\mathrm{A/m^2}$. a) 1% good field region width as a function of width on the left axis and the center gradient plotted on the right axis. b) transverse gradient profiles as a function of width, where only half the curve is shown because of symmetry across the y-axis. Note that the color of the points in part (a) corresponds to the same-colored curves in part (b).

Using Eq. 2.17 we calculated the 1% good field region and center gradient values for a wide range of conducting sheet widths. The 1% good field region (dots) is plotted on the left

y-axis in Fig. 4.4a and the gradient (line) is plotted on the right y-axis. There are several noteworthy characteristics of this plot. First, the gradient peaks at a critical width around 3 mm, which matches the expected value from Eq. 4.2 of $W_c = 3.1$ mm, then continuously declines after that. The starred point corresponds to the good field region size at the critical width in Fig. 4.4a. The width of the good field region, as a function of device width, also has a peak value. After this peak value, the size of the good field region drops rapidly but recovers at very large widths. The problem is at large widths the gradient is quite low. The color of the dots in Fig. 4.4a correspond to the full transverse gradient profile in Fig. 4.4b, where we can clearly see this evolution. Very dark blue dots/profiles signify a wide good field region, whereas a light blue denotes a narrow good field region.

We see, therefore, that there exists a region that possesses both a reasonably sized good field region and relatively high gradient. In my experience this width tends to be around $2W_c$ but the precise width needs to be found from simulation.

We observe a similar behavior with a variable gap and fixed width. In this example let $W = 4$ mm, $H = 0.1$ mm, and $J = 1 \times 10^7\,\mathrm{A/m^2}$). We plot the gradient profiles in 4.5a, where the dashed line corresponds to the largest good field region point in 4.5b. Again, the good field region width is maximized, along with the gradient, when the chosen width is about twice the gap.

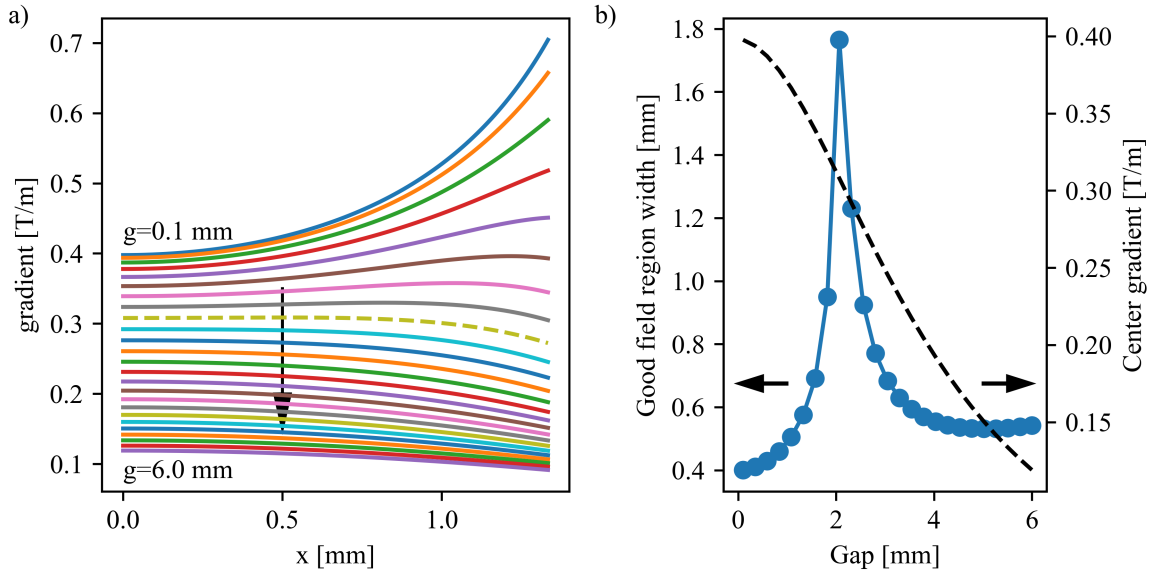

Figure 4.5: Dependence of the TCSQ gradient on the gap with $H = 0.1$ mm, $W = 4$ mm, and $J = 1 \times 10^7$ A/m^2. a) transverse gradient profiles as a function of width at different gaps. The largest gap (6 mm) has the lowest gradient, whereas the smallest gap (0.1 mm) has the largest gradient. The dashed curve possesses the largest 1% good field region. Only a limited extent in x is shown because the gradient near the edges of small-gap spikes significantly; for example, the gradient of the $g = 0.1$ mm device reaches 2.2 T/m at x=1.9 mm. The required axis rescaling obscures the clear trend shown here in the device center, which is of most interest. b) the points show the 1% good field region width as a function of gap (left axis) and the dashed black line shows the gradient as a function of width (right axis).

The behavior of the gradient as a function of conductor thickness behaves as expected. As the conductor thickness increases the gradient increases, but the good field region size does not change appreciably. These results are shown in Fig. 4.6.

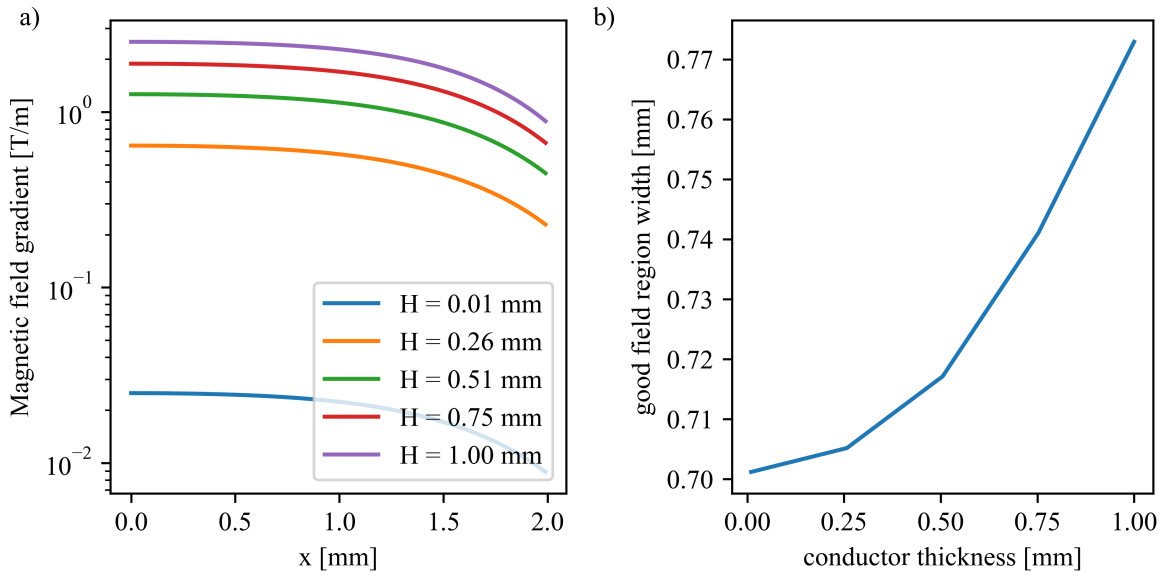

Figure 4.6: Dependence of the TCSQ gradient on the conductor height with a gap of $g = 3$ mm, width $W = 4$ mm, and $J = 1 \times 10^7$ A/m^2. a) transverse gradient profiles with different conductor thicknesses H. b) 1% good field region width as a function of conductor thickness.

Finally, the full multipole spectrum of this device was calculated as a function of width in Fig. 4.7. Both axes show the multipole amplitude; the quadrupole $n = 2$ multipole amplitude (dashed line) corresponds to the right y axis, whereas all higher order multipole amplitudes (solid lines) correspond to the left y axis. We see that all multipoles eventually decay with increasing device width, but that higher order multipoles decay more rapidly than lower order multipoles. We see that the higher order multipoles (solid lines, left axis) become very small when $W \approx 2W_c \approx 2g$, but the $n = 2$ quadrupole moment (dashed line, right axis) remains relatively large.

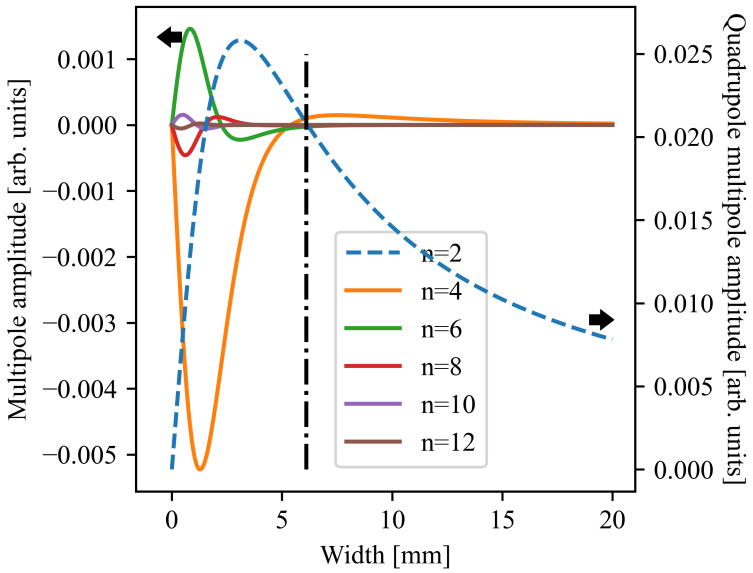

Figure 4.7: Harmonic analysis of TCSQ as a function of width for a device with $g = 3$ mm, $H = 0.1$ mm, and $J = 1 \times 10^7\,\mathrm{A/m^2}$. The quadrupole moment corresponds to the right axis; all other harmonics correspond to the left axis. The dot-dashed line corresponds to the width of the device with the largest good field region as calculated from the transverse gradient profiles.

4.1.5 Experimental demonstration

A series of TCSQ devices with different widths were constructed using 3D printed mounts and adhesive copper tape (50 μm thick) to validate these simulations. The length (3.5 inches, $\approx$ 89 mm) was chosen to be much larger than the width or gap. The mounts had printed alignment marks that helped precisely align the copper tape strips. The gap was set by precision aluminum spacers between the two halves of the mount. Fig. 4.8 shows the two separated halves of the mount with copper tape, and the fully assembled device in the bottom inset.

The magnetic field was measured by a custom three-axis Hall probe designed for low field measurements that was fixed to a 2D scanning stage, and the center gradient and good field region width were calculated. The measured magnetic fields were somewhat noisy (due to inherent magnetic sensor noise and the unshielded test setup) to complicate the calculations,

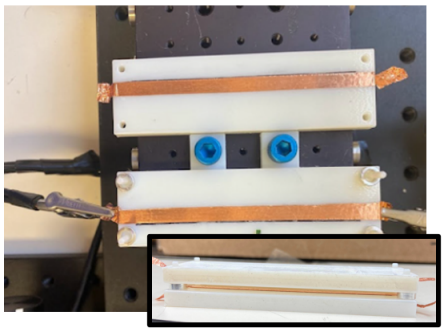

Figure 4.8: Picture of 3D printed mounts with copper tape installed. The insert shows the assembled device.

so the magnetic field data was smoothed during data post-processing.

The experimental results, compared with simulation, are shown in Fig. 4.9. The device parameters were copper sheet thickness of approximately 50 μm, a gap of approximately 2.5 mm, and a series of device widths from 1.25 to 8.25 mm. The current density was fixed at $J = 1.92 \times 10^7\,\mathrm{A/m^2}$, which was chosen to produce manageable heating in the largest devices. Fig. 4.9a shows simulations of the transverse gradient profiles over the width range, and Fig. 4.9b shows the experimentally measured transverse gradient profiles of the same widths. The comparison of these two data plots shows good qualitative agreement despite the presence of data artifacts (especially for smaller width devices) stemming from fabrication and alignment imperfections. Fig. 4.9c shows the 1% good field region width of the simulations in Fig. 4.9a (cyan-blue hue scale) and the measured data in Fig. 4.9b (yellow-red hue scale). Again, the lighter colors correspond to small good field region widths, and darker colors correspond to larger good field region widths. We see that the experimentally measured good field region width replicated the expected peak structure, showing an optimal good field region width around 5 mm, which is roughly twice the gap and critical width. This comparison is highly dependent on the quality of the magnetic field data, and thus on the sensor - the match between simulation and experiment would improve with a better magnetic field sensing setup. Lastly, we see in Fig. 4.9d that the center gradient as a function of width and note that it generally matches the simulated curve well, especially for wider devices for

which alignment errors are proportionally smaller.

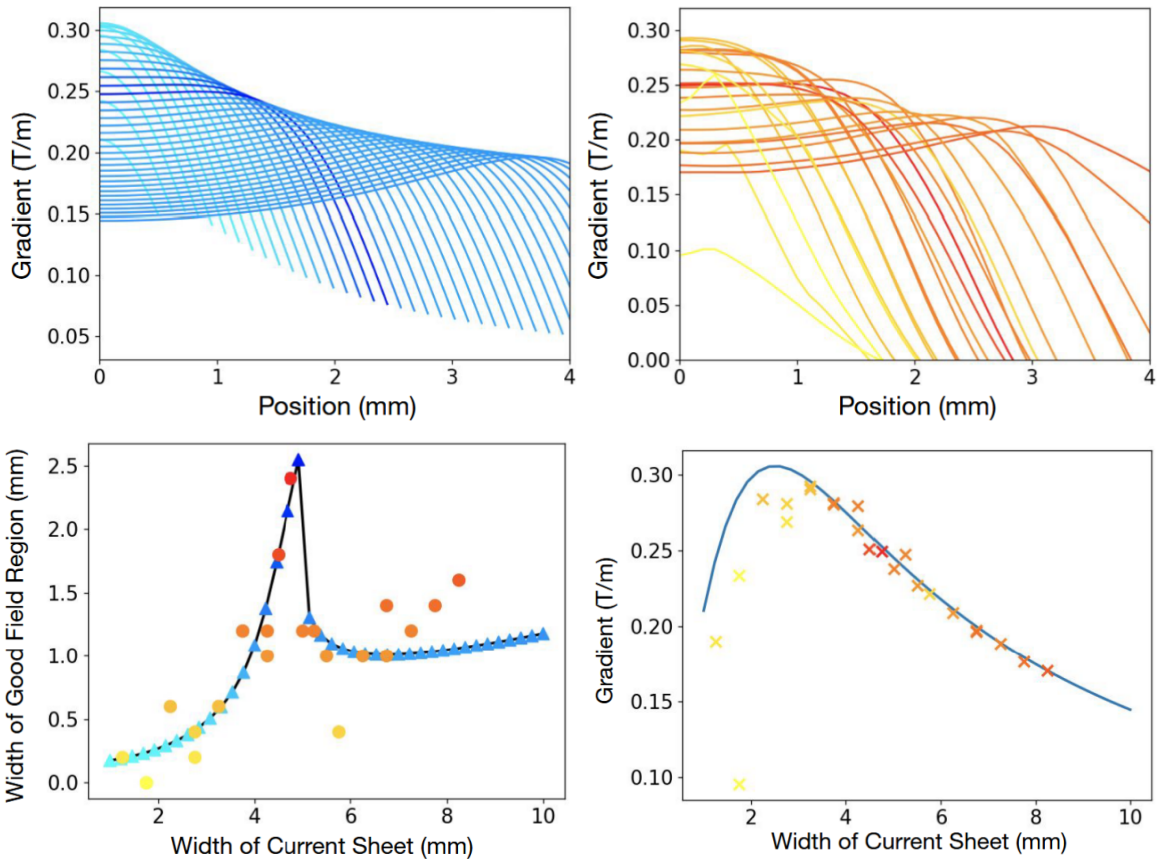

Figure 4.9: a) Simulated transverse gradient profiles, b) experimentally measured transverse gradient profiles, c) good field region width (simulated and measured), and d) gradient at the TCSQ center (simulated and measured). In all cases the TCSQs had a gap of 2.5 mm, current density of 1.92E7 A/m^2, copper thickness of approximately 50 μm, and the device widths were varied from 1.25 mm to 8.25 mm.

4.1.6 Benefits of cryogenic operation

This technology would likely work best with cryogenic undulators [113] because:

1. The cryogenic electrical resistivity of the most commonly used conductor, copper, is several orders of magnitude smaller than the electrical resistivity at room temperature, which substantially decreases the amount of power dissipated by the conductor.

2. The thermal conductivity also increases, though usually by less than an order of magnitude, within a wide cryogenic temperature range. This means that heat can flow freely to the thermal ground held at a low cryogenic temperature.

Not all properties become better at low temperatures; the specific heat generally decreases with temperature but only by roughly one order of magnitude. However, the combined improvements in electrical resistivity and thermal conductivity is larger than the decrease in specific heat.

The heating of the current sheets, and resultant demagnetization effects on the ferromagnetic elements of the undulator, must be taken into account in the design, as any heating will decrease the undulator magnetic field due to reversible (if the temperature does not get too high) magnetization loss. One may be tempted to consider superconducting current sheets to circumvent this heating issue. However, superconductors exclude magnetic fields, which would largely (and unacceptably) neutralize the dipole fields of the undulator.

4.1.7 Conclusion

We confirmed experimentally that there exists an optimum current sheet width that produces both a high gradient and large region of uniform gradient. This device could be useful in upcoming short period, small gap undulators as a distributed focusing element. The most likely application would be for cryogenically cooled undulators that can tolerate some heating from normal-conducting current sheets. With such modalities the current density could possibly reach $J = 1 \times 10^9\,\mathrm{A/m^2}$ and gradients larger than 50 T/m.

4.2 Monolithic quadrupole

4.2.1 Theory - conformal mapping derivation

As we saw in the last section, the field produced by two flat current sheets is impure and has higher order multipole content. In this section we will use conformal mapping to analytically predict a better current-dominated geometry to produce a quadrupole field. Conformal mapping is inherently two-dimensional, leaving the consideration of length or edge effects to other techniques. General solutions of various geometries using conformal mapping techniques are given by Beth in such references as [114, 115]. The notation and approach described here is more reminiscent of that shown by Halbach [116].

In this example we desire to find the optimal current sheet geometry. We first specify the field that we want on a line. We choose the line along x at $y = 0$ and specify the desired field to be $B_x = 0$, $B_y = B'x$, where B' is the field gradient. We then construct the analytical function $B^*(z)$ through analytic continuation:

$$B^*(z) = B_y - iB_x = B'z$$

where $i = \sqrt{-1}$ and $z = x+iy$. By definition, the complex potential $F = A+iV$, where A and V are the magnetic vector and scalar potentials, respectively. As the current sheets are considered in this model to be infinitely long in the z direction, we need only consider the z component, A_z, in the x, y plane. By derivation, it can be shown that $F'(z) = \frac{dF}{dz} = -iB^*(z)$. Through direction integration we find F to be

$$F = -\frac{1}{2}B'z^2 = -\frac{1}{2}B'(x^2 - y^2) - iB'xy = A + iV$$

where the last equation comes from the definition of F. In general, the shape of soft iron pole tips corresponds to a constant scalar potential; a corresponding rule is that the shape

of a current sheet should correspond to a constant vector potential, which we will call A_0. Therefore,

$$A = \mathrm{Re}\{F\} = -\frac{1}{2}B'(x^2 - y^2) = A_0$$

Solving for y in terms of A_0 gives

$$y = \sqrt{\frac{2A_0}{B'} - x^2} \tag{4.3}$$

The first term with A_0 cannot be smaller than the largest value of x^2, which is $x^2 = (W/2)^2$, which places a limit on the values of A_0. The actual value of A_0 is not of concern. The maximum value of x is half the device width W, which gives

$$A_0 \geq \frac{B'}{2}\frac{W^2}{4}$$

Substituting this into Eq. 4.3 and taking the equality gives

$$y = \sqrt{\frac{W^2}{4} - x^2} \tag{4.4}$$

which is simply the equation for a circle of diameter W.

4.2.2 Theory - magnetostatic derivations

Equation 4.4 specifies the bore region inside a conductor with otherwise constant current density should be circular to generate a quadrupole field. Since the outer part is not specified, we will take the outer geometry to be a rectangle. We do this for two reasons: 1) ease of fabrication and 2) simplicity of calculation. We will revisit this choice of geometry later. The device can be visualized as shown in Fig. 4.10a, and the 2D computation of the magnetic field done in COMSOL Multiphysics is shown in Fig. 4.10b for a device of width (W) of 4

mm, height (H) of 2 mm, and a bore diameter (or gap, g) of 1 mm. The gradient for this device is 257 T/m with a current density of $J = 1 \times 10^9$ A/m^2.

The first group to consider this type of device was Sarma *et al.*, whose contributions will be discussed in context in a later section. They did not show any experimental validation of their designs, but experimental validation will be shown here.

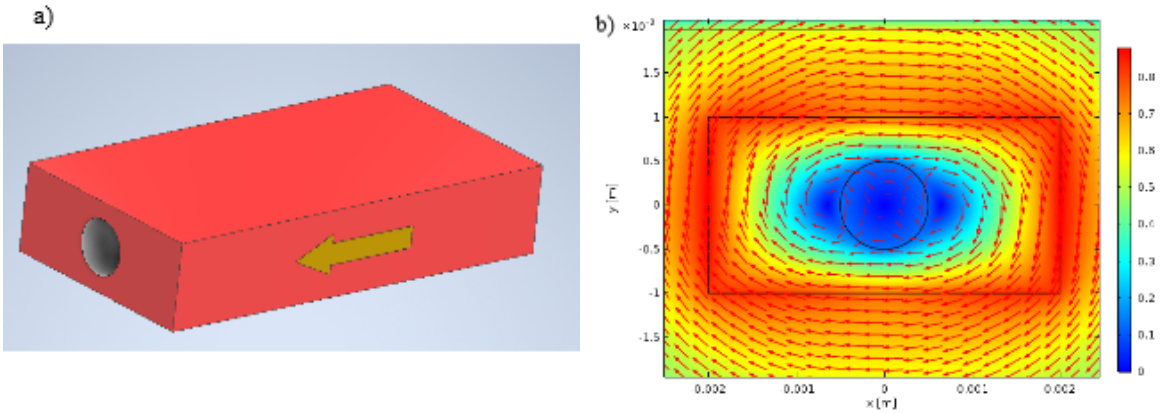

Figure 4.10: a) prototypical device in three dimensions, with a current flowing in the direction of the arrow. b) 2D magnetic field amplitude of device, with arrows showing the direction of the magnetic field. We see the characteristic form of a quadrupole field in the bore region. The scale bar unit is Tesla.

The conformal mapping approach does not give us a way to calculate the gradient of the device, so we turn to the direct integration of Maxwell's equations. Magnetic field gradients superimpose linearly. This geometry can be equivalently represented by the superposition of a rectangular (in the cross-section) block and a cylindrical current volume, with opposing currents.

We previously derived the gradient of a volume current in Chapter 2 to be Eq. 2.17. By allowing $L \to \infty$ and evaluating at the origin yields the gradient in the center of the current block:

$$\frac{dB_x}{dy}_{CB} = -\frac{8\mu_0 J_0}{4\pi}\,\mathrm{atan}\left(\frac{W}{H}\right) \tag{4.5a}$$

$$\frac{dB_y}{dx}_{CB} = \frac{8\mu_0 J_0}{4\pi}\,\mathrm{atan}\left(\frac{H}{W}\right) \tag{4.5b}$$

The magnetic field inside a solid cylinder with uniform current density in the $+z$ direction is easily found using Ampere's law to be

$$B_x(x,y) = -\frac{\mu_0 J}{2} y$$
$$B_y(x,y) = \frac{\mu_0 J}{2} x$$

and so the gradients inside the cylinders of current are calculated to be

$$\frac{dB_x}{dy}_{C} = -\frac{\mu_0 J}{2} \tag{4.6a}$$

$$\frac{dB_y}{dx}_{C} = \frac{\mu_0 J}{2} \tag{4.6b}$$

Therefore, to find the gradient at the center of a rectangular copper block with a circular bore region, we can simply superimpose these two gradient results, i.e., Eqs. 4.5 and 4.6 with the currents going in opposite directions. Therefore, we obtain

$$\frac{dB_x}{dy} = \frac{2\mu_0 J}{\pi}\left(\frac{\pi}{4} - \arctan\left(\frac{W}{H}\right)\right)$$
$$\frac{dB_y}{dx} = \frac{2\mu_0 J}{\pi}\left(\arctan\left(\frac{H}{W}\right) - \frac{\pi}{4}\right)$$

From the trigonometric identity $\arctan(1/x) = \pi/2 - \arctan(x)$ we see that these two expressions are equivalent. Therefore, the gradient is analytically calculated via

$$B' = \frac{dB_y}{dx} = \frac{dB_x}{dy} = \frac{2\mu_0 J}{\pi}\left(\arctan\left(\frac{H}{W}\right) - \frac{\pi}{4}\right) \tag{4.7}$$

We plot this equation in Fig. 4.11 over a variety of H/W for a current density of $J = 1 \times 10^7\,\mathrm{A/m^2}$. As this is an iron-free magnetostatic device, one can simply scale the gradient for a given H/W for the desired current density.

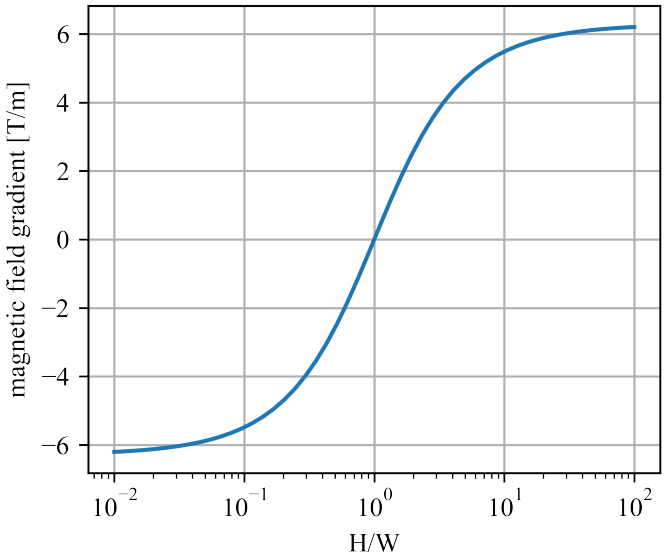

Figure 4.11: Gradient of device as a function of H/W at a current density of $J = 1 \times 10^7\,\mathrm{A/m^2}$.

Equation 4.7 was verified with a wide variety of geometries in COMSOL. We note a few significant features of this device as a result of Eq. 4.7.

1. For $H/W = 1$, the magnetic field gradient in the center is zero. Higher order fields may still be present, however.

2. For $H > W$, the gradient is positive (for a current directed in $+z$)

3. For $H < W$, the gradient is negative (again, for a current directed in $+z$)

4. The gradient is explicitly independent of bore size. Notably cos 2θ magnets also share this characteristic. Both magnet types are *implicitly* dependent on bore size, however; bigger bores require larger amounts of current to reach the same gradient.

5. The maximum gradient (i.e., for $H \gg W$) is $B'_{max} = \mu_0 J/2$. From Fig. 4.11, one can achieve 50% of the maximum gradient with $H/W \approx 2.4$ and 90% with $H/W \approx 12.7$.

4.2.3 Finite Element Simulations

While the device will have a strong quadrupole field by design, higher order multipole field components may also be present. A COMSOL study of the multipole fields of this device is presented in Fig. 4.12. These simulations were performed in two dimensions so all units should be considered arbitrary. Additionally, all skew moments are zero and so are not plotted.

As a first simulation, the height and width of the device were fixed and the bore diameter changed from 1 mm to 3 mm, shown in Fig. 4.12a. As predicted, there is no change whatsoever due to different bore sizes, besides the required current.

The results of fixing the bore size at 1 mm and changing the ratio H/W are shown in Fig. 4.12b. The quadrupole moment increases with H/W, and that the gradient with $H/W = 2$ is equal but opposite in sign as when $H/W = 0.5$. The octupole moment ($n = 4$) behavior requires more explanation. We see that for $H/W = 1, 2, 3, 4$, the relative strength of the moment decreases with larger H/W value. We see that the octopole moment for $H/W = 0.5$ is much larger than that of $H/W = 2$, despite the quadrupole moment being the same. This phenomenon arises because the $H/W = 0.5$ device is much smaller, physically, than the $H/W = 2$ device, which can be seen by the large difference in the $H * W$ product of these two devices. We investigate this phenomenon in 4.12c, where the ratio H/W is constant but the size of the device, given by $H * W$, is changed linearly. This study confirms that small $H * W$ lead to higher order multipoles with relatively larger amplitudes.

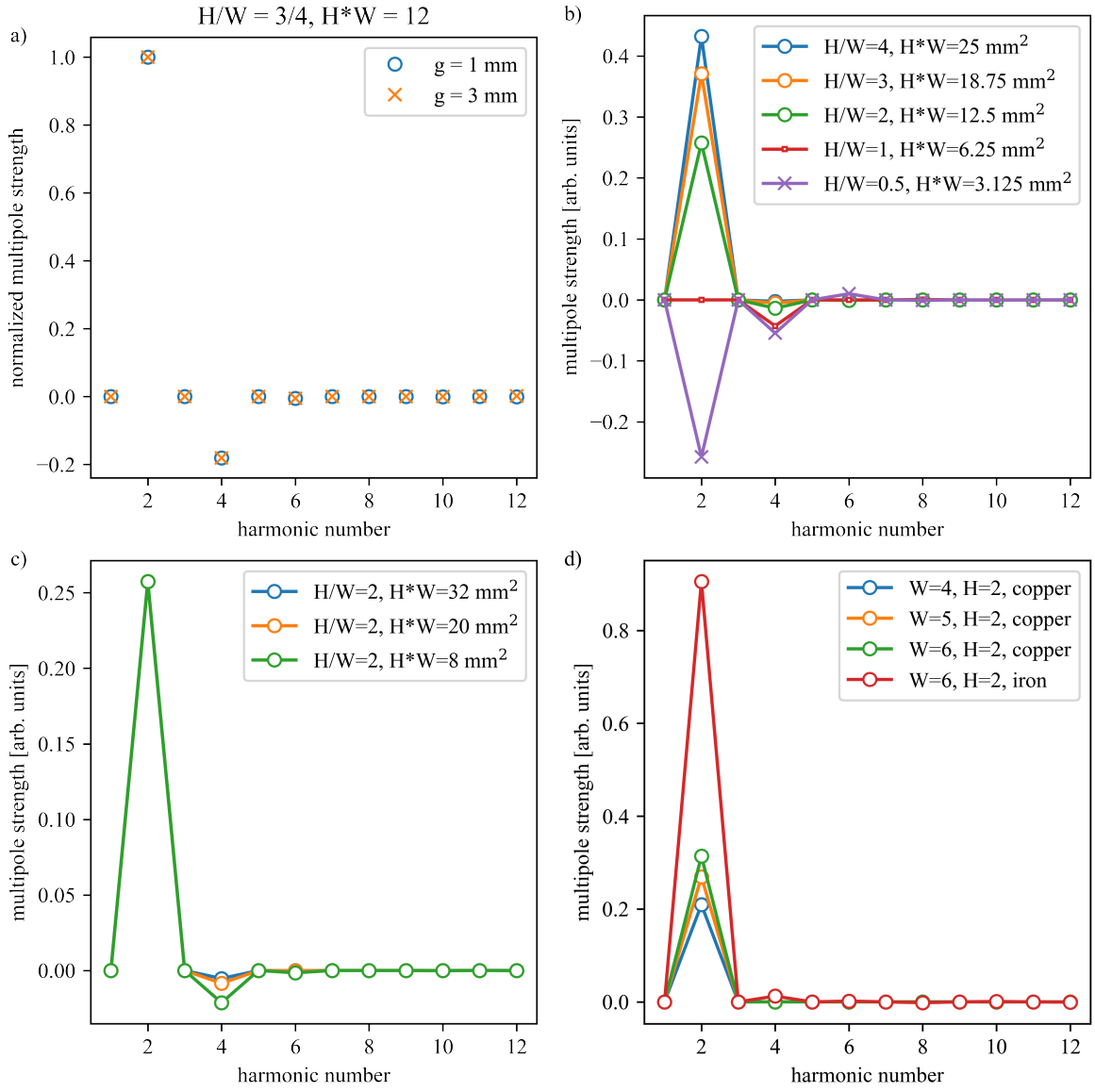

Figure 4.12: Geometry effects on field components, calculated in 2D in COMSOL Multiphysics at a reference radius of 98% of the bore radius in all cases. a) Effect of bore size (H=3 mm, W=4 mm, bore=1, 3 mm). b) Effect of H/W ratio. c) Effect of $H*W$ product. d) Harmonics of elliptical copper design and elliptical iron (constant $\mu_r = 4000$) design.

We then simulated a conductor with an elliptical cross-section and circular bore. We show the results for several major axis total widths in Fig. 4.12d. As expected, larger W/H leads to strong quadrupole moments. For the devices made of copper, the higher order harmonics are vanishingly small, which means that the quadrupole field is intrinsically very pure. This result was previously shown by Sarma *et al.* previously [117]. For the largest device we changed the device material from copper to iron with a relative permeability of $\mu_r = 4000$, which boosts the quadrupole field by roughly a factor of 3. In this case higher order harmonics do exist, but still at low levels. It seems that using iron as the device material, which conductivity is roughly 5 times lower than copper, would only be useful in a setting where the amount of current is limited by the power supply. The field is also not as pure as the copper conductor device, though the design could likely be optimized further. Additionally the effects of saturation were not taken into account; simulations attempting to quantify this did not converge sufficiently well to have confidence in the field data, but one could expect saturation to play a big role in field quality because it significantly changes the field distribution in the conducting material, which does not happen if the conductor is non-magnetic.

A preliminary investigation of the effect of bore misalignment on the field quality is shown in Fig. 4.13; the normal components are in part (a) and the skew components are in part (b). The device had an elliptical cross-section of major axis length $W = 12$mm and minor axis length $W = 6$ mm. The 2 mm radius bore was then offset by a distance dx, dy in the x,y directions respectively, by 0.25, 0.5, 0.75, and 1 mm steps. The corresponding effect on the harmonic fields, however, is not proportional to the displacement magnitude but rather the ratios dx/W and dy/H as shown in the legends. This device is wider than it is tall, and we see that for horizontal bore displacements, i.e., $dx \neq 0$, a normal (vertical) dipole moment is obtained, the strength of which is proportional to the displacement size. Indeed, it can be shown that the dipole field is given by $B_x \approx B'dy$ or $B_y \approx B'dx$ for the skew and normal components, respectively. We see the same behavior for vertical displacement,

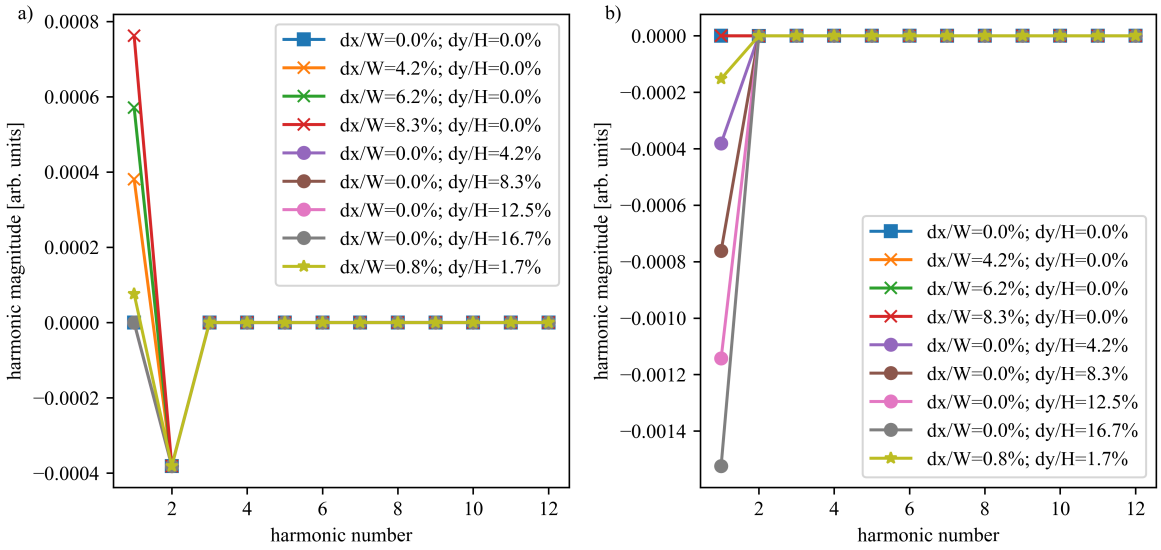

Figure 4.13: Effect of bore displacement in x (dx) and y (dy) from center of elliptical cross-section with major and minor diameters of H and W in the y and x directions respectively. The square markers show the zero displacement case, the "x", dot markers show the case of displacement in the x, y directions respectively, and the star marker shows the effect of simultaneous displacement in x and y. a) normal field components, which shows that only displacements in x, not y induce a non-zero normal dipole moment proportional to the size of the displacement, and b) skew field components, which shows that only displacements in y, not x, induce a skew dipole moment. The simulation with displacements in both directions also shows both a normal and skew dipole moment. Therefore, bore displacements only induce dipole moments, not higher order multipoles.

except that a skew dipole field (horizontal) is generated. We can also see that for the case of $dx/W = dy/H$ (for example, the orange x in (a) and purple dot in (b) for $dx/W = dy/H = 4.2E-2$), the normal dipole moment is the same magnitude as the skew dipole moment. As a last example to show that these dipole moments can be superimposed, we simulated a device with a horizontal and vertical displacement of 0.1 mm, which is shown on the plots as a green star. We see that this configuration has both normal and skew dipole fields as well as a non-degraded normal quadrupole field. It is notable that 1) no other higher harmonics are generated and 2) that the quadrupole strength does not suffer as a result of bore displacement.

The first device that we investigated (with a rectangular cross-section) is practically

trivial to build and test, so we present experimental results in the next section using that device.

4.2.4 Experimental verification

The rectangular cross-section device was fabricated as a proof-of-concept. The dimensions of the copper block were 1/2" x 1/4" x 1", with a 4 mm bore size. Due to machining issues, the bore hole was misaligned by 0.5 mm and 0.15 mm in the vertical and horizontal directions, respectively. The current-carrying leads were chosen to be screws that are inserted a distance of only a few threads to maximize the current going in the z direction instead of the x and y directions. Some of the holes were not properly threaded, so the holes were filled with solder paste, the screw leads inserted, then the solder reflowed using a heat gun. The final device is shown in Fig. 4.14a, and the same device connected and ready to be scanned (using the same setup used elsewhere in this dissertation) is shown in Fig. 4.14b. Although the bore size is 4 mm, the magnetic field probe size constrains the transverse range to 1.75 mm. The current was constrained by the heating of the leads, not the device, to 20 A ($J = 3.3 \times 10^5\,\mathrm{A/m^2}$ in the device); the resistive losses of the device at this current are less than 1 W and so does not heat up appreciably.

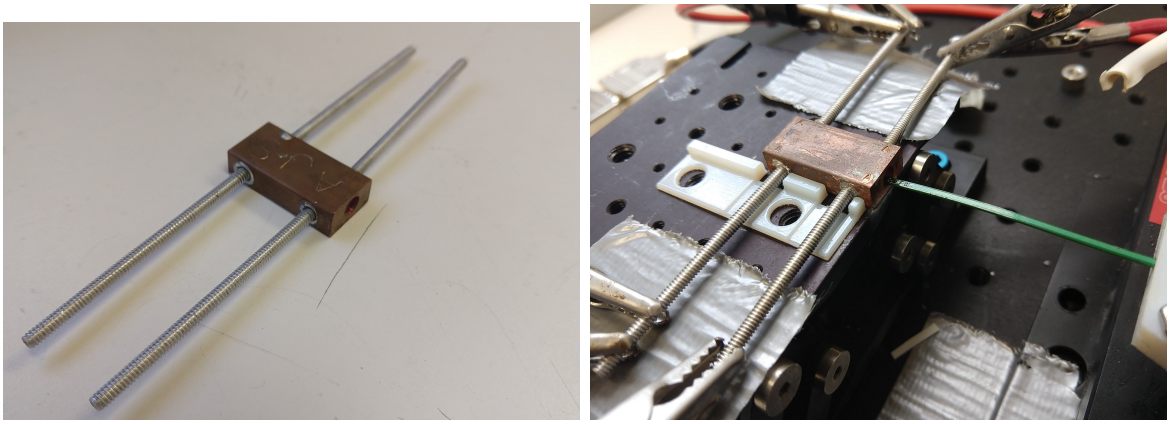

Figure 4.14: a) Monolithic quadrupole device, with attached screw leads. b) Mounted device for scanning.

Two-dimensional measurements of the magnetic field (all three components) were conducted in the xz plane, and the results are shown in Fig. 4.15. Fig. 4.15a shows the device coordinates. The orange plane shows the plane on which data was measured. It also shows the device extents using black lines and the approximate locations of the screw leads using red lines. These black and red lines are used in the data graphs that follow. Figs. 4.15b-d show the B_x, B_y, B_z components of the magnetic field respectively. We can see in Fig. 4.15b that the horizontal dipole component, B_x, is constant across the bore of the device (i.e., the x direction). In Fig. 4.15c we see a substantial variation of B_y with respect to x, which is the gradient we simulated. In Fig. 4.15d we see the measured B_z fields. We note that in the ideal case, where all current is directed in the z direction, there would be no component of B_z. However, the curved nature of the current in the leads causes current flow in the x and y direction nearby, leading to non-zero B_z magnetic field component in their vicinity. In all data sets we see good agreement between locations of field roll-off and the locations of the leads and device extents.

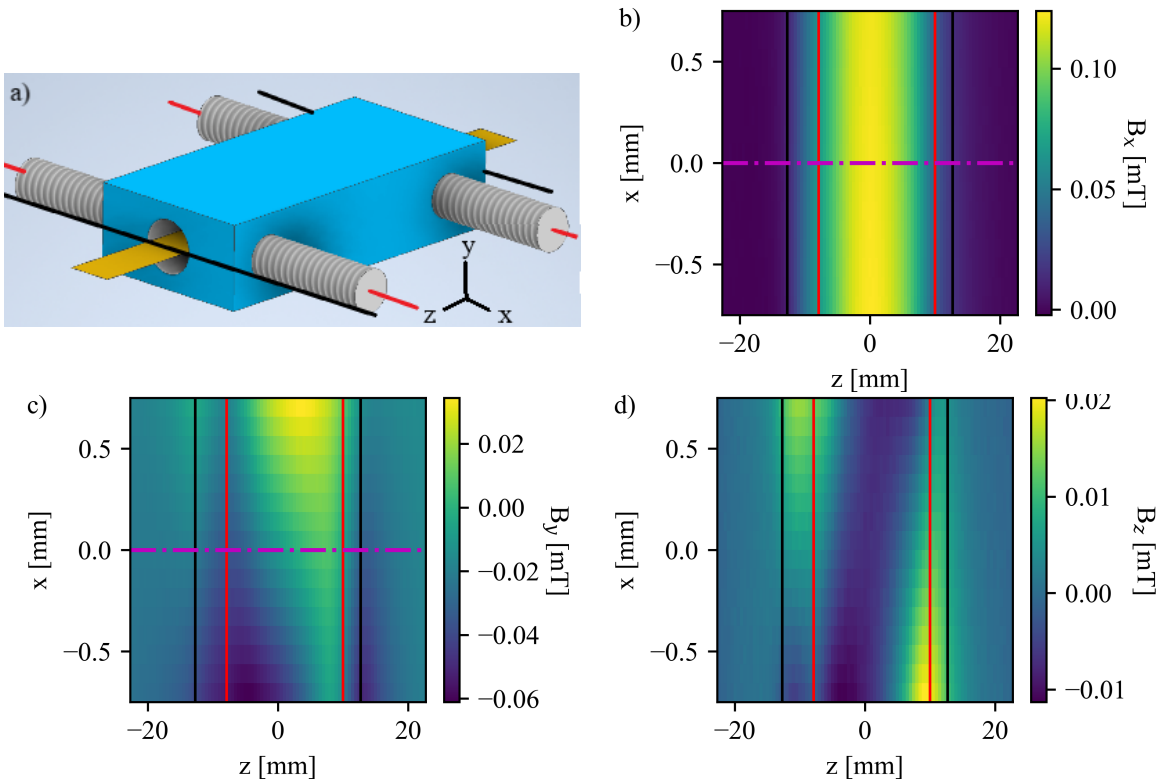

Figure 4.15: a) Model of device, with the specified coordinate system. The plane on which the data were measured is denoted by orange. The black and red lines denote the device edges and locations of screw leads, respectively. The other figures are the measured b) B_x, c) B_y, and d) B_z components of the magnetic field in mT. One-dimensional lineouts along the magenta lines in parts b,c are shown in Fig. 4.17b.

The main figure of merit that is most important for this work is the gradient, $\frac{dB_y}{dx}$, which is shown in Fig. 4.16. We see some of the features already discussed, which is good uniformity across the bore and expected field roll off near the leads. The noise in the graph comes from the low magnetic fields, in addition to stage movement uncertainties (our stage is not encoded).

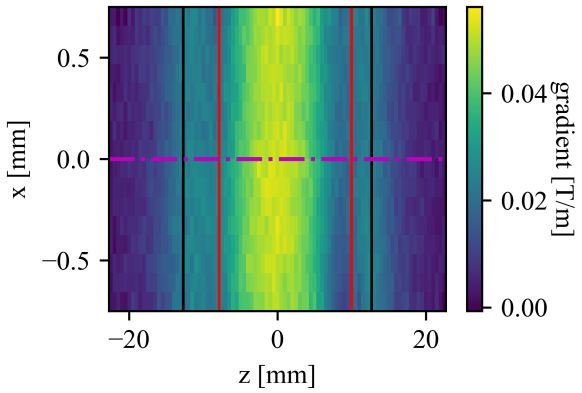

Figure 4.16: Gradient ($\frac{dB_y}{dx}$) of the device in units of T/m. A one-dimensional lineout along the magenta dashed line is shown in Fig. 4.17a

One-dimensional lineouts along the magenta lines from Fig. 4.15 and Fig. 4.16 are shown in Fig. 4.17. The experimentally measured data is plotted with simulated data from a RADIA. The RADIA model is substantially similar to the actual device in that the dimensions of the block, bore, and bore offset are the same. The main difference is that all the current is directed in the z direction since RADIA is not capable of modeling the screw leads correctly. While this is a significant difference, the overall behavior will not be drastically affected. First, we compare the variation of the experimentally measured transverse gradient along the device axis with the RADIA simulation. We see fairly substantial deviation. From Eq. 4.7 we expect a gradient of 0.076 T/m, which is between the maximum simulated and experimental measurement values of 0.093 T/m and 0.053 T/m respectively. The RADIA model does not match this value because of length effects; if the RADIA model is made very long the simulated gradient matches the analytical model.

As the bore is transversely offset, we also expect dipole components in both transverse directions, which are plotted alongside RADIA simulation predictions in Fig. 4.17b. We see relatively good agreement with the horizontal B_x component. This component arises from the large vertical bore displacement. The smaller horizontal displacement leads to a non-zero B_y offset, which is also shown. The general sign and magnitude of the measured data do match RADIA simulations, despite a lack of point-to-point agreement.

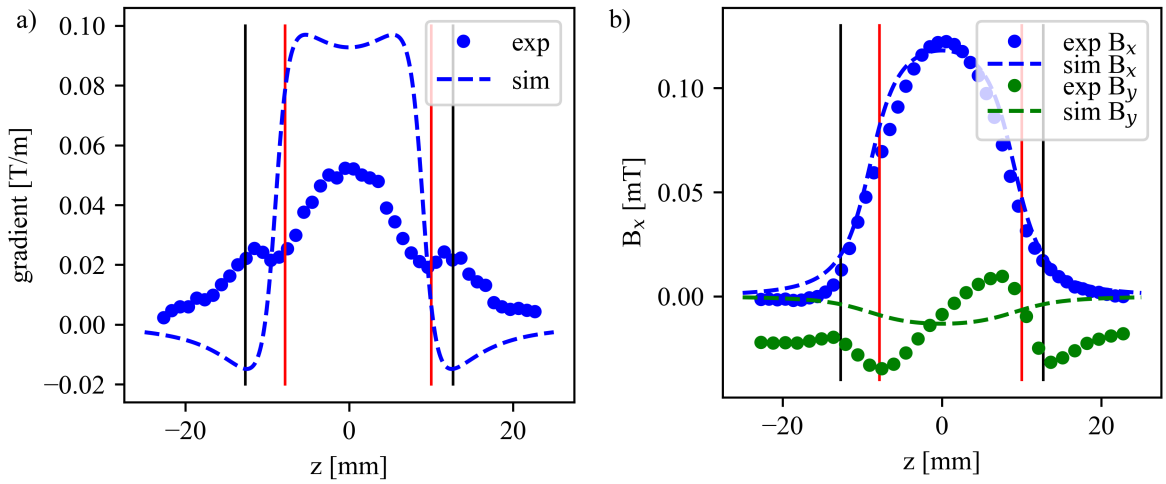

Figure 4.17: a) Experimentally measured and simulated (via RADIA) gradient of the monolithic quadrupole. The black vertical lines show the edges of the device, and the red vertical lines show the approximate locations of the electrical leads. b) The measured and simulated (via RADIA) transverse dipole fields of the monolithic quadrupole.

4.2.5 Further considerations

Elliptical conductors, with a circular cross-section, create pure quadrupole fields, but did not prove this assertion. I discovered after performing this work this type of device was first proposed by Sharma *et al.* in a series of papers. Their work was based on direct integration of the Biot-Savart law and numerical geometry optimization, not conformal mapping. They found the general gradient due to two superimposed ellipses, with opposite current directions of the same magnitude, to be

$$G = \mu_0 J \frac{ad - bc}{(a+b)(c+d)} \tag{4.8}$$

where a and d are the major axis lengths of the two ellipses, with b and c being their respective minor axis lengths. It is interesting to note that unlike the formula for the rectangular cross-section, which depended only on H/W, that this formula depends on all semi-axes of both ellipses. However, they also showed that the magnetic field inside this conductor,

and an entire class of related configurations, is a pure quadrupole field. They proposed to approximate the difficult-to-fabricate elliptical geometries with easy-to-fabricate rectangular coils using numerical optimization. Initially they did this analysis for $\cos(\theta)$ dipoles [118], but extended their work to quadrupoles [117], sextupoles [119], and combined function magnets (such as the device experimentally demonstrated here, which has superimposed dipole and quadrupole fields) [120].

As all current-dominated devices, this device requires high currents to achieve useful magnetic field gradients. For example, the prototypical device first presented with a gradient of 257 T/m (W=4 mm, H = 2 mm, g = 1 mm, $J = 1 \times 10^9$ A/m^2) requires a current of 7214 A. The resistive power dissipation per length is $P/\ell = \rho A J^2$, where P is the total power loss, ℓ is the length, A is the cross-sectional area of the conductor, J is the current density, and ρ is the conductor resistivity. At room temperature, a copper device has a resistivity of approximately $17 \times 10^{-9}\,\Omega$m and a power loss per length of 122 kW/m, which is very large. The resistive power loss can be reduced by operating normal conducting copper devices cryogenically, which can reduce the resistivity by several orders of magnitude, but using superconductors is the most promising technological platform for this type of device. Indeed, this was the conclusion of Sarma *et al.* [120]:

> It should be mentioned that it is not hard and fast that the coil should be superconducting only, to generate the required combined type fields. Room temperature coils will also generate the same type of field. However, the field generated by room temperature coils is too feeble to be of much use for accelerator applications. So we have emphasized the use of these coils in superconducting magnets.

It is clear that a superconducting magnet is the only viable option for a large bore magnet. Depending on the required gradient, it *might* be possible to use a normal conducting copper material for a small bore device due to improved thermal characteristics.

One interesting extension of this work is to realize that a single conductor block could be machined to be a monolithic magnet system with multiple magnets in series. For example, Fig. 4.18 shows a possible monolithic design for a quadrupole triplet. The red (blue) segments have negative (positive) field gradients for the current direction specified by the yellow arrow. Additionally, the length of the middle quadrupole is approximately twice that of the outer quadrupoles, which yields a total focusing configuration. The insets show the cutaway view of these devices. Consideration should be given to the nature of the transition between quadrupole segments. Two possibilities are shown in Fig. 4.18. In Fig. 4.18a there is a "linear" transition between quadrupole segments. At the middle of this transition the cross-section is a circle, which has zero magnetic field, and so there are no edge effects in transitioning between different "magnets" in the monolithic system. In addition, higher order multipoles are reduced during the transition because $H * W$ is relatively larger during the transition than in the main focusing sections. If higher order multipoles were desired, one could rotate the cross-section, keeping the area constant, as shown in Fig. 4.18b. The fabrication of this design would also be much more difficult, so there are not any foreseeable uses for this type of system.

One of the main sources of multipole components in accelerator magnets is due to the coils in the entrance and exit regions of the magnet. The monolithic quadrupole design shown in Fig. 4.19 avoids this problem. The current is fed into the red regions around the periphery of the yellow flange region. The flange would be designed sufficiently large to allow the current density to be uniform before entering the monolithic quadrupole. The symmetry of the current in the flange results in zero magnetic field at the magnet entrance, and so this configuration could result in very low higher order multipole content.

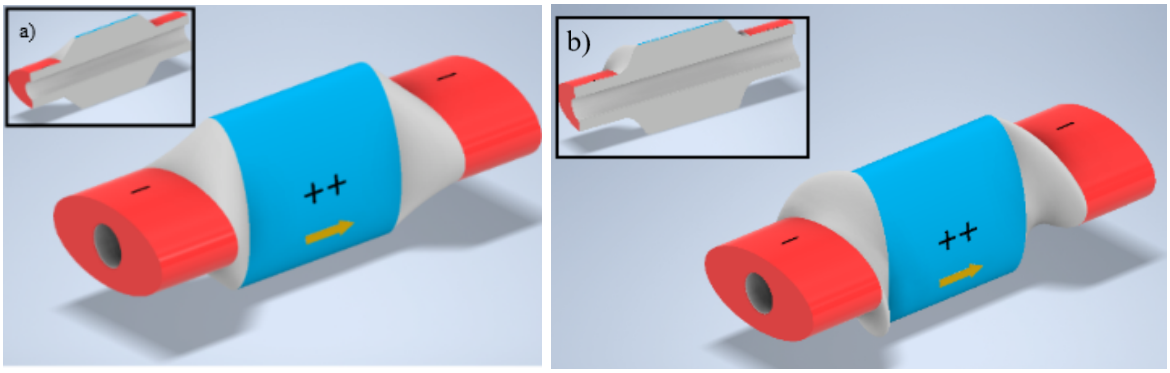

Figure 4.18: Quadrupole triplets used for total focusing. The insets show a cutaway view of the device. Red sections have negative gradients, blue sections have positive gradients for the current direction shown by the arrow. The +, - show the sign and relative strength of the quadrupole segment. a) The transition between segments goes through the equal semi-axis length point, which has a gradient of 0 T/m. This transition does not introduce multipoles. b) The transition between quadrupole segments is achieved by rotating the quadrupole field, which introduces many normal and skew higher order multipoles.

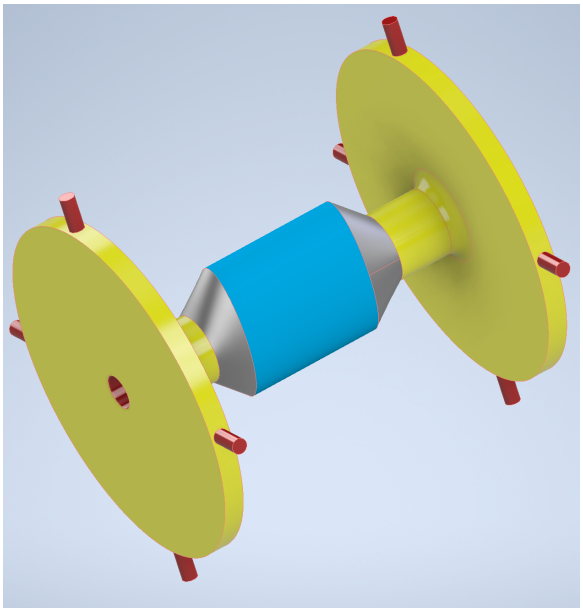

Figure 4.19: Monolithic quadrupole with zero (limited by fabrication error) higher order multipoles. Yellow regions have zero field, blue region has a pure quadrupole field. Gray transitional regions also have pure quadrupole fields.

CHAPTER 5

Microfabricated Panofsky Quadrupole

This chapter forms the basis of a manuscript that will be submitted soon to the journal Physical Review Accelerators and Beams. *Thank you to my coauthors Sophie Crisp, Alexander Odie, Pietro Musumeci, Rob Candler, and James Rosenzweig.*

5.1 Introduction

The current emphasis on smaller and cheaper accelerator systems requires a corresponding effort to develop more compact magnet beam optics. To this end, we present in this work a microfabricated Panofsky-like quadrupole as shown in Fig. 5.1, characterized through theory, simulation, and experiment. The benefits of such a device over other microfabricated quadrupole designs are the ease of fabrication, that it can be fabricated with an arbitrary length (from less than a millimeter to 100s millimeters), and the adjustable gap. The device can provide high quality magnetic gradients greater than 100 T/m.

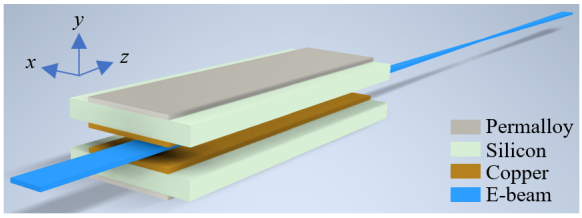

Figure 5.1: Model of the MPQ (with the indicated materials) focusing an electron beam. To focus this electron beam, the current in both copper sheets is directed in the $-z$ direction. We use the indicated coordinate system throughout this manuscript.

Conventional electromagnet quadrupoles with soft iron pole tips typically have a circular bore. The gradient can be analytically derived to be $B' = \frac{2\mu_0 NI}{r^2}$, where μ_0 is the permeability of free space, NI the number of amp-turns exciting each pole tip, and r is the bore radius. The ideal pole tip shape, determined from conformal mapping [116], assumes infinitely long poles and so will always be contaminated with higher order multipoles. Rectangular aperture quadrupoles, often known as Panofsky quadrupoles (PQs) [121], are composed of current sheets surrounded by a soft iron yoke as shown in Fig. 5.2a (both opaque and semitransparent regions) and do not suffer from such machining limitations. Draper *et al.* [122] showed theoretically that this geometry creates a pure dipole or quadrupole field (i.e., no higher order multipoles), depending on coil excitation, across the *entire* bore region. The gradient of a PQ is proportional to $1/d_g$ [121], where the gap d_g is the small dimension of the rectangular aperture. There are two major drawbacks of the PQ compared to conventional quadrupoles. First, as a current-dominated magnet that also has magnetic material, the field quality is very sensitive to conductor location [123]. The other drawback is the magnetic field strength is ∼4x lower than a conventional quadrupole with the same bore size and NI. As such, PQs have typically been used only where wide apertures are required, such as in spectrometers [121, 124], beam injection [125], and beam extraction [126]. More novel interpretations such as the twin-aperture PQ [127] and tunable combined function PQ [128, 129, 130] show the versatility of this magnet type. The highest gradient of any of these PQs was 15 T/m.

Despite the apparent drawbacks associated with using PQs, there are a few important advantages in favor of using microfabricated Panofsky quadrupoles (MPQs) as compact quadrupole magnets. First, the $1/d_g$ scaling of the gradient is beneficial as the device size (and therefore the gap) is decreased. Second, while the microfabrication of conventional quadrupoles [79] is very difficult and suffers from low yield and reliability, the fabrication of the MPQ is very simple by comparison and has a robust construction. Third, the magnetic length of the microscale conventional quadrupole is limited to ∼1 mm, but the magnetic length of the MPQ is limited only by substrate size (typically greater than 100 mm). There-

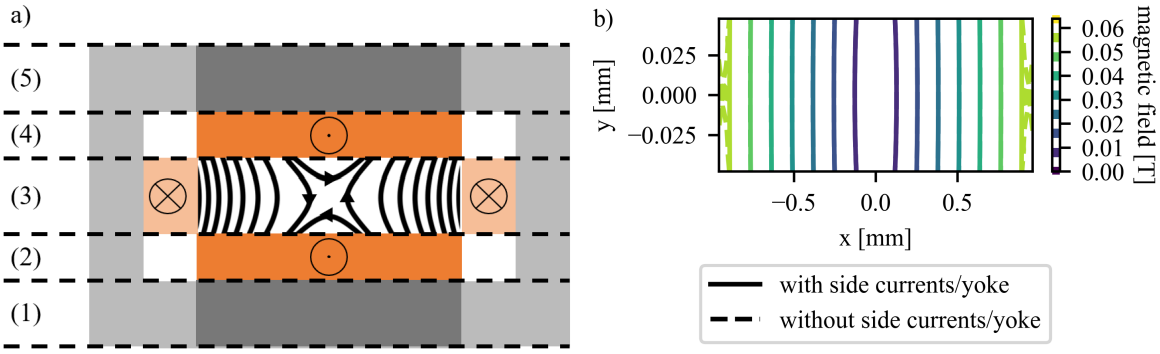

Figure 5.2: a) Depiction of PQ and its magnetic field contours. The current sheets are orange and are surrounded by the gray magnetic yoke. The microfabrication layers are delineated with dashed lines. The semitransparent regions of the PQ are not present in the MPQ design. b) the magnitude of the PQ transverse magnetic field with side currents and yokes (solid lines) and without (dashed lines). All appreciable variation is at the edges of the bore region.

fore, the inherently lower gradient of the MPQ can be compensated by longer length.

Table 5.1: Simulated device parameters

J (A/m^2)	current density	1×10^8
d_{Cu} (μm)	copper thickness	50
d_{yk} (μm)	yoke thickness	50, 300
d_{Si} (mm)	distance between copper and yoke	0.6
W (mm)	device width	2
d_g (mm)	gap between MPQ halves	0.1

The PQ can be visualized in a series of layers as shown in Fig. 5.2, which makes it amenable to microfabrication processes. A possible processing flow could be to form the 1) bottom magnetic yoke, 2) bottom thin copper trace, 3) side traces and yoke, 4) top thin copper trace, and 5) top magnetic yoke. The third layer thickness, which could exceed 100 μm, is the most problematic because electroplated films thicknesses greater than a few hundred microns often suffer from stress-induced delamination [131]. One could consider a hybrid device where most of the MPQ is microfabricated and the third layer is conventionally machined, but such approaches would have many issues to address in how to align, mount, and electrically insulate the various individual parts. The solution explored in this work is less

complicated: design the device width be much larger than other dimensions, such that the side traces and yoke can be omitted because they contribute little to the field in the magnet center. This device is also shown in Fig. 5.2a as only the opaque (not semitransparent) parts. We confirmed this hypothesis using a COMSOL Multiphysics simulation of the magnetic field magnitude of a device with parameters shown in Table 5.1. The results are shown in Fig. 5.2b, where we see the magnetic field of the devices with and without side currents and yokes differ only near the device edges. Note the extreme aspect ratio in the figure. A consequence of this result is that the top and bottom halves can be fabricated separately (even on the same silicon substrate), then assembled in the correct configuration with a mounting fixture.

5.2 Theory

Hand and Panofsky derived an expression to predict the gradient of the original rectangular aperture quadrupole using the standard assumptions that the device is very long and the permeability of soft magnetic material is very high.

We can use standard Ampere's Law, $\oint \vec{H} \cdot d\vec{l} = \iint J \cdot dA = I_{enclosed}$, to get a first order approximation of the magnetic fields of this geometry. The derivation using this technique for a standard Panofsky quadrupole is presented in the appendix; here we derive the magnetic field gradient of the MPQ using a similar technique.

The main assumptions are three-fold. We assume:

1. The device width is much larger than the bore width, such that $W \gg g$; this means that the magnetic field in the bore does not depend on y.

2. $\vec{H} \approx 0$ inside the yoke, which requires that the soft magnetic material have very high, field-independent permeability.

3. The device length is very long, such that there are no three-dimensional effects.

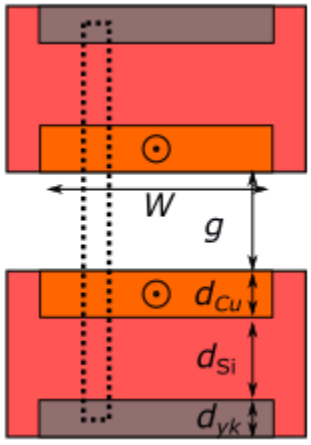

Figure 5.3: MPQ labeled with relevant parameters and the integration path used in the gradient derivation.

We note that the second condition comes from boundary conditions. Consider the interface between vacuum, interface 1, and a soft magnetic material, interface 2. In the absence of magnetic charge the normal component of the magnetic flux density is continuous across the interface, so $\vec{B}_{n1} = \vec{B}_{n2} \rightarrow \mu_1 \vec{H}_{n1} = \mu_2 \vec{H}_{n2}$. We then see that $\vec{H}_{n2} = \frac{\mu_1}{\mu_2}\vec{H}_{n1} \approx 0$ since $\mu_2 \gg \mu_1$.

We define the contour path of the integral along the dashed line shown in Fig. 5.3. The left and right vertical lines are located at x and $x + \Delta x$ respectively. Naturally, $H_y(x) \neq H_y(x + \Delta x)$ from assumption 1 above, so the contour integral gives

$$\oint \vec{H} \cdot d\vec{l}$$
$$= 2H_y(x)d_{Si} + 2H_y(x)d_{Cu} + H_y(x)g - (2H_y(x + \Delta x)d_{Si} + 2H_y(x + \Delta x)d_{Cu} + H_y(x + \Delta x)g)$$
$$= 2I_t \frac{\Delta x}{W}$$

where I_t is the total current in one of the current sheets. Rearranging the equation gives

$$\frac{H_y(x+\Delta x) - H_y(x)}{\Delta x} = \frac{2I_t}{W\left(g + 2d_{Cu} + 2d_{Si}\right)}$$

After taking the limit that Δx goes to 0 gives and converting to a magnetic flux density we arrive at the following expression for the magnetic field gradient:

$$\frac{dB_y}{dx} = B' = \frac{2\mu_0 I_t}{W\left(g + 2d_{Cu} + 2d_{Si}\right)} = \frac{2\mu_0 J d_{Cu}}{g + 2d_{Cu} + 2d_{Si}} \tag{5.1}$$

Where $I_t = J \cdot d_{Cu} \cdot W$ is the total current. Other parameters are explained in Table 5.1. This expression is equivalent to that derived by Hand and Panofsky if $d_{Si} = 0$, as was the case for the original Panofsky quadrupole. The same result can be derived by instead directing one side of the loop far away (along which $\vec{H}$ is approximately zero) instead of through the device at a nearby location and taking a limit to form the derivative like was shown here. One observation is that W enters Eq. 5.1 only from converting current density to current; we show later in this section that there is a more complicated relationship between B' and W not reflected in either of these expressions.

We investigated the limits over which this formula is valid using COMSOL. The simulations were 2D, as is the magnetic circuit analysis used to derive Eq. 5.1. The nominal parameters for the analysis are shown in Table 5.1. We used several different yokes. The "ideal" yoke has a fixed, high relative permeability of 8500 (corresponding to the measured low field permeability of the electroplated permalloy [92]). Magnetic saturation is not included in a constant permeability model and so the yoke thickness makes little difference – this was verified in simulations not shown here. We also simulated yokes with the measured MH curve of the electroplated permalloy with thicknesses of 50 and 300 μm to show saturation effects. We include a "yokeless" MPQ - this is the exactly as the two current sheet quadrupole (TCSQ) device derived in Chapter 2 and described in more detail in Chapter 4.

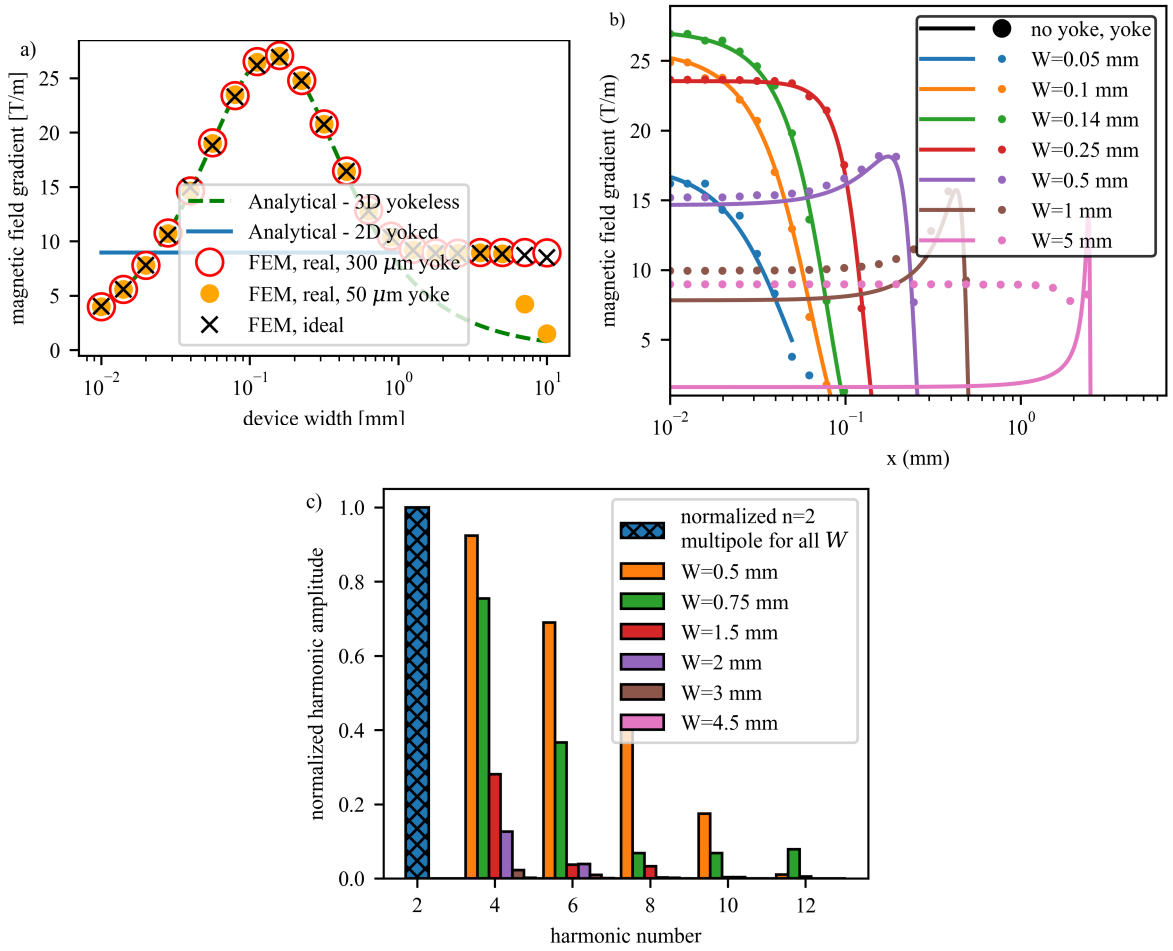

Figure 5.4: a) Comparison of theory and simulation of the gradient dB_y/dx in the center of the MPQ as a function of width. b) Transverse magnetic field gradient profile for a yoked (points) and yokeless (solid lines) MPQ for different widths. The parabolic nature of the yokeless gradient curves is somewhat obscured by the nature of the semilog plot. c) Normalized real multipole content of the MPQ (nominal parameters, except the gap was 1.5 mm) as a function of width.

We first investigated the relationship of gradient and device width in the case of constant current density, shown in Fig. 5.4. As Eq. 5.1 does not depend on W in the case of constant current density, we expect the relationship of B' and W to be constant, but FEM simulations in Fig. 5.4a show very different behavior. We see for large widths, the gradient matches Eq. 5.1 except for where the thin yoke saturates (around $W = 5$ mm). At very small device widths, where the "large width" assumption is invalid, the behavior resembles that of the

yokeless MPQ. The transition point between these two behaviors is around $W = 1$ mm for this geometry. To explain the formation of the peak in Fig. 5.4a, we have plotted the transverse gradient profile at several widths of the yokeless (dots) and yoked (lines) MPQ in Fig. 5.4b. We plot the gradient at positive x values only because of symmetry. Consider first the large width $W = 5$ mm device. There is a large peak in the gradient near the device edge at $x = 2.5$ mm. As the device width decreases this peak also moves to smaller x values. The gradient is constant over much of the device interior, and both the interior gradient and the edge gradient increase for as the device width decreases. However, the interior gradient increases faster than the edge gradients. At some width, in this case around $W = 0.25$ mm, the interior gradient and edge gradients are equal, creating a region of relatively uniform gradient across most of the device. At even smaller widths the interior gradient increases even further past the edge gradients, leading to a bulge in the gradient in the device center. We previously found the critical width for two copper sheets, at which this maximum gradient occurs, to be $W_c = \sqrt{g(g + 2d_{Cu})}$ (Eq. 4.2). For $g = 0.1$ mm and $d_{Cu} = 50$ μm we calculate $W_c = 0.14$ mm, which matches Fig. 5.4a,b. At even smaller widths, however, the largeness of the gap compared to the device width affects performance and the gradient approaches zero.

This behavior and previous assumptions of device width naturally lead to the question of how wide the MPQ needs to be to generate a good quality quadrupole field. The PQ has a pure quadrupole field, so this is also the goal for the MPQ. We show the normalized absolute values of the even-order multipoles as a function of width in Fig. 5.4c. We used the nominal device parameters for the simulation, but with a gap of 1.5 mm due to excessive numerical noise at smaller gaps. The distribution of higher order multipoles depends on the geometry, such as d_{Si}, g, and d_{Cu}, but in all cases the higher order multipoles were suppressed as the width increased. For example, if $d_{Si} = 0.6$ mm the width/gap ratio W/g needs to be approximately 4 to suppress the $n = 4$ harmonic to less than 1%, while if $d_{Si} = 0$ then only $W/g = 2.5$ is required to achieve the same level of harmonic suppression.

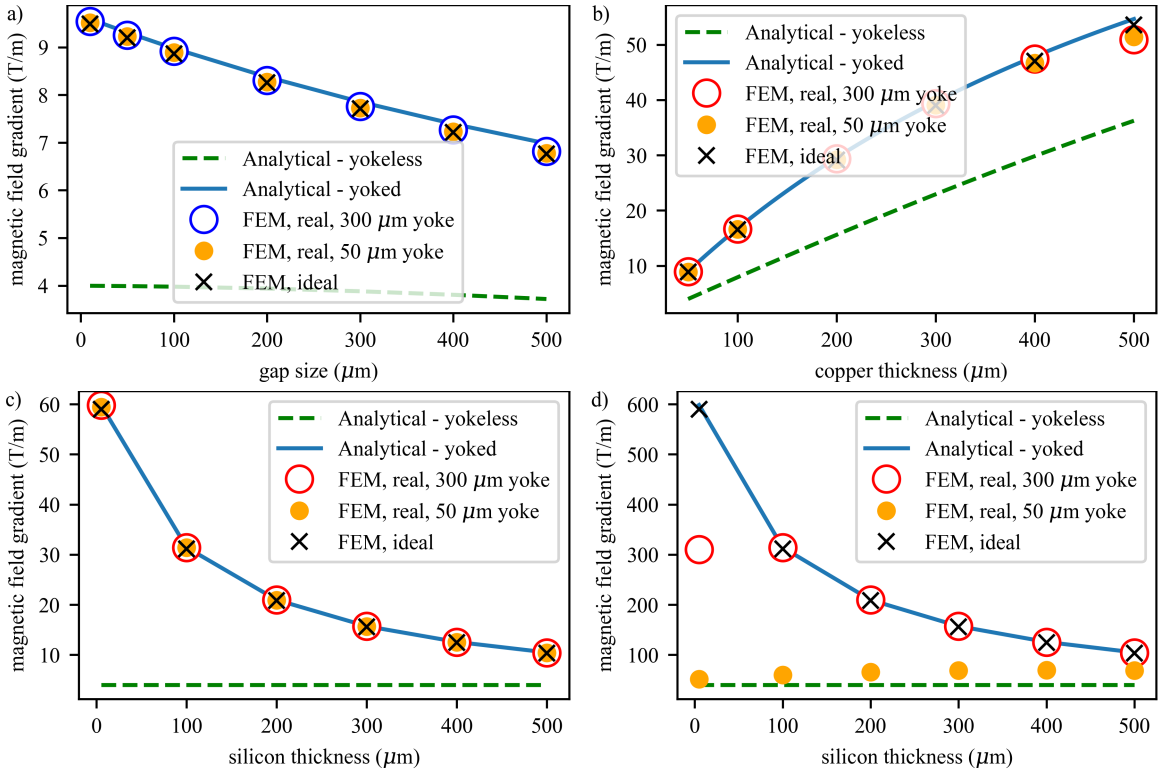

Figure 5.5: Comparison of theory and simulation for the magnetic field gradient, dB_y/dx, at the center of the MPQ while changing the a) gap d_g, b) copper thickness d_{Cu}, c) silicon thickness d_{Si} at $J = 1 \times 10^8$ A/m^2 and d) silicon thickness at $J = 1 \times 10^9$ A/m^2. The ideal material is assumed to have a fixed relative permeability of 8500 (i.e., no saturation), while the real material utilizes experimentally measured MH curves.

We also investigated in Fig. 5.5 the effects of varying the gap (part a), copper thickness (part b), and silicon thickness (parts c-d) in the case of constant current density. We see good agreement in general; the few instances of poor agreement stem from either a) breaking the derivation assumptions that lead to Eq. 5.1 or b) magnetic saturation. For example, we see that all FEM results depart from the analytical expectation in Fig. 5.5b for large copper thicknesses because of violating the derivation assumptions of large width compared to other device dimensions. Magnetic saturation is evident in the simulation when 1) the ideal material model (fixed permeability) behavior differs from that of the models that incorporate "real" magnetic material properties, or 2) when the behaviors of the models with thin and thick yoke material are different. Both indications are prominent in Fig. 5.5d, which features the same device as Fig. 5.5c but with a higher current density of $J = 1 \times 10^9$ A/m^2. The ideal yoke model tracks perfectly with the analytical 2D result, showing that any deviation does not come from violating derivation assumptions. We also see, however, that the thin 50 μm yoke is saturated for all d_{Si}, but the thick yoke does not fully saturate until $d_{Si} < 100\mu$m, where both of these models fail to match up to the prediction of Eq. 5.1.

The MPQ can also be operated in dipole mode. Dipole mode requires the currents to be of the same magnitude but in opposite directions (for quadrupole mode, the currents are the same magnitude and the same direction). The dipole field can be derived using magnetic circuit analysis to be

$$B_x = \mu_0 J d_{Cu} = \mu_0 \frac{I}{W} \tag{5.2}$$

The dipole field does not depend on the gap because it was assumed that the width was much larger than the gap (or the silicon thickness d_{Si}) - this was verified using FEMM in simulations not shown here. Interestingly, one can use conformal mapping to derive the profile of current sheets to generate a pure dipole field, and one solution is two wide, flat current sheets as described here. In addition, it is assumed that d_{Si} is relatively smaller

than other dimensions. As an example of field magnitudes that can be expected, for $J = 1 \times 10^9$ A/m^2 and $d_{Cu} = 50$ μm, $B_x = 6.3$ mT.

The MPQ can generate dipole and quadrupole fields simultaneously by simply superimposing the currents. For instance, if one determines that the desired quadrupole field can be obtained with 20 A and the desired dipole field can be obtained by using 5 A, one can generate both fields by using 25 A in one copper sheet and 15 A in the other sheet. In general, the effective quadrupole and dipole currents can be extracted from the currents in the top (I_{top}) and bottom (I_{bot}) MPQ halves:

$$I_{eq,dipole} = \frac{I_{top} - I_{bot}}{2} \tag{5.3a}$$

$$I_{eq,quad} = \frac{I_{top} + I_{bot}}{2} \tag{5.3b}$$

$$\tag{5.3c}$$

A final observation about the dipole mode of the MPQ is that, due to the geometry, the dipole mode can only generate a B_x component, leading to a vertical y displacement; the MPQ cannot generate a B_y component that would allow for horizontal beam steering.

5.3 Three-dimensional magnetic simulations with leads

The MPQ has symmetrical electrical leads to facilitate current flow into the quadrupole active region. We first used asymmetrical leads, but found that the beam focused *and* rotated, so symmetrical leads were adopted despite the more difficult fabrication integration. The previous simulations do not consider the effect of these, or the leads inside the PCB, on the quadrupole performance. In this section we present RADIA [132] simulations to provide a more complete view of device behavior. The device parameters for this section are the same

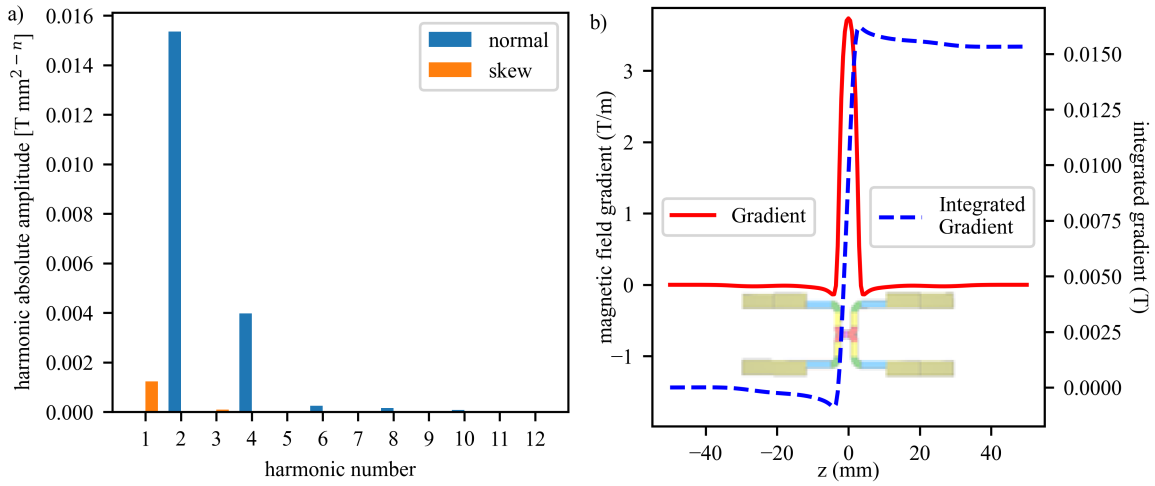

Figure 5.6: Analysis of device and PCB together using nominal parameters, except with a gap of 1.5 mm. a) harmonic analysis of MPQ with leads at a 0.5 mm reference radius. b) Longitudinal variation of center gradient (left axis) and cumulatively integrated center gradient (right axis). The overlaid graphic of the bottom MPQ half shows the PCB leads in tan; all other colors are the device and device leads as fabricated on the silicon die.

as for the previous section simulations, except the gap is set to 1.5 mm to better compare with experimental results shown in the next section.

Figure 5.6a shows the integrated magnetic field harmonic components. The quadrupole moment (n=2) has a value of 0.0153 T. The effective length is computed to be 4.1 mm, despite the active region measuring physically to be 6.7 mm long. This is due in part to the curved nature of the leads. The current is directed completely in the z direction only over about 1 mm; the current in rest of the device also has some x component due to the curved nature of the leads, which effectively reduces the amount of current traveling in the z direction. We see non-zero multipoles at every even order and a non-zero skew dipole moment ($n = 1$), indicating the presence of a dipole magnetic field in the x direction. The presence of even multipole harmonics is expected from the 180-degree symmetry. The skew dipole is *not* present in simulations of the two straight current sheets (the configuration shown in Fig. 5.2b) as seen in Fig. 5.4c, so this skew dipole moment can be attributed to the device and PCB leads.

Figure 5.6b shows the gradient in the device center as a function of z (red solid line, left axis), with the same curve cumulatively integrated (dashed blue line, right axis). The device is overlaid with the same scale as the z axis. The cumulatively integrated curve shows the relative contributions of each part of the device to the integrated gradient. The initial value is 0 T, and the final value is 0.0153 T, matching the value already shown in Fig. 5.6a. We see that all of the positive contributions to the integrated gradient happens inside the device active region. We also see, however, that the integrated gradient decreases slightly in the vicinity of the device and PCB traces. This, in addition to the curved leads, makes the calculated effective magnetic length smaller.

The MPQ does not have a theoretical guarantee of perfect field quality across the bore region like the conventional Panofksy quadrupole because it lacks a continuous yoke and side current windings. We simulated two devices using RADIA and use focal length variation to quantify the field quality. The first device has a small aperture (1 mm width, 0.1 mm gap) and the second device has a larger aperture corresponding to the experimental device (2 mm wide, 1.5 mm gap). For the small aperture, the focal length variation from the center value is +10%/-23%, with a 1% good field region size of 0.33 mm x 0.06 mm. For the large aperture device the focal length variation from the center across the entire bore is, at worst, +27%/-33%, and the size of the 1% good field region is 0.5 mm x 0.25 mm. As expected, the field quality and relative size of the good field region are much better in the small aperture device than the large aperture device. This is mostly due to the larger W/g ratio. Once conclusion, therefore, is that one could expect to see beam aberrations if the gap is too large.

5.4 Experimental work

5.4.1 Fabrication

The fabrication process flow for this device is shown in Fig. 5.8a. First, the silicon is electrically insulated by depositing 300 nm silicon nitride on both sides of the 0.6 mm

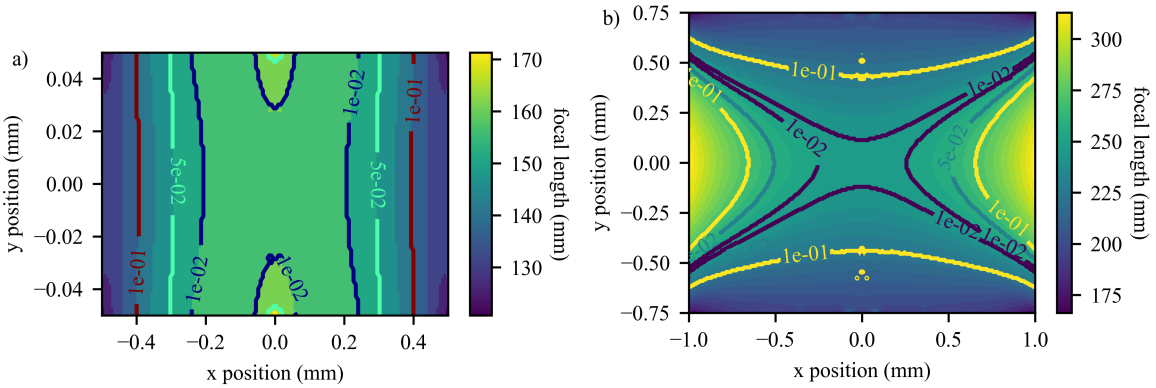

Figure 5.7: Device focal length in millimeters with a current of 20 A ($J = 2 \times 10^8$ A/m^2) for the a) small aperture (1 mm width, 100 μm gap) devices and b) large aperture (2 mm wide, 1.5 mm gap) devices. The colormap shows the focal length across the device aperture, and the contour lines show the 1%, 5%, and 10% "good focal length" regions.

thick wafer using low-pressure chemical vapor deposition (Tystar Titan II). We sputter an electroplating seed layer of 40 nm titanium and 300 nm copper (CVC 601) on the wafer backside. We use thick film photoresist (AZ 50XT) to define the yoke region and electroplate the permalloy yoke to a height of 50 μm using a process previously developed by our group [92]. We then sputter an electroplating seed layer on the front side, use thick film photoresist to define the copper trace region, then electroplate copper (Technic Elevate Cu 6320) to a height of 50 μm. The wafer is diced, and the devices are mounted on a PCB for testing as shown in Fig. 5.8b. Electrical interface from device to PCB is done with thick copper sheets to handle 10s A of current (Fig 5.8b). The PCB-mounted devices are aligned on their respective aluminum mount pieces, then brought together as shown in Fig. 5.8c.

We note that decreasing the distance between the copper conductor and yoke, i.e., reducing d_{Si}, is important to achieve the maximum gradient according to Eq. 5.1. We attempted to reduce d_{Si} by etching trenches in the silicon for both the copper and permalloy, electroplating into the trenches, then using chemical mechanical polishing (CMP) to planarize the surface. This results in the device shown in Fig. 5.9a. For film thicknesses of 50 μm and a wafer thickness of 0.6 mm, this would result in d_{Si}=0.5 mm instead of d_{Si}=0.6 mm. However, all these attempts failed. When the trenches were etched using deep reactive ion

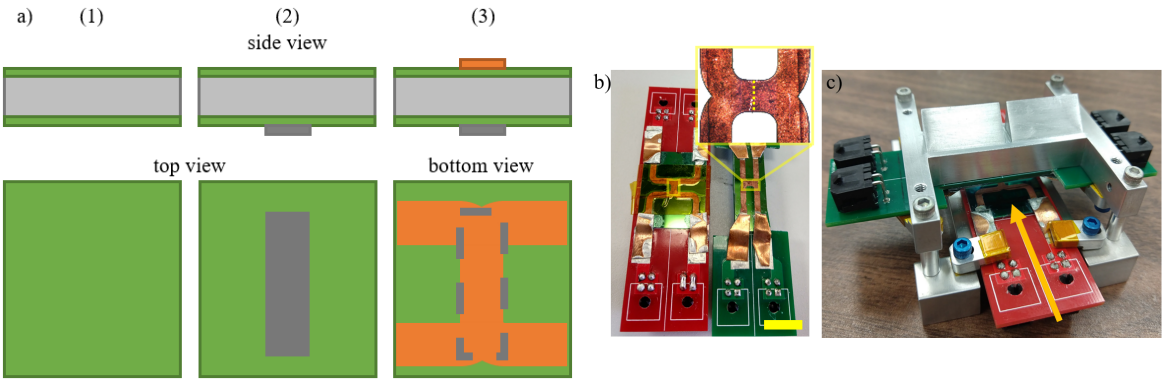

Figure 5.8: a) fabrication flow showing the side and top/bottom views of fabrication steps of 1) electrical insulation, 2) yoke electroplating, and 3) copper electroplating on the opposite side, with the yoke extents shown by dashed lines. b) MPQs mounted on PCBs. The yellow scale bar is 1 cm. The region of the quadrupole is shown by a yellow box for each half of the MPQ, and the inset is an optical microscope image of the right device's active region. The dotted yellow line across the device has a length of 2 mm. c) the fully assembled MPQ in the aluminum mount, with the beam propagation direction shown by the orange arrow.

etching (DRIE), the second trench etch consistently fell victim to micromasking. This happens because the metallic films on the wafer backside drastically changed the wafer cooling profile; this causes incomplete etching of the passivation layer, which leads to micromasking and etch failure. We successfully etched the trenches using KOH etching [133] to make the device shown in Fig. 5.9b (note the characteristic 54.7 degree etch angle), but the surface quality was not as good as the well-etched DRIE trenches [134, 135]. More significantly, the permalloy film stress near the trench edges is significantly different than the rest of the film [136], which results in film delamination. Notably we didn't have this problem with the first device etched via DRIE because a) the copper films have lower intrinsic stress, and b) we plated over the entire wafer instead of just in the trenches; the permalloy bath does not have enough metal ions to plate the entire wafer with 50 μm of permalloy. For these reasons we decided to circumvent the surface quality and edge stress issues by using through-mold electroplating for this proof-of-concept device as shown in Fig. 5.9c, though this has the largest d_{Si} and lowest gradient. To reduce the copper-yoke separation to approximately zero, one could imagine a device shown in Fig. 5.9d, fabricated by etching a deep trench with either

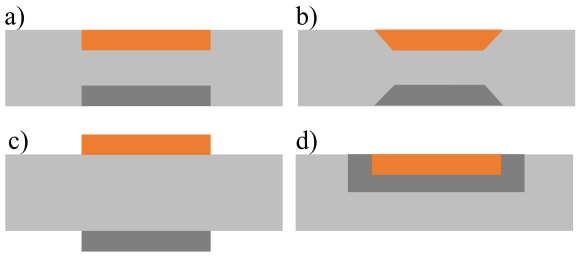

Figure 5.9: MPQ half device fabricated via a) DRIE, b) KOH etching, c) through-mold plating (represents actual device), and d) ideal device fabricated via DRIE.

DRIE or KOH etching, partially filling it with electroplated permalloy, then filling the rest of the trench with copper, followed by a final planarizing step. This device would inherently have the fabrication challenges of the other failed attempts, however, and so was not attempted.

5.4.2 Thermal characterization

Thermal simulations were performed using COMSOL for three different "devices" and compared with experimental measurements obtained from a thermal camera (ThermalExpert TE-Q1 Pro) using the right PCB-mounted device from Fig. 5.8b. The first modeled device is that of the MPQ fabricated in PCB material, i.e., with copper traces embedded directly into PCB material. The second is of the MPQ fabricated on silicon and mounted on a PCB board as demonstrated in this work. In both cases, the PCB is "mounted" on a thermal reservoir held at 293 K. One example of a constant temperature thermal reservoir could be an actively cooled metal block. The third situation is that of a MPQ fabricated in silicon and mounted directly to the thermal reservoir. The maximum steady state temperature of the devices as a function of current is plotted in Fig 5.10. We see that the all-PCB device can tolerate the least amount of current per unit temperature change, followed closely by the MPQ mounted on a PCB. The PCB-fabricated device performs poorly because of the typically small ($\sim$1 W/(m K)) thermal conductivity of PCB material at room temperature. The silicon-fabricated, PCB-mounted device performs slightly better as the silicon

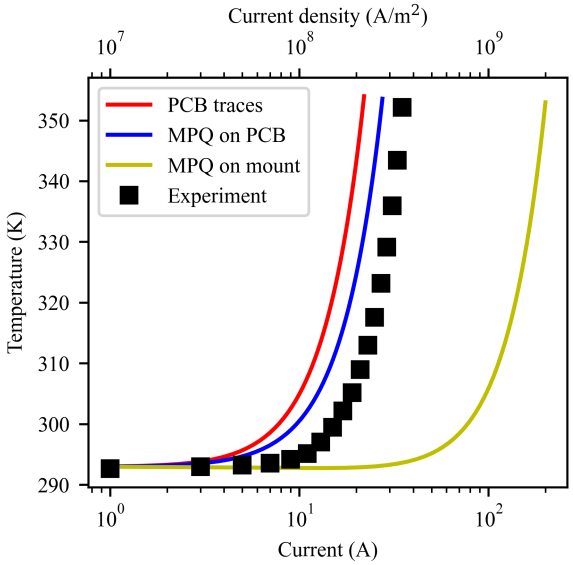

Figure 5.10: Steady-state COMSOL thermal simulations at room temperature of devices fabricated in 1) PCB (FR4) material, 2) silicon mounted on PCB, and 3) silicon mounted on a cooled metal mount, compared with the experimental device (similar to device 2). The top x-axis is simply a scaled version of the bottom x-axis.

has a much higher thermal conductivity (∼100 W/(m K)) and spreads the generated heat over a wider area, but still suffers from high PCB thermal resistance. The MPQ mounted directly on a metallic mount can tolerate approximately 10 times more current than the PCB-mounted MPQ because there is no thermally resistive PCB material. We see that the fabricated device tolerates slightly more current than the corresponding simulated PCB-mounted silicon-fabricated device, which we attribute to the large copper electrical leads soldered to the device. These leads can dissipate substantial heat but were not included in the COMSOL model. Another small source of error could be air convection, which also was not included in the COMSOL model, but this is unlikely because the thermal conductivity of air (∼0.025 W/(m K)) is much smaller than that of PCB material.

5.4.3 Direct field measurement via Hall probe

We first used a Hall probe to map the magnetic field in the MPQ. The gap was set to 5.6 mm to accommodate the Hall probe thickness, and the total current through each MPQ half was 20 A (2×10^8 A/m^2). We measured $B' = dB_y/dx$, the transverse gradient, along the z axis, which is the beam propagation direction. The experimental results match magnetostatic simulations from RADIA within 10% which is shown in Fig. 5.11. The integrated gradient for this low-current, large-gap configuration is 0.0048 T, the maximum gradient is 1 T/m, so the effective length is 4.8 mm.

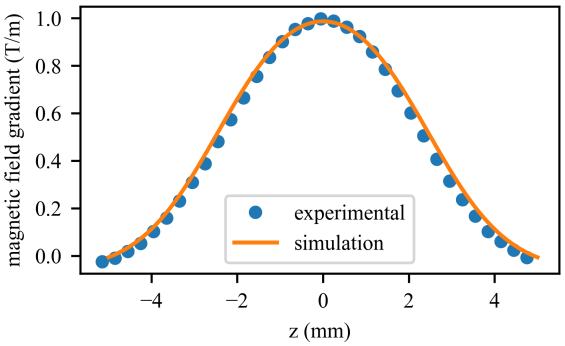

Figure 5.11: Measured gradient (dB_y/dx) along z-axis at $x = y = 0$ at a current of 20 A (2×10^8 A/m^2) and a 5.6 mm gap.

5.4.4 Electron beam measurement

Focusing of a relativistic electron beam was performed at the UCLA Pegasus beamline [137]. The electron beam from the radiofrequency photoinjector [138] is accelerated to an energy of 3.2 MeV ($\gamma = 7.24$), focused by the MPQ, then imaged on a screen 0.5 m downstream by a Princeton Instruments PI-MAX 3 camera. Solenoidal focusing was used to collimate the beam, but no other focusing magnets were used. The MPQ gap was set to 1.5 mm for the beamline experiments. At least five images were taken for each current value, both before and while the MPQ was powered. We parameterized each shot by fitting with a two-dimensional Gaussian distribution model and averaged the parameters for each group of

shots. The beam displacement in x and y is calculated as the beam centroid shift between shots with the MPQ powered and not powered. The beam size radius was taken to be twice the standard deviation of the fitted Gaussian curve, 2σ, in x and y directions.

For the first experiment (Fig. 5.12a-b) the current in both MPQ halves was equal and in the $-z$ direction (for clarity the current magnitude is plotted). As shown in Fig. 5.12a, the beam was fully focused in the x direction at a current of 22 A to 335 μm. The beam size in the y direction continually increased with the current magnitude as expected. The solid lines show the least-squares parabolic fit [139]; the data was well-approximated by a beam envelope (as represented in Eq. 2.13) with the following values for the second-order beam moments: $\sigma_{x_0} = 1.12\,\text{mm}, \sigma_{x_0 x_0'} = -8.9 \times 10^{-7}\,\text{m}$, $\sigma_{x_0'} = 8.6 \times 10^{-4}, \sigma_{y_0} = 0.98\,\text{mm}, \sigma_{y_0 y_0'} = -4.3 \times 10^{-8}\,\text{m}, \sigma_{y_0'} = 8.6 \times 10^{-4}$. This leads to calculated emittances of 0.38 and 0.84 μm-rad in the x and y directions respectively, which are reasonable values for the beamline. The focal length as a function of current, as calculated by RADIA, was $f = 8.65/I[\text{A}]$ for the uncompensated case and $f = 13.56/I[\text{A}]$ for the compensated case. The calculated gradient at 40 A was 11.2 T/m.

While the RADIA simulation predicted a small vertical displacement as seen in Fig. 5.12b (which also matches with the skew dipole moment calculated in Fig. 5.6), the measured displacement in the same subfigure was much larger. We found experimentally that the displacement can be compensated by using approximately four times more current in the top MPQ half to superimpose a dipole field as suggested in a previous section. We show the beam size and displacement in this compensated scenario in Fig. 5.12c,d. Without compensation, the vertical beam displacement was over 3 mm at 40 A (Fig. 5.12b) but with current compensation, the displacement was reduced to less than 0.15 mm (Fig. 5.12d). The data in Fig. 5.12c seem to suggest that the minimum beam size was achieved near the maximum current value of 40 A in the top MPQ half, which would be reasonable because the equivalent quadrupole current would have been 25 A (per Eq. 5.3), but as this is only just above the 22 A focusing current found in the uncompensated experiment and the number of

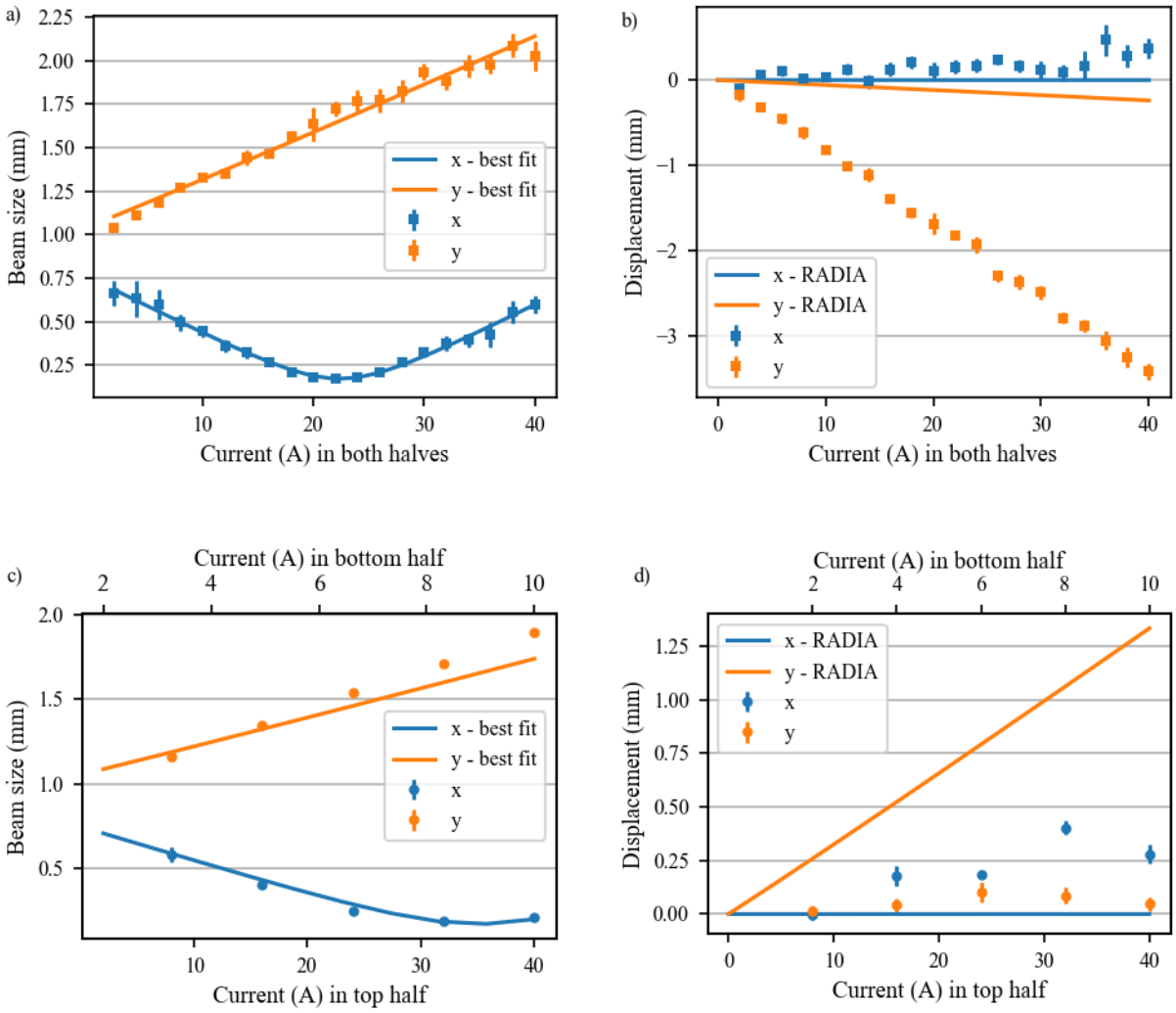

Figure 5.12: Beam size and beam displacement as a function of current magnitude. a-b) beam size and displacement, respectively, where the current in both halves was the same. c-d) compensated experiment, where the top half used four times as much current as the bottom half to cancel the beam displacement. The error bars, most too small to see, denote one standard deviation of at least five measurements.

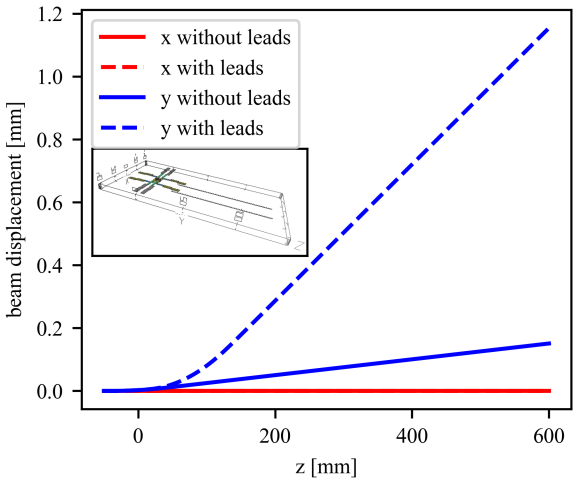

Figure 5.13: RADIA simulations without (solid lines) and with (dashed lines) extra 100 mm long leads on the back of device, showing the effects on the overall beam displacement in both x and y directions. The inset shows the device with the extra leads.

data points are low, a claim to have found the minimum beam size is tenuous.

We found after doing scans of the individual device halves, and finding good agreement with RADIA predictions, is that the most likely candidate for the anomalous beam deflection is that some electrical connection wires to the bottom half of the MPQ, approximately 100 mm long, may not have been routed away sufficiently from the beam axis during the experiment. We show in Fig. 5.13 the effect such wires could have on the beam with a current of 22 A, in both the x (horizontal) and y (vertical) directions. The effect on focal length is minimal and so is not shown here. We see that the total displacement is nearly 1 mm at 22 A (gray line), whereas the experimentally measured displacement was nearly 2 mm at the same current. However, we do not know the exact location or angle of these wires during the experiment which introduces large uncertainties for this simple example. However, we believe that the vertical deflection could be explained in large part or completely by these extra wires, and that the current compensation of the device was sufficient to cancel the effects of these extra wires.

We also investigated the effect of 1) displacing the top half of the MPQ horizontally (i.e. in the x direction) with respect to the bottom half of the MPQ without shifting the beam

propagation axis and 2) changing the yaw angle, i.e., rotating the entire device around the y axis. The current was 22 A in both MPQ halves. The results are shown in Fig. 5.14. In both figures the solid lines correspond to the beam displacement on the left y-axis, and the points correspond to the focal length on the right y-axis. We see in Fig. 5.14a that the displacement of the top MPQ half has a pronounced effect on both the beam displacement and focal length. The beam displacements in x and y are both significant as well. Changing the yaw angle, as shown in Fig. 5.14b, does not contribute significantly by itself to either focal length degradation or any beam shift, at least for the small range investigated here, though it can serve to couple and modify the effects of other misalignments and so should not be ignored.

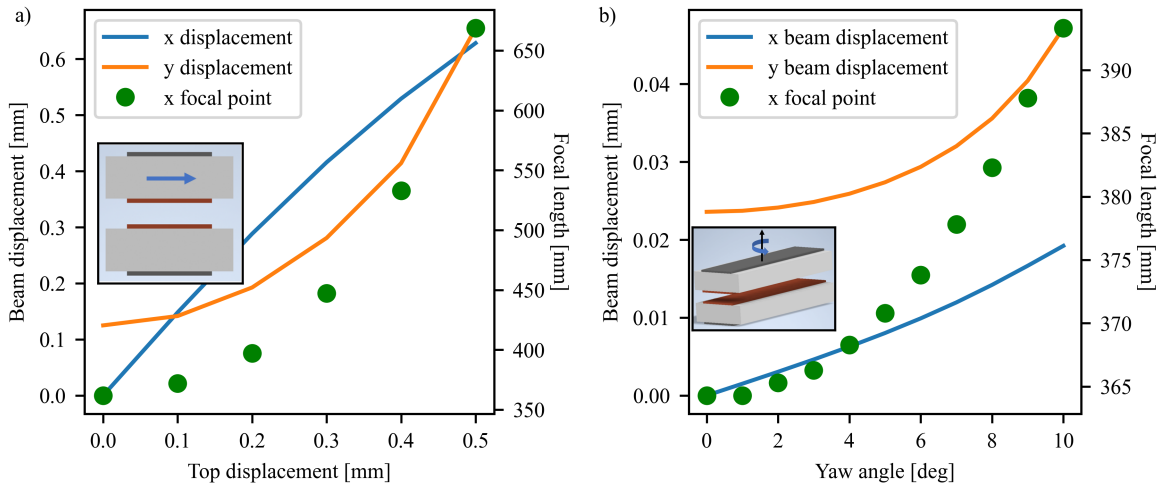

Figure 5.14: RADIA simulations showing the effect of a) displacing the top half and b) changing the yaw angle (i.e., rotation around the z axis) on the beam size and focal length. The insets show the type of misalignment under study.

5.5 Future designs

There are several other ways in which a second generation MPQ could improve substantially on the proof-of-concept shown here.

Using through-silicon vias would improve the field quality of the MPQ significantly.

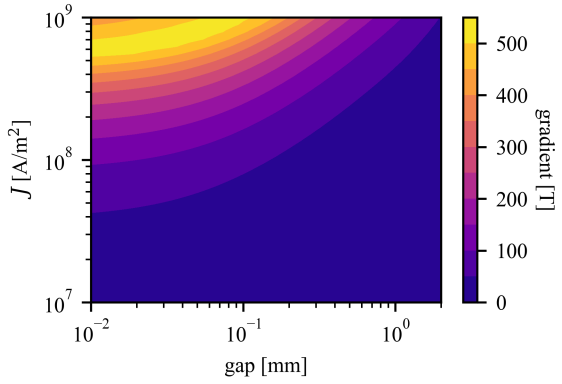

Figure 5.15: a) RADIA simulation showing the gradient in the center of the 2 mm wide MPQ as a function of current density and gap with $d_{Si} = 5$ μm, $d_{Cu} = 50$ μm and $d_{yk} = 300$ μm.

Such vias route the current to the backside of the substrate instead of to the sides, which mostly eliminate harmful fringing entrance fields as shown by the hand-assembled quadrupole multipole calculation in Fig. 5.18b. Ensuring conductor and yoke flatness by using chemical-mechanical polishing would also aid in reducing field errors.

The gradient could be substantially increased by reducing d_{Si}. The gradient in the center of the device as a function of gap and current, with $d_{Si} = 5$ μm and $d_{yk} = 300$ μm, is shown in Fig. 5.15. We see that while the maximum gradient that we showed experimentally was 11.2 T/m, the maximum possible gradient at higher (but possible) current densities and narrow gaps approaches 600 T/m if d_{Si} is small.

As a concrete example of how reducing d_{Si} improves the efficiency and utility of the MPQ, consider a fairly typical small bore (8 mm) quadrupole magnet used in the undulator section of the Linac Coherent Light Source [140] that has a maximum integrated gradient of 3.6 T and consumes 27 W in the magnet coils. This equates to 0.13 T/W, or 0.13 T of integrated gradient per watt of power. The total power consumption of both halves of the MPQ, not including extraneous wiring, was measured to be approximately 0.34 W at 10 A. With nominal parameters in Table 5.1, we calculate the integrated gradient via RADIA simulation to be 0.043 T, and so the integrated gradient per watt of power expended is also

calculated to be 0.13 T/W for the MPQ. That is with large d_{Si}, however; with $d_{Si} = 0$ the integrated gradient is 0.27 T at 10 A. The power loss would be the same (0.34 W), which leads to 0.79 T/W, which is approximately six times higher than the conventional quadrupole.

5.5.1 Microengineered quadrupole

One criticism is that the MPQ could be simply fabricated through methods other than microfabrication. To address this valid concern, we assembled an MPQ-like device with $d_{Si} \approx 0$ but with copper tape and discrete yoke pieces. We fabricated the yoke by waterjet cutting a 0.5 mm thick sheet of as-rolled vanadium permendur (Goodfellow Inc.) into 2 mm x 10 mm rectangles. Using vanadium permendur instead of electroplated permalloy has several advantages over electroplated permalloy: higher permeability (10,000 instead of 8500), larger thickness (0.5 mm instead of 0.05 mm), and higher saturation magnetization (2.1 T, instead of 0.8 - 1.1 T), so the potential for high gradients is maximized by this material choice.

After the yokes were machined, they were mounted and aligned on repurposed pieces of the original MPQ mount with high thermal conductivity double-sided tape. Adhesive copper tape was used as the conductor. It was cut to 2 mm wide using a Cri-cut craft machine. The copper tape thickness is 50 μm on average. No insulation was provided between the copper tape and yoke because that would substantially increase the distance between the yoke and copper sheet. Although the yoke and copper tape are in direct electrical contact, the lack of insulation should not cause any issues because 1) the adhesive contact between copper and yoke is not an ideal electrical connection and 2) the resistivity of vanadium permendur is roughly 10 times that of copper, meaning that little current would pass into the yoke even with good electrical contact. We used 4 mm spacers to maintain a constant gap, resulting in a 2.8 mm gap between the copper sheets. A picture of the device is shown in Fig. 5.16

We measured the magnetic field with the two-dimensional scanner described elsewhere

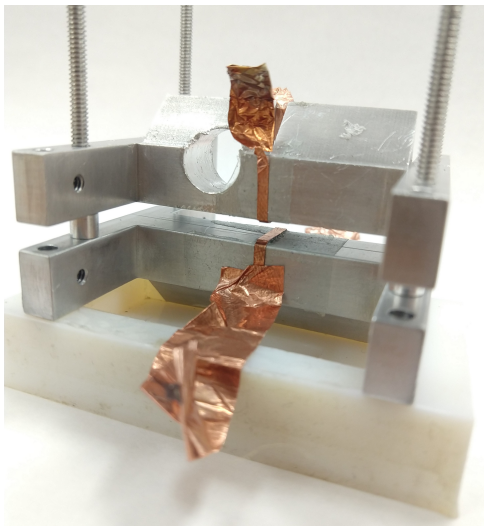

Figure 5.16: Picture of assembled quadrupole.

and compared the results with RADIA simulations of the same structure. The current was set to 5 A ($J = 5 \times 10^7\,\mathrm{A/m^2}$) and the results are shown in Fig. 5.17. In Fig. 5.17a we see the transverse field at $z = 0$ and that it matches well with the RADIA simulation. We note that the quadrupole has "good" characteristics only if the implicit assumptions are satisfied, i.e., the gap is small compared to the gap. In this case the gap is not small to other dimensions, and so 1) the transverse gradient is not uniform and b) the measured and simulated gradient ($\sim$ 1.3 T/m) does not reach the 2D value (2.1 T/m) predicted by Eq. 5.1. Figure 5.17b shows the variation of the central gradient along the device axis, where again we see good agreement between simulation and experiment. In Fig. 5.17 we also plotted the simulations using the nominal MPQ silicon thickness of 0.6 mm, where we see that reducing the distance from 0.6 mm to 50 μm (a rough estimate of the adhesive layer thickness) increases the gradient by nearly a factor of 2.

One advantage of this device over the as-fabricated MPQ is the vertical current leads that should contribute negligibly to the field in the gap. The full as-simulated device with leads is shown in Fig. 5.18a, where the permendur yokes are red and everything else is copper. The simple lead-free device, which intuitively has the lowest harmonic level, is composed of those

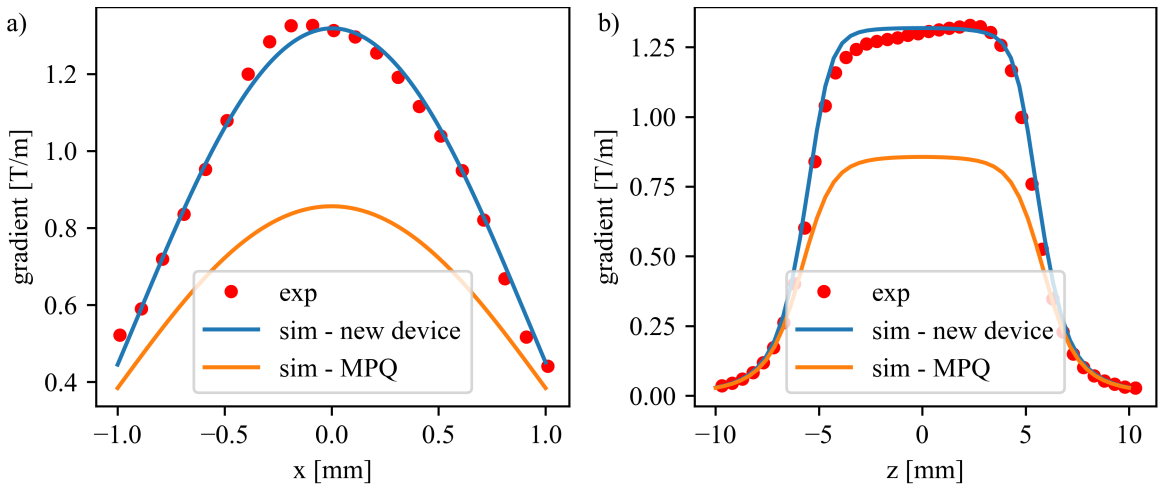

Figure 5.17: a) Measured transverse field gradient at $z = 0$ compared with simulation of the hand-assembled device and the MPQ with the same parameters but with $d_{Si} = 0.6$ mm. b) Transverse gradient along beam axis, compared with simulation of the hand assembled device and MPQ.

parts of Fig. 5.18a contained within the yellow box, or in other words, only the two parallel copper sheets and their yokes. The multipole content was calculated for both devices and is shown in Fig. 5.18b, which shows virtually no difference between the two structures. This makes sense, because one would not expect the leads to contribute much magnetic field to the region inside the gap.

There are some concerns about the performance of this type of device. First, there are many sources of manufacturing error to which we can attribute field errors, such as thickness variation of the copper tape, cutting of both copper tape and yoke, and misalignment. These difficulties are engineering issues, not fundamental physics issues. As with the MPQ, the device performance is limited by its thermal characteristics. There are two main issues. The first is that even "high thermal conductivity" adhesive and tape is very thermally resistive compared to metal or silicon, and there are two layers of such adhesive in this device. These layers do not exist in the MPQ, so we anticipate that this device cannot handle the high current densities that the MPQ allows. Secondly, heat generated by the copper current sheets must be dissipated directly through the yoke and raise the yoke's

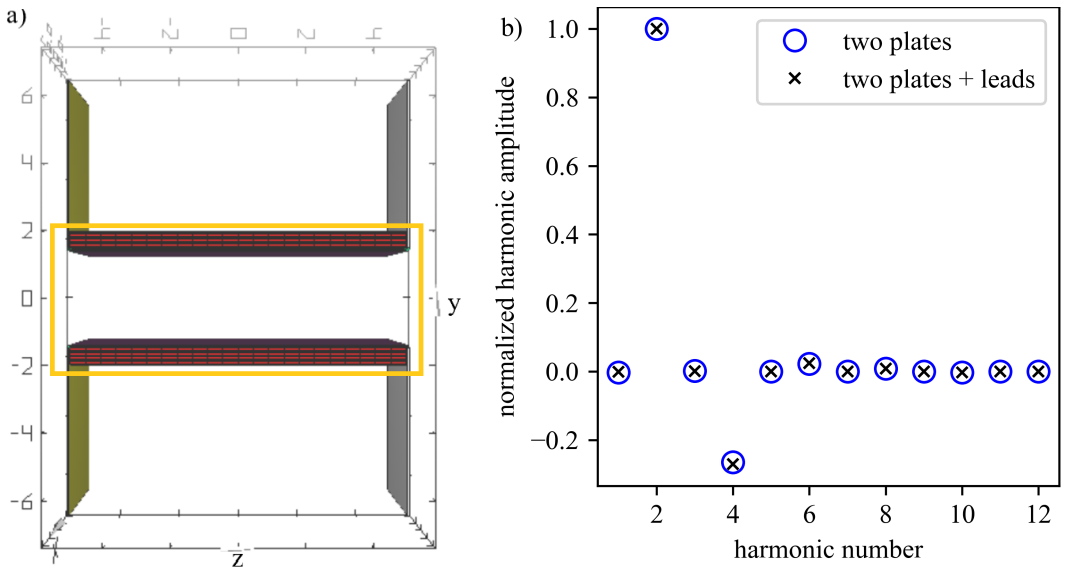

Figure 5.18: a) the two structures under consideration as constructed in RADIA. The lead-free model is contained within the yellow rectangle and is composed of only the two parallel copper sheets and yokes. The full model includes all the leads shown. b) the calculated multipoles of both RADIA models.

temperature. High temperatures negatively impact the magnetic properties of the yoke, and therefore the gradient.

5.6 Conclusion

We present the design, fabrication, and characterization of a microfabricated Panofsky-style quadrupole. We successfully demonstrated focusing of a 3.2 MeV electron beam. While the focal length was longer, and the vertical displacement larger, than expected, we showed through RADIA simulations that small misalignments due to hand assembling of the device could plausibly account for these errors. We showed that an MPQ-like device can be fabricated using more conventional techniques; however, we expect the thermal response to be worse than the MPQ while retaining the alignment challenges of the microfabricated MPQ. We also provide several design improvements that would be beneficial in a second-generation device.

CHAPTER 6

Final conclusion

This work builds on the substantial work of others using microfabrication to make miniature accelerator components, with the ultimate goal of more compact, cheaper, and accessible accelerators.

To this end we microfabricated two electromagnet devices. The first was a 1.2 mm electromagnet undulator that incorporates a thick, laser-machined yoke to increase the field. The second was a Panofsky-like quadrupole that has a simple fabrication process and has the possibility of achieving 100s T/m field gradients if engineered appropriately, along with arbitrary length that is limited only by the substrate size.

We also investigated several devices that used more conventional fabrication techniques, but are still "miniature" in nature. We demonstrated a Panofsky-like quadrupole similar to the microfabricated version that had a superior geometry with vertically aligned leads and small conductor-yoke distance, but the thermal behavior is worse than the microfabricated version which somewhat mitigates the other advantages. We also showed that current-carrying sheets can line the inside of an undulator to produce a quadrupole field, and that the field quality can be optimized by modifying the geometry. We also showed that a single conductor block can be machined into a quadrupole - the gradients are low, but it has potential for ultra-low field harmonics.

We expect that devices such as these, but more importantly the ideas that they embody, will continue to be developed and eventually put into use in future compact accelerators in a variety of applications in medicine, industry, and basic research.

APPENDIX A

Appendices

A.1 Standard Panofsky quadrupole derivation, 2D

The derivation of the gradient formula depends on a few insights:

- H_y only depends on x, not y, for a wide-bore device, or even a narrow-bore device near the center, so H_y is constant along vertical lines.
- From boundary conditions $\vec{H}$ is very small in soft magnetic material because of the very high permeability, and so $\vec{H} \approx 0$.

  Because of this, soft magnetic material dimensions *according to the model* are not important; due to real-life effects such as saturation, however, the soft magnet dimensions can become important and this analysis will break down.
- The total enclosed current depends on the integration path.

With these facts in hand the contour integral evaluates to

$$\oint \vec{H} \cdot d\vec{l} = -H_y d_{Cu} - H_y g - H_y d_{Cu} - (\approx 0) = -I + 2I\frac{W/2 - x}{W}$$

Solving for H_y gives

$$H_y = \frac{B_y}{\mu_0} = \frac{I}{g + 2d_{Cu}}\left(1 - 2\frac{W/2 - x}{W}\right)$$

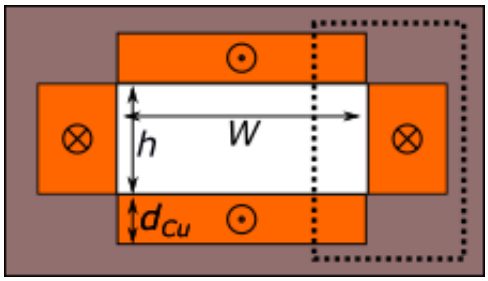

Figure A.1: Standard Panofsky quadrupole. Orange denotes conductors, gray is soft magnetic material in the yoke, and dashed lines are integration paths. Dimensions are noted, though dimensions of soft magnetic material do not appear in this analysis.

The gradient that is $\frac{dB_y}{dx}$, which is computed to be

$$\frac{dB_y}{dx} = \frac{2\mu_0 I}{W(g + 2d_{Cu})} \tag{A.1}$$

This expression can be reduced to the expression found in the original Hand and Panofsky paper provided that the cross-sectional area of the side windings is the same as the top/bottom windings. In this case, $Wd_{Cu} = a/4$, where a is the total cross-sectional winding area.

A.2 Mesoundulator pole tip shaping

Assuming some excitation of the mesoundulator, either through current-carrying wires or permanent magnets, one can specify a desired magnetic field along a line and derive the proper pole tip shape to achieve such a field through conformal mapping. Conformal mapping is a very useful technique of complex analysis used throughout engineering, see for example Ref. [141]. This analysis is strictly two-dimensional in that it ignores three-dimensional end effects and fringing fields. This is not intended to be a complete derivation, but hopefully sketched enough for the reader to understand on a high level how this is done. A helpful resource on magnet design specifically is given in Ref. [116].

We first start with a few definitions. Note the the standard definition of $i = \sqrt{-1}$.

- In the z-plane, $z = x + iy$.
- In the w-plane, $w = u(x, y) + iv(x, y)$.
- The complex potential $F = A + i\tilde{V}$.
- The analytical function $B^*(z) = B_x(x, y) - iB_y(x, y)$, which is simply the complex conjugate of the complex function $B(z)$.
- The relationship between an analytical function (in the following section this is $B^*(z)$) and the complex potential F is $F(z) = i\frac{dF}{dz}$.
- Any parameter with a tilde is considered to be multiplied by the vacuum permeability. Example: for a coil excitation current I, $\tilde{I} = \mu_0 I$.

The concept of an "analytical function" is rooted in complex analysis, and simply means that the function is differentiable. The consequence is that once the analytical function, such as $B^*(z)$, is specified along a line in the domain, the values of the function at any point in the domain are specified. $B^*(z)$ is analytical because it satisfies the Cauchy-Riemann equations.

In turn, the Cauchy-Riemann equations are automatically satisfied by the Laplace equation, which ultimately is the equation that is being solved here.

For this analysis we need only consider one quarter of a period, as shown in Fig. A.2a. The procedure is as follows:

1. specify the desired magnetic field along the midline ($y = 0$) of the undulator,
2. find the complex potential F in a perfect dipole, because the undulator is a series of dipole magnets,
3. find the complex potential F for the undulator from the desired magnetic field,
4. equate the complex potentials, which completes the dipole field mapping onto the problem of the undulator. This equation will yield a condition that will determine the pole tip shape that yields the desired magnetic field along the middle of the undulator.

We desire a perfectly sinusoidal field in the middle of the undulator so $B_x(x, 0) = 0, B_y(x, 0) = -B_0 \cos(k_u x)$, where B_0 is the maximum magnetic field in the gap region and $k_u = 2\pi/\lambda_u$, where λ_u is the undulator period. The analytical function $B^*(z)$ becomes

$$B^*(x, 0) = B^*(z) = +iB_0 \cos(k_u z) \tag{A.2}$$

We can now determine the potential of a window-frame dipole magnet shown in Fig. A.2b. Applying the integral form of Ampere's law and taking appropriate approximations for the specified geometry $B_y(x, y) = -\mu_0 I/h = -\tilde{I}/h$ means we can define an analytic function with the complex variable $w = u(x, y) + iv(x, y)$ as

$$B^*(w) = B_x - iB_y = +i\tilde{I}/h \tag{A.3}$$

and the complex potential $F(w)$ as

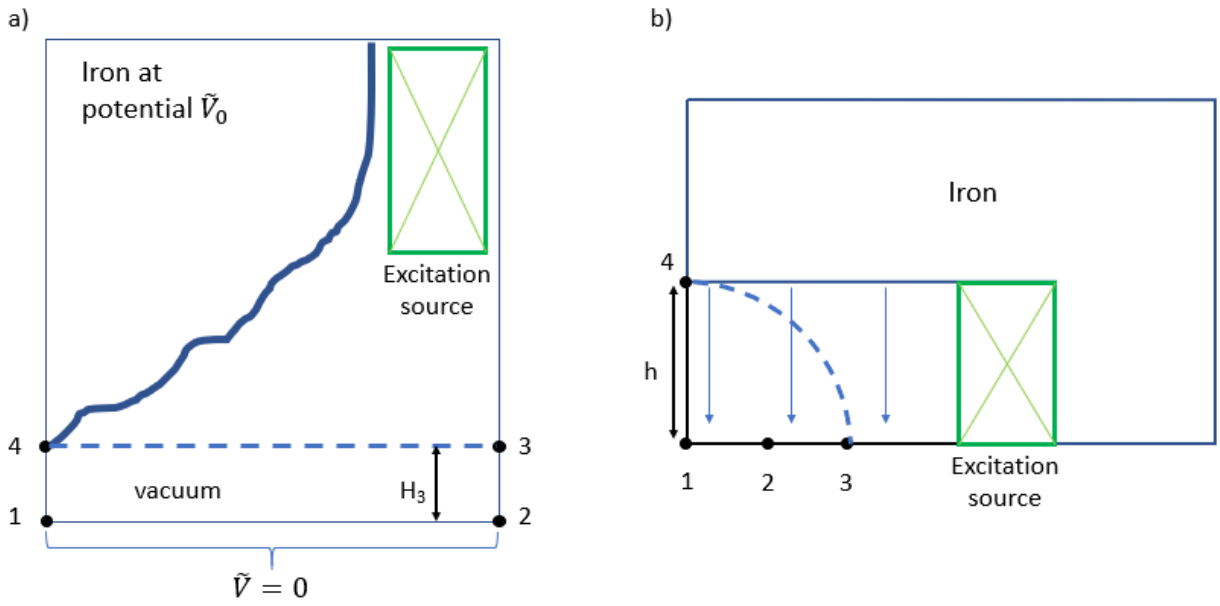

Figure A.2: a) concept sketch over a quarter period of the undulator. The points indicated are mapped onto the points shown in (b). H_3 is half of the gap, and the iron (or soft iron pole tip) is held at a magnetic scalar potential $\tilde{V}_0$. The pole profile is shown here as a sketch only. The midplane potential is $\tilde{V} = 0$ by symmetry. b) concept sketch of the first quadrant of a window-frame dipole magnet, with the specified current excitation. The half-gap distance is h.

$$B^*(w) = i\frac{dF}{dw} \rightarrow F(w) = -i\int \frac{\tilde{I}}{h}dw = \frac{\tilde{I}}{h}w \tag{A.4}$$

We now find the complex potential of the desired undulator. Using Eq. A.2, we find that the complex potential for the undulator field is given by

$$B^*(z) = i\frac{dF}{dz} \rightarrow F(w) = -i\int iB_0\cos(k_u z)dz = \frac{B_0}{k_u}\sin(k_u z) \tag{A.5}$$

We now map the perfect dipole field from the window frame magnet into the desired undulator field. This is done by setting the complex scalar potentials equal, $F(w) = F(z)$. The result is:

$$\frac{\tilde{I}}{h}w = \frac{B_0}{k_u}\sin(k_u z) \tag{A.6}$$

Solving this equation for w yields

$$w = \frac{B_0 h}{\tilde{I}k_u}\sin k_u z = \frac{B_0 h}{\tilde{I}k_u}\hat{w}$$

Then,

$$\begin{aligned}
&\hat{w} = \sin(k_u z) = \frac{e^{ik_u z} - e^{-ik_u z}}{2i} \rightarrow \\
&e^{2ik_u z}\hat{w} - 2ie^{ik_u z} - 1 = 0 \rightarrow \\
&e^{ik_u z} = i\hat{w} \pm \sqrt{1 - \hat{w}^2}
\end{aligned}$$

The last step resulted from application of the quadratic formula. The mapping that we desire requires the positive root, and so we see that a point-to-point mapping with the same complex potential F and analytical magnetic field B^* comes from the equation

$$z = \frac{iw + \sqrt{1 - w^2}}{ik_u} \tag{A.7}$$

where we trivially replaced $\hat{w}$ with w.

Now, recall that $F = A + i\tilde{V}$. Therefore, in general the imaginary part of F corresponds to $\tilde{V}$. Recall further that for the window frame magnet $F(w) = \frac{\tilde{I}}{h}w$, so any point with the same v corresponds to the same $\tilde{V}$ and thus are iso-scalar potential surfaces. We therefore take the imaginary part of w and set it equal to a constant C. Using the identity $\sin(z) = \sin(x + iy) = \sin(x)\cosh(y) + i\cos(x)\sinh(y)$, and realizing that the prefactor of w is simply a multiplicative constant, gives

$$\cos(k_u x)\sinh(k_u y) = C \tag{A.8}$$

To summarize what has been done to get to this point, we specified a desired field profile, which is a perfectly sinusoidal dipole field. We obtained the scalar potential $F(w)$ of a uniform dipole field by using a window dipole magnet, and through conformal mapping required the spatial variation of the dipole field to be the desired field. We then computed the map between domains and realized that the equipotential surface is easily obtained from $F(w)$. We knew from definition that $\mathrm{Im}(F) = \tilde{V}$, but it turns out in the window frame magnet case that $\mathrm{Im}(F(w)) \propto \mathrm{Im}(w)$. Therefore, taking the imaginary part of w and setting it equal to a constant yields the equipotential condition.

Here it is important to state that the constant C as derived here is $C = \frac{B_0 h}{\tilde{I} k_u}$. It is not clear, however, how to determine a set of self-consistent parameters so directly calculating C is not a useful practice. At its core, the equation can only indicate the location of equipotentials. Therefore, we choose C such that the x and y values match the undulator parameters of period and gap, respectively. We show in Fig. A.3 the pole shapes were found using Eq. A.8 for a variety of C over a quarter of an undulator period. One can easily see that the gap increases for larger C values and that the pole shape does change over the range considered

here.

One can see in Fig. A.3 that there is practically no space to the right side of the pole tip for the excitation coils. The only solution is to truncate the pole tip extent to allow for the insertion of excitation coils. This will unfortunately introduce some harmonic content. To make matters worse, we found that the CAD software did not allow us to define the pole tip profile with an arbitrary function, e.g. Eq. A.8. We set the gap to 300 μm and found that with a period of 1.2 mm that $C \sim 0.87$. We found that at the pole profile, within a small distance from the pole tip, is well-approximated by an arc. For $C = 0.87$, the best radius of curvature for the arc is ~250 μm. An arc with this radius of curvature, with the longitudinal extent actually fabricated, superimposed on each of the lines plotted in Fig. A.3. We can see that the agreement is quite good for $C = 0.87$ and for a range of C both above and below 0.87, which means that the curved tips could have satisfactory performance over a range of gaps.

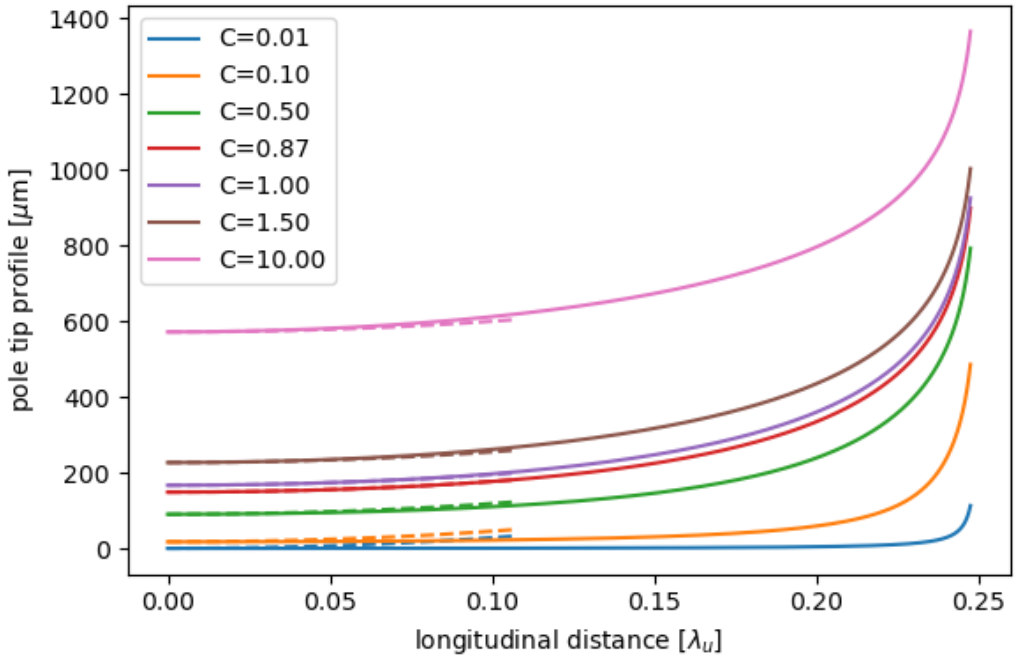

Figure A.3: Pole tip profiles for various C. The solid lines are calculated from Eq. A.8. The dashed lines have a curvature radius of 250 μm and extend over the pole tip region of the fabricated mesoundulator yokes.

REFERENCES

[1] "Undulator." https://en.wikipedia.org/w/index.php?title=Undulator&oldid=993740270. Accessed: 2020-12-14.

[2] K. Halbach, "Desirable excitation patterns for tapered wigglers," *Nuclear Instruments and Methods in Physics Research Section A: Accelerators, Spectrometers, Detectors and Associated Equipment*, vol. 250, p. 95–99, Sep 1986.

[3] R. D. Schlueter, "Wiggler and undulator insertion devices," *Lawrence Berkeley National Laboratory*, 1994.

[4] T. Tanaka and H. Kitamura, "Spectra: a synchrotron radiation calculation code," *Journal of Synchrotron Radiation*, vol. 8, p. 1221–1228, Nov 2001.

[5] V. M. N. Passaro, A. Cuccovillo, L. Vaiani, M. De Carlo, and C. E. Campanella, "Gyroscope technology and applications: A review in the industrial perspective," *Sensors*, vol. 17, p. 2284, Oct 2017.

[6] M. Varanis, A. Silva, A. Mereles, and R. Pederiva, "Mems accelerometers for mechanical vibrations analysis: a comprehensive review with applications," *Journal of the Brazilian Society of Mechanical Sciences and Engineering*, vol. 40, p. 527, Oct 2018.

[7] G. Wu, J. Xu, E. J. Ng, and W. Chen, "Mems resonators for frequency reference and timing applications," *Journal of Microelectromechanical Systems*, vol. 29, p. 1137–1166, Oct 2020.

[8] F. Ejeian, S. Azadi, A. Razmjou, Y. Orooji, A. Kottapalli, M. Ebrahimi Warkiani, and M. Asadnia, "Design and applications of mems flow sensors: A review," *Sensors and Actuators A: Physical*, vol. 295, p. 483–502, Aug 2019.

[9] Y. Hwang, A. Phan, K. Galatsis, O. M. Yaghi, and R. N. Candler, "Zeolitic imidazolate framework-coupled resonators for enhanced gas detection," *Journal of Micromechanics and Microengineering*, vol. 23, p. 125027, Nov 2013.

[10] K. H. Schoenbach and K. Becker, "20 years of microplasma research: a status report," *The European Physical Journal D*, vol. 70, p. 29, Feb 2016.

[11] M. K. Mishra, V. Dubey, P. M. Mishra, and I. Khan, "Mems technology: A review," *Journal of Engineering Research and Reports*, p. 1–24, Feb 2019.

[12] Y. Cao and Z. Xi, "A review of mems inertial switches," *Microsystem Technologies*, vol. 25, p. 4405–4425, Dec 2019.

[13] M. Li and T. Hu, "Research status and development trend of mems s&a devices: A review," *Defence Technology*, Feb 2020.

[14] S. H. Dandgavhal, A. R. Lande, and A. Ahmad, "A state-of-the-art literature review on microelectromechanical systems," in *Computing Algorithms with Applications in Engineering* (V. K. Giri, N. K. Verma, R. K. Patel, and V. P. Singh, eds.), p. 181–199, Springer Singapore, 2020.

[15] F. A. M. Ghazali, M. N. Hasan, T. Rehman, M. Nafea, M. S. M. Ali, and K. Takahata, "Mems actuators for biomedical applications: a review," *Journal of Micromechanics and Microengineering*, vol. 30, p. 073001, May 2020.

[16] M. A. C. Silva, D. C. Guerrieri, A. Cervone, and E. Gill, "A review of mems micropropulsion technologies for cubesats and pocketqubes," *Acta Astronautica*, vol. 143, p. 234–243, Feb 2018.

[17] T. Fritsch, D. Beer, J. Küller, G. Fischer, A. Zhykhar, and M. Fiedler, "Mems acoustical actuators: Principles, challenges and perspectives," in *Microactuators, Microsensors and Micromechanisms* (L. Zentner and S. Strehle, eds.), p. 125–136, Springer International Publishing, 2021.

[18] H. Zahedmanesh, O. V. Pedreira, C. Wilson, Z. Tőkei, and K. Croes, "Copper electromigration; prediction of scaling limits," in *Proceedings of IEEE International Interconnect Technology Conference (IITC)*, IEEE, 2019.

[19] C. Lee, Z. Wu, Y. Xuan, R. J. England, and M. Qi, "Novel fabrication of 3d woodpile accelerator by silicon membrane stacking," *AIP Conference Proceedings*, vol. 1777, p. 060005, Oct 2016.

[20] E. A. Peralta, K. Soong, R. J. England, E. R. Colby, Z. Wu, B. Montazeri, C. McGuinness, J. McNeur, K. J. Leedle, D. Walz, and et al., "Demonstration of electron acceleration in a laser-driven dielectric microstructure," *Nature*, vol. 503, p. 91–94, Nov 2013.

[21] S. V. Kutsaev, "Novel technologies for compact electron linear accelerators (review)," *Instruments and Experimental Techniques*, vol. 64, p. 641–656, Sep 2021.

[22] K. R. Hogstrom and P. R. Almond, "Review of electron beam therapy physics," *Physics in Medicine & Biology*, vol. 51, no. 13, p. R455, 2006.

[23] A. Nevelsky, Z. Bernstein, R. Bar-Deroma, A. Kuten, and I. Orion, "Design and dosimetry characteristics of a commercial applicator system for intra-operative electron beam therapy utilizing elekta precise accelerator," *Journal of Applied Clinical Medical Physics*, vol. 11, no. 4, p. 57–69, 2010.

[24] Y. Danon, R. Block, R. Testa, and H. Moore, "Medical isotope production using a 60 mev linear electron accelerator," *TRANSACTIONS-AMERICAN NUCLEAR SOCIETY*, vol. 98, p. 894, 2008.

[25] K. Peach and C. Ekdahl, "Particle beam radiography," *Reviews of Accelerator Science and Technology*, vol. 6, pp. 117–142, 2013.

[26] M. Silindir and A. Y. Özer, "Sterilization methods and the comparison of e-beam sterilization with gamma radiation sterilization," *Fabad Journal of Pharmaceutical Sciences*, vol. 34, no. 1, p. 43, 2009.

[27] A. J. Berejka and C. Eberle, "Electron beam curing of composites in north america," *Radiation Physics and Chemistry*, vol. 63, no. 3-6, pp. 551–556, 2002.

[28] J. Raghavan and M. R. Baillie, "Electron beam curing of polymer composites," *Polymer composites*, vol. 21, no. 4, pp. 619–629, 2000.

[29] D. Abliz, Y. Duan, L. Steuernagel, L. Xie, D. Li, and G. Ziegmann, "Curing methods for advanced polymer composites - a review," *Polymers and Polymer Composites*, vol. 21, p. 341–348, Jul 2013.

[30] A. Greenwald, A. Kirkpatrick, R. Little, and J. Minnucci, "Pulsed-electron-beam annealing of ion-implantation damage," *Journal of Applied Physics*, vol. 50, no. 2, pp. 783–787, 1979.

[31] A. Broers, W. Molzen, J. Cuomo, and N. Wittels, "Electron-beam fabrication of 80-å metal structures," *Applied Physics Letters*, vol. 29, no. 9, pp. 596–598, 1976.

[32] A. Tanuševski and D. Poelman, "Optical and photoconductive properties of sns thin films prepared by electron beam evaporation," *Solar energy materials and solar cells*, vol. 80, no. 3, pp. 297–303, 2003.

[33] Y. Chen, "Nanofabrication by electron beam lithography and its applications: A review," *Microelectronic Engineering*, vol. 135, p. 57–72, Mar 2015.

[34] D. Norman, J. Jones, W. Yoon, K. Haskell, J. Sterbentz, J. Zabriskie, A. Hunt, F. Harmon, and M. Kinlaw, "Inspection applications with higher electron beam energies," *Nuclear Instruments and Methods in Physics Research Section B: Beam Interactions with Materials and Atoms*, vol. 241, no. 1-4, pp. 787–792, 2005.

[35] S. Kutsaev, R. Agustsson, A. Arodzero, S. Boucher, J. Hartzell, A. Murokh, F. O'Shea, and A. Y. Smirnov, "Electron accelerators for novel cargo inspection methods," *Physics Procedia*, p. 115–125, Jan 2017.

[36] B. Spataro, D. Alesini, V. Chimenti, V. Dolgashev, A. Haase, S. G. Tantawi, Y. Higashi, C. Marrelli, A. Mostacci, R. Parodi, and et al., "Technological issues and high gradient test results on x-band molybdenum accelerating structures," *Nuclear Instruments and Methods in Physics Research Section A: Accelerators, Spectrometers, Detectors and Associated Equipment*, vol. 657, p. 114–121, Nov 2011.

[37] N. Solyak, "Gradient limitations in room temperature and superconducting acceleration structures," *AIP Conference Proceedings*, vol. 1086, 01 2009.

[38] M. Dal Forno, V. Dolgashev, G. Bowden, C. Clarke, M. Hogan, D. McCormick, A. Novokhatski, B. Spataro, S. Weathersby, and S. G. Tantawi, "rf breakdown tests of mm-wave metallic accelerating structures," *Phys. Rev. Accel. Beams*, vol. 19, p. 011301, Jan 2016.

[39] A. D. Cahill, J. B. Rosenzweig, V. A. Dolgashev, S. G. Tantawi, and S. Weathersby, "High gradient experiments with x-band cryogenic copper accelerating cavities," *Phys. Rev. Accel. Beams*, vol. 21, p. 102002, Oct 2018.

[40] B. M. Cowan, "Three-dimensional dielectric photonic crystal structures for laser-driven acceleration," *Physical Review Special Topics - Accelerators and Beams*, vol. 11, p. 011301, Jan 2008.

[41] B. Naranjo, A. Valloni, S. Putterman, and J. B. Rosenzweig, "Stable charged-particle acceleration and focusing in a laser accelerator using spatial harmonics," *Physical Review Letters*, vol. 109, p. 164803, Oct 2012.

[42] K. J. Leedle, R. F. Pease, R. L. Byer, and J. S. Harris, "Laser acceleration and deflection of 96.3 kev electrons with a silicon dielectric structure," *Optica*, vol. 2, p. 158–161, Feb 2015.

[43] K. J. Leedle, A. Ceballos, H. Deng, O. Solgaard, R. F. Pease, R. L. Byer, and J. S. Harris, "Dielectric laser acceleration of sub-100 kev electrons with silicon dual-pillar grating structures," *Optics Letters*, vol. 40, p. 4344–4347, Sep 2015.

[44] K. P. Wootton, Z. Wu, B. M. Cowan, A. Hanuka, I. V. Makasyuk, E. A. Peralta, K. Soong, R. L. Byer, and R. J. England, "Demonstration of acceleration of relativistic electrons at a dielectric microstructure using femtosecond laser pulses," *Optics Letters*, vol. 41, p. 2696–2699, Jun 2016.

[45] J. Breuer and P. Hommelhoff, "Laser-based acceleration of nonrelativistic electrons at a dielectric structure," *Physical Review Letters*, vol. 111, p. 134803, Sep 2013.

[46] M. Kozák, M. Förster, J. McNeur, N. Schönenberger, K. Leedle, H. Deng, J. S. Harris, R. L. Byer, and P. Hommelhoff, "Dielectric laser acceleration of sub-relativistic electrons by few-cycle laser pulses," *Nuclear Instruments and Methods in Physics Research Section A: Accelerators, Spectrometers, Detectors and Associated Equipment*, vol. 865, p. 84–86, Sep 2017.

[47] R. J. England, R. J. Noble, K. Bane, D. H. Dowell, C.-K. Ng, J. E. Spencer, S. Tantawi, Z. Wu, R. L. Byer, E. Peralta, and et al., "Dielectric laser accelerators," *Reviews of Modern Physics*, vol. 86, p. 1337–1389, Dec 2014.

[48] D. Mihalcea, L. Faillace, J. Hartzell, H. Panuganti, S. Boucher, A. Murokh, P. Piot, and J. C. T. Thangaraj, "Measurement of ampère-class pulsed electron beams via field emission from carbon-nanotube cathodes in a radiofrequency gun," *Applied Physics Letters*, vol. 107, no. 3, p. 033502, 2015.

[49] C. Bower, D. Shalom, Wei Zhu, D. Lopez, G. P. Kochanski, P. L. Gammel, and Sungho Jin, "A micromachined vacuum triode using a carbon nanotube cold cathode," *IEEE Transactions on Electron Devices*, vol. 49, no. 8, pp. 1478–1483, 2002.

[50] E. Esarey, C. B. Schroeder, and W. P. Leemans, "Physics of laser-driven plasma-based electron accelerators," *Reviews of Modern Physics*, vol. 81, p. 1229–1285, Aug 2009.

[51] H. S. Ghotra and N. Kant, "Gev electron acceleration by a gaussian field laser with effect of beam width parameter in magnetized plasma," *Optics Communications*, vol. 383, p. 169–176, Jan 2017.

[52] V. Shpakov, E. Chiadroni, A. Curcio, H. Fares, M. Ferrario, A. Marocchino, F. Mira, V. Petrillo, A. R. Rossi, and S. Romeo, "Plasma acceleration limitations due to betatron radiation," *Nuclear Instruments and Methods in Physics Research Section A: Accelerators, Spectrometers, Detectors and Associated Equipment*, vol. 909, p. 463–466, Nov 2018.

[53] M. E. Couprie, "Towards compact free electron–laser based on laser plasma accelerators," *Nuclear Instruments and Methods in Physics Research Section A: Accelerators, Spectrometers, Detectors and Associated Equipment*, vol. 909, p. 5–15, Nov 2018.

[54] W. Qin, L. Zeng, S. Huang, G. Zhao, Y. Ding, Z. Huang, R. Hu, H. Lu, X. Yan, and K. Liu, "Study of a free-electron laser driven by a laser-plasma accelerated beam at peking university," *Nuclear Instruments and Methods in Physics Research Section A: Accelerators, Spectrometers, Detectors and Associated Equipment*, vol. 925, p. 193–198, May 2019.

[55] M. Fuchs, R. Weingartner, A. Popp, Z. Major, S. Becker, J. Osterhoff, I. Cortrie, B. Zeitler, R. Hörlein, G. D. Tsakiris, and et al., "Laser-driven soft-x-ray undulator source," *Nature Physics*, vol. 5, p. 826–829, Nov 2009.

[56] Y. V. Shvyd'ko, S. Stoupin, A. Cunsolo, A. H. Said, and X. Huang, "High-reflectivity high-resolution x-ray crystal optics with diamonds," *Nature Physics*, vol. 6, p. 196–199, Mar 2010.

[57] A. Halavanau, A. Benediktovitch, A. A. Lutman, D. DePonte, D. Cocco, N. Rohringer, U. Bergmann, and C. Pellegrini, "Population inversion x-ray laser oscillator," *Proceedings of the National Academy of Sciences*, vol. 117, p. 15511–15516, Jul 2020.

[58] F. J. Furch, B. A. Reagan, B. M. Luther, A. H. Curtis, S. P. Meehan, and J. J. Rocca, "Demonstration of an all-diode-pumped soft x-ray laser," *Optics letters*, vol. 34, no. 21, pp. 3352–3354, 2009.

[59] T. Popmintchev, M.-C. Chen, A. Bahabad, M. Gerrity, P. Sidorenko, O. Cohen, I. P. Christov, M. M. Murnane, and H. C. Kapteyn, "Phase matching of high harmonic generation in the soft and hard x-ray regions of the spectrum," *Proceedings of the National Academy of Sciences*, vol. 106, no. 26, pp. 10516–10521, 2009.

[60] R. Tatchyn and P. Csonka, "Modelling and characterisation of a micropole undulator with a 726μm period," *Journal of Physics D: Applied Physics*, vol. 20, p. 394–397, Mar 1987.

[61] J. A. Clarke, *The science and technology of undulators and wigglers*. Oxford series on synchrotron radiation, Oxford University Press, 2004.

[62] H. Koziol, "Beam diagnostics for accelerators," tech. rep., CERN, 2001.

[63] E. Tarazona and P. Elleaume, "Measurement of the absolute energy and energy spread of the esrf electron beam using undulator radiation," *Review of Scientific Instruments*, vol. 67, p. 3368–3368, Sep 1996.

[64] M. S. Bakeman, C. B. Schroeder, K. E. Robinson, C. Toth, K. Nakamura, W. M. Fawley, W. P. Leemans, C. B. Schroeder, W. Leemans, and E. Esarey, "Magnetic characterization and design of an undulator-based electron beam diagnostic," in *AIP Conference Proceedings*, p. 643–648, AIP, 2009.

[65] B. Yang and J. Xu, "Measurement of the aps storage ring electron beam energy spread using undulator spectra," in *PACS2001. Proceedings of the 2001 Particle Accelerator Conference (Cat. No.01CH37268)*, vol. 3, p. 2338–2340 vol.3, Jun 2001.

[66] I. Lobach, S. Nagaitsev, V. Lebedev, A. Romanov, G. Stancari, A. Valishev, A. Halavanau, Z. Huang, and K.-J. Kim, *Transverse beam emittance measurement by undulator radiation power noise*. arXiv, Dec 2020.

[67] J. P. Duris, P. Musumeci, and R. K. Li, "Inverse free electron laser accelerator for advanced light sources," *Physical Review Special Topics - Accelerators and Beams*, vol. 15, p. 061301, Jun 2012.

[68] Y. Liu, X. J. Wang, D. B. Cline, M. Babzien, J. M. Fang, J. Gallardo, K. Kusche, I. Pogorelsky, J. Skaritka, and A. van Steenbergen, "Experimental observation of femtosecond electron beam microbunching by inverse free-electron-laser acceleration," *Physical Review Letters*, vol. 80, p. 4418–4421, May 1998.

[69] R. Bonifacio, L. De Salvo Souza, P. Pierini, and N. Piovella, "The superradiant regime of a fel: Analytical and numerical results," *Nuclear Instruments and Methods in Physics Research Section A: Accelerators, Spectrometers, Detectors and Associated Equipment*, vol. 296, p. 358–367, Oct 1990.

[70] J. B. Rosenzweig, N. Majernik, R. R. Robles, G. Andonian, O. Camacho, A. Fukasawa, A. Kogar, G. Lawler, J. Miao, P. Musumeci, and et al., "An ultra-compact x-ray free-electron laser," *New Journal of Physics*, vol. 22, p. 093067, Sep 2020.

[71] S. Tripathi, R. K. Bhandari, S. Ghosh, and D. Kanjilal, "Design of a compact hybrid undulator for the thz radiation facility of delhi light source (dls)," *FEL-2017*, p. 3, 2017.

[72] J. B. Rosenzweig, *Fundamentals of Beam Physics*, p. 54. Oxford University Press, Sep 2003.

[73] J. Bahrdt, "Fourth-order optical aberrations and phase-space transformation for reflection and diffraction optics," *Appl. Opt.*, vol. 34, pp. 114–127, Jan 1995.

[74] J. K. Lim, P. Frigola, G. Travish, J. B. Rosenzweig, S. G. Anderson, W. J. Brown, J. S. Jacob, C. L. Robbins, and A. M. Tremaine, "Adjustable, short focal length permanent-magnet quadrupole based electron beam final focus system," *Physical Review Special Topics - Accelerators and Beams*, vol. 8, Jul 2005.

[75] K. Cheung, L. Velásquez-García, and A. Akinwande, "Fully batch-fabricated linear quadrupole mass filters," in *2008 Solid-State, Actuators, and Microsystems Workshop Technical Digest*, (Hilton Head, South Carolina, USA), p. 316–319, Transducer Research Foundation, Jun 2008.

[76] D. S. Black, K. J. Leedle, Y. Miao, U. Niedermayer, R. L. Byer, and O. Solgaard, "Laser-driven electron lensing in silicon microstructures," *Physical Review Letters*, vol. 122, p. 104801, Mar 2019.

[77] S. V. Kutsaev, "Advanced technologies for applied particle accelerators and examples of their use (review)," *Technical Physics*, vol. 66, p. 161–195, Feb 2021.

[78] T. Godlove, S. Bernal, and M. Reiser, "Printed-circuit quadrupole design," in *Proceedings Particle Accelerator Conference*, vol. 4, p. 2117–2119 vol.4, May 1995.

[79] J. Harrison, Y. Hwang, O. Paydar, J. Wu, E. Threlkeld, J. Rosenzweig, P. Musumeci, and R. Candler, "High-gradient microelectromechanical system quadrupole electromagnets for particle beam focusing and steering," *Physical Review Special Topics-Accelerators and Beams*, vol. 18, no. 2, p. 023501, 2015.

[80] J. Harrison, A. Joshi, J. Lake, R. Candler, and P. Musumeci, "Surface-micromachined magnetic undulator with period length between $10\mu m$ and 1 mm for advanced light sources," *Physical Review Special Topics - Accelerators and Beams*, vol. 15, p. 070703, Jul 2012.

[81] N. V. Smolyakov, "Planar microundulator with rectangular grooved poles," *Nuclear Instruments and Methods in Physics Research Section A: Accelerators, Spectrometers, Detectors and Associated Equipment*, vol. 308, p. 80–82, Oct 1991.

[82] V. L. Granatstein, W. W. Destler, and I. D. Mayergoyz, "Small-period electromagnet wigglers for free-electron lasers," *Applied Physics Letters*, vol. 47, p. 643–645, Sep 1985.

[83] D. C. Meeker, "Finite element method magnetics (ver. 4.2, 28feb2018 build)," 2018.

[84] P. Elleaume, "A new approach to the electron beam dynamics in undulators and wigglers," *EPAC92*, vol. 661, 1992.

[85] Z. Wolf, "Undulator field integral measurements," Dec 2010. doi:10.2172/1000323.

[86] D. Attwood and A. Sakdinawat, *X-Rays and Extreme Ultraviolet Radiation: Principles and Applications*. Cambridge University Press, Feb 2017. Google-Books-ID: 8gZQDQAAQBAJ.

[87] X. Wen, S. Huang, L. Lin, F. Wang, F. Zhu, L. Feng, L. Yang, Z. Wang, P. Fan, J. Hao, and et al., "Superradiant thz undulator radiation source based on a superconducting photo-injector," *Nuclear Instruments and Methods in Physics Research Section A: Accelerators, Spectrometers, Detectors and Associated Equipment*, vol. 820, p. 75–79, Jun 2016.

[88] A. Murokh, R. Agustsson, M. Babzien, I. Ben-Zvi, L. Bertolini, K. van Bibber, R. Carr, M. Cornacchia, P. Frigola, J. Hill, and et al., "Results of the visa sase fel experiment at 840nm," *Nuclear Instruments and Methods in Physics Research Section A: Accelerators, Spectrometers, Detectors and Associated Equipment*, vol. 507, p. 417–421, Jul 2003.

[89] G. Rakowsky, J. Aspenleiter, L. Solomon, R. Carr, R. Ruland, and S. Lidia, "Measurement and optimization of the visa undulator," in *Proceedings of the 1999 Particle Accelerator Conference (Cat. No.99CH36366)*, vol. 4, p. 2698–2700 vol.4, Mar 1999.

[90] B. A. Peterson, F. Herrault, O. D. Oniku, Z. A. Kaufman, D. P. Arnold, and M. G. Allen, "Assessment of laser-induced damage in laser-micromachined rare-earth permanent magnets," *IEEE Transactions on Magnetics*, vol. 48, p. 3606–3609, Nov 2012.

[91] A. Zieba and S. Foner, "Detection coil, sensitivity function, and sample geometry effects for vibrating sample magnetometers," *Review of Scientific Instruments*, vol. 53, p. 1344–1354, Sep 1982.

[92] M. Glickman, T. Niblock, J. Harrison, I. Goldberg, P. Tseng, and J. Judy, "High permeability permalloy for mems," in *2010 Solid-State, Actuators, and Microsystems Workshop Technical Digest*, (Hilton Head, South Carolina, USA), p. 328–331, Transducer Research Foundation, Jun 2010.

[93] P. Musumeci, J. T. Moody, and C. M. Scoby, "Relativistic electron diffraction at the ucla pegasus photoinjector laboratory," *Ultramicroscopy*, vol. 108, p. 1450–1453, Oct 2008.

[94] M. Weissbluth, C. J. Karzmark, R. E. Steele, and A. H. Selby, "The stanford medical linear accelerator," *Radiology*, vol. 72, p. 242–265, Feb 1959.

[95] J. Chavanne and P. Elleaume, "Undulator and wiggler shimming," *Synchrotron Radiation News*, vol. 8, p. 18–22, Jan 1995.

[96] V. A. Papadichev and G. V. Rybalchenko, "A 2.7mm period hybrid pm undulator," *Nuclear Instruments and Methods in Physics Research Section A: Accelerators, Spectrometers, Detectors and Associated Equipment*, vol. 407, p. 419–422, Apr 1998.

[97] J. Pflüger, "Undulators for sase fels," *Nuclear Instruments and Methods in Physics Research Section A: Accelerators, Spectrometers, Detectors and Associated Equipment*, vol. 445, p. 366–372, May 2000.

[98] J.-C. Huang, L.-H. Wu, C.-K. Yang, C.-K. Chuan, T.-Y. Chung, and C.-S. Hwang, "Performance of a nsrrc in-vacuum undulator," *IEEE Transactions on Applied Superconductivity*, vol. 24, no. 3, pp. 1–4, 2014.

[99] J.-C. Huang, H. Kitamura, C.-K. Yang, C.-H. Chang, C.-H. Chang, and C.-S. Hwang, "Challenges of in-vacuum and cryogenic permanent magnet undulator technologies," *Phys. Rev. Accel. Beams*, vol. 20, p. 064801, Jun 2017.

[100] J.-C. Chang, Y.-H. Liu, *et al.*, "Finite element analysis on beam-induced heat load in in-vacuum undulators with a small magnet gap," in *9th Int. Particle Accelerator Conf.(IPAC'18), Vancouver, BC, Canada, April 29-May 4, 2018*, pp. 3760–3762, JACOW Publishing, Geneva, Switzerland, 2018.

[101] W. M. Fawley, D. Prosnitz, and E. T. Scharlemann, "Synchrotron-betatron resonances in free-electron lasers," *Physical Review A*, vol. 30, p. 2472–2481, Nov 1984.

[102] E. Scharlemann, "Wiggle plane focusing in linear wigglers," *Journal of Applied Physics*, vol. 58, p. 2154–2161, Sep 1985.

[103] A. Varfolomeev and A. Hairetdinov, "Advanced hybrid undulator schemes providing enhanced transverse e-beam focusing," *Nuclear Instruments and Methods in Physics Research Section A: Accelerators, Spectrometers, Detectors and Associated Equipment*, vol. 341, p. 462–465, Mar 1994.

[104] C. M. Fortgang, "A pure permanent magnet — two plane focusing — tapered wiggler for a high average power fel," *Nuclear Instruments and Methods in Physics Research Section A: Accelerators, Spectrometers, Detectors and Associated Equipment*, vol. 393, p. 385–388, Jul 1997.

[105] A. A. Varfolomeev, V. V. Gubankov, A. H. Hairetdinov, S. N. Ivanchenkov, A. S. Khlebnikov, N. S. Osmanov, and S. V. Tolmachev, "Mock-up of the focusing undulator for the slac x-ray fel project," *Nuclear Instruments and Methods in Physics Research Section A: Accelerators, Spectrometers, Detectors and Associated Equipment*, vol. 358, p. 70–71, Apr 1995.

[106] S. Caspi, R. Schlueter, and R. Tatchyn, "High-field strong-focusing undulator designs for x-ray linac coherent light source (lcls) applications," May 1995.

[107] Y. Wasa, T. Suzuki, T. Kusaka, K. Inoue, Y. Kawata, A. Kobayashi, and T. Keishi, "Development of a focusing wiggler with trapezoid-shaped permanent magnets," *Nuclear Instruments and Methods in Physics Research Section A: Accelerators, Spectrometers, Detectors and Associated Equipment*, vol. 331, p. 715–720, Jul 1993.

[108] B. J. A. Shepherd and J. A. Clarke, "Magnetic design of a focusing undulator for alpha-x," p. 3, 2004.

[109] T. Okazaki, Y. Hosoda, T. Keishi, and A. Kobayashi, "Adjustable focusing force undulator," *Nuclear Instruments and Methods in Physics Research Section A: Accelerators, Spectrometers, Detectors and Associated Equipment*, vol. 331, p. 673–679, Jul 1993.

[110] K. Robinson and D. Quimby, *Canted-pole transverse gradients in planar undulators*. United States: IEEE Service Center, 1987. INIS Reference Number: 19078220.

[111] A. V. Smirnov, "Performance characterization of twisted undulator," *Review of Scientific Instruments*, vol. 72, no. 3, p. 1649, 2001.

[112] G. Travish and J. Rosenzweig, "Numerical studies of strong focusing in planar undulators," in *Proceedings of International Conference on Particle Accelerators*, p. 1548–1550 vol.2, May 1993.

[113] F. H. O'Shea, R. B. Agustsson, Y. C. Chen, A. J. Palmowski, and E. Spranza, "Development of a short period cryogenic undulator at radiabeam," p. 3, 2016.

[114] R. A. Beth, "Elliptical and circular current sheets to produce a prescribed internal field," *IEEE Transactions on Nuclear Science*, vol. 14, p. 386–388, Jun 1967.

[115] R. A. Beth, "Evaluation of current-produced two-dimensional magnetic fields," *Journal of Applied Physics*, vol. 40, p. 4782–4786, Nov 1969.

[116] K. Halbach, "Understanding modern magnets through conformal mapping," *International Journal of Modern Physics B*, vol. 04, p. 1201–1222, May 1990.

[117] P. R. Sarma, "Coil shape of a two-fold symmetric perfect superconducting quadrupole for use in common-coil twin magnets," *Nuclear Instruments and Methods in Physics Research Section A: Accelerators, Spectrometers, Detectors and Associated Equipment*, vol. 564, p. 81–86, Aug 2006.

[118] P. R. Sarma, N. Ibomcha, and R. K. Bhandari, "Modification of cosθ coil shape in superconducting dipole magnets for reducing the coil size," *Review of Scientific Instruments*, vol. 76, p. 013302, Jan 2005.

[119] P. R. Sarma, "Coil shape of a perfect superconducting sextupole magnet," *Journal of Physics D: Applied Physics*, vol. 40, p. 717–720, Feb 2007.

[120] P. R. Sarma, "Ideal coil shape for combined function superconducting magnets," *Journal of Physics D: Applied Physics*, vol. 40, p. 3056–3059, May 2007.

[121] L. N. Hand and W. K. H. Panofsky, "Magnetic quadrupole with rectangular aperture," *Review of Scientific Instruments*, vol. 30, p. 927–930, Oct 1959.

[122] J. E. Draper, "Beam steering with quadrupole and with rectangular box magnets," *Review of Scientific Instruments*, vol. 37, p. 1390–1394, Oct 1966.

[123] R. Auzolle, F. Kircher, and J. P. Penicaud, "A panofsky-type superconducting quadrupole with a very high gradient homogeneity," *IEEE Transactions on Nuclear Science*, vol. 28, p. 3228–3230, Jun 1981.

[124] R. Peterson, J. Kraushaar, R. Ristinen, H. Thiessen, and M. Rickey, "A versatile multipole correction magnet of rectangular aperture," *Nuclear Instruments and Methods*, vol. 129, p. 47–51, Nov 1975.

[125] Y. Li, P. Chin, R. Kishek, M. Reiser, M. Venturini, J. Wang, Y. Zou, and T. Godlove, "Design, simulation and test of pulsed panofsky quadrupoles," vol. 5, p. 3369–3371, IEEE, 1999.

[126] S. Masubuchi and T. Nakanishi, "Panofsky magnet for the beam extraction from the synchrotron using a fast q-magnet and rf-knockout," *Nuclear Instruments and Methods in Physics Research Section B: Beam Interactions with Materials and Atoms*, vol. 269, p. 2911–2914, Dec 2011.

[127] M. Sullivan, K. Bertsche, P. Vobly, E. Paoloni, S. Bettoni, and P. Raimondi, "A new interaction region design for the super-b factory," *Energy (GeV)*, vol. 7, pp. 4–0, 2010.

[128] K. Melconian, C. Collins, K. Damborsky, J. Kellams, P. McIntyre, N. Pogue, and A. Sattarov, "Design of a mgb_2 beam transport channel for a strong-focusing cyclotron," *IEEE Transactions on Applied Superconductivity*, vol. 24, p. 1–4, Jun 2014.

[129] G. H. Biallas, N. Belcher, D. Douglas, T. Hiatt, and K. Jordan, "Combined panofsky quadrupole corrector dipole," in *2007 IEEE Particle Accelerator Conference (PAC)*, p. 602–604, Jun 2007.

[130] J. Budnick, T. Hall, D. Li, and S. Y. Lee, "Design, fabrication and experimental results of a multi-purpose panofsky magnet," *Nuclear Instruments and Methods in Physics Research Section A: Accelerators, Spectrometers, Detectors and Associated Equipment*, vol. 368, p. 572–578, Jan 1996.

[131] C. R. Bonhote, H. K. DeSimone, J. W. Lam, M. W. Last, E. H. P. Lee, and I. R. McFadyen, "Stress relief for electroplated films," Dec. 2 2008. US Patent 7,459,198.

[132] O. Chubar, P. Elleaume, and J. Chavanne, "A three-dimensional magnetostatics computer code for insertion devices," *Journal of synchrotron radiation*, vol. 5, no. 3, pp. 481–484, 1998.

[133] H. Tanaka, S. Yamashita, Y. Abe, M. Shikida, and K. Sato, "Fast etching of silicon with a smooth surface in high temperature ranges near the boiling point of koh solution," *Sensors and Actuators A: Physical*, vol. 114, p. 516–520, Sep 2004.

[134] K. Sato, M. Shikida, Y. Matsushima, T. Yamashiro, K. Asaumi, Y. Iriye, and M. Yamamoto, "Characterization of orientation-dependent etching properties of single-crystal silicon: effects of koh concentration," *Sensors and Actuators A: Physical*, vol. 64, p. 87–93, Jan 1998.

[135] E. D. Palik, O. J. Glembocki, I. Heard, P. S. Burno, and L. Tenerz, "Etching roughness for (100) silicon surfaces in aqueous koh," *Journal of Applied Physics*, vol. 70, p. 3291–3300, Sep 1991.

[136] C. Lingk and M. E. Gross, "Recrystallization kinetics of electroplated cu in damascene trenches at room temperature," *Journal of Applied Physics*, vol. 84, no. 10, pp. 5547–5553, 1998.

[137] K. Kabra, S. Li, F. Cropp, T. J. Lane, P. Musumeci, and D. Ratner, "Mapping photocathode quantum efficiency with ghost imaging," *Physical Review Accelerators and Beams*, vol. 23, p. 022803, Feb 2020.

[138] D. Alesini, A. Battisti, M. Ferrario, L. Foggetta, V. Lollo, L. Ficcadenti, V. Pettinacci, S. Custodio, E. Pirez, P. Musumeci, and L. Palumbo, "New technology based on clamping for high gradient radio frequency photogun," *Phys. Rev. ST Accel. Beams*, vol. 18, p. 092001, Sep 2015.

[139] E. Prat, "Symmetric single-quadrupole-magnet scan method to measure the 2d transverse beam parameters," *Nuclear Instruments and Methods in Physics Research Section A: Accelerators, Spectrometers, Detectors and Associated Equipment*, vol. 743, pp. 103–108, 2014.

[140] P. Emma, "Electro-magnetic quadrupole magnets in the lcls fel undulator," *Office of Scientific and Technical Information*, 1 2005.

[141] E. Kreyszig, *Advanced Engineering Mathematics, 10th Edition*. Wiley, 2011.